Comprehensive Investigation of Energy Fluence Spectra and MLC Modeling Parameters and their Effects on Dose Calculation Accuracy in Pinnacle

Written By:

Jameel Ali Bashehab, B.Sc. Medical Physics

A Thesis Submitted in Partial Fulfillment
of the Requirements for the
Degree of Master of Science

McMaster University
Department of Medical Physics and Applied Radiation Sciences
July, 2013

Comprehensive Investigation of Energy Fluence Spectra and MLC Modeling Parameters and their Effects on Dose Calculation Accuracy in Pinnacle

Written By:

Jameel Ali Bashehab, B.Sc. Medical Physics

Supervisors:

Dr. Orest Ostapiak, Ph.D., FCCPM
Dr. Kevin Diamond, Ph.D., MCCPM

This work has been performed at Department of Medical Physics
Juravinski Cancer Center, ON, Hamilton, Canada
July, 2013

McMaster University
Department of Medical Physics and Applied Radiation Sciences

ABSTRACT:

The main focus of this work is to improve the existing clinical machine model within the Pinnacle software planning system (at Juravinski Cancer Center, Hamilton, CA). The incident energy fluence spectrum exiting from the accelerator head is considered an important element of the machine model. Relying on the Pinnacle auto modeling function to determine the relative photon fluence spectrum based on percent depth dose curves fitting for various filed sizes, led to different solutions when the process cycle were repeated. This work presents a new method for determining the Pinnacle photon energy fluence spectrum based on 6 MV Varian 21EX machine. A Monte Carlo simulation spectrum based on BEAMnrc code was attenuated to various depths of water. We determine that, the BEAMnrc spectrum attenuated by 15 cm of water gives the closest agreement between the computed and measured depth dose, similar to the clinical machine spectrum.

Implementing the novel spectrum into a machine that retained the same modeling parameters as the clinical machine (21ex-JCC) shows a slight better calculation of the output factor. The MLC model parameters were also investigated, however, adjusting the MLC offset table was found to give significant improvements, especially for the small field geometries.

The full impact of adjusting the photon energy spectrum, Off-Axis Softening Factor, MLC rounded leaf tip radius and MLC calibration offsets were investigated individually, resulting in a good model parameter fit. Several proposed supplementary setups were created to further assess our model. This include a geometry sensitive to

MLC abutment leakage, the calculation of output factors for long and narrow MLC defined fields, and small square MLC and jaws defined fields. A Sun-Point diode detector was used in the measurement of the output factors for its accurate precision at small geometries. In addition, a GAFCHROMIC EBT2 film dosimetry was used in the measurement of the MLC abutment leakage.

Our new model shows superior results in comparison to the clinical 21ex-JCC machine model, especially with MLC small field calculations. We conclude that relying on PDD curves and dose profiles validation method in assessing the model might not necessarily lead to the best machine parameters, since these are not sensitive to subtle changes in parameters that have important dosimetric consequences.

ACKNOWLEDGEMENT:

I first and foremost want to express my appreciation and thanks towards my supervisors, Dr. Kevin Diamond and Dr. Orest Ostapiak, for their invaluable guidance, encouragement, and support during the full course of this work. Many thanks to Ms. Lisa Gamble, and the entire staff of physics quality assurance at the Juravinski Cancer Center, for their helps during the measurements of our examined setups of this work. My deep appreciation also goes to Dr. Tom Farrell, for his assistance and advice during my Master's study. I would like also to give special thanks to my parents and my wife, for their support, encouragement, and patients as always.

Table of Contents

LIST OF FIGURES:

LIST OF GRAPHS:

LIST OF TABLES:

CHAPTER 1: INTRODUCTION

1.1 - Overview of Linear Accelerator Operation:

A direct current (DC) is provided through a power supply to a modulator, which is responsible for the generation of high-voltage pulses of a few microseconds duration. These high voltage pulses are delivered to the klystron and the electron gun simultaneously as shown in figure 1 (Khan, 2010)[1].

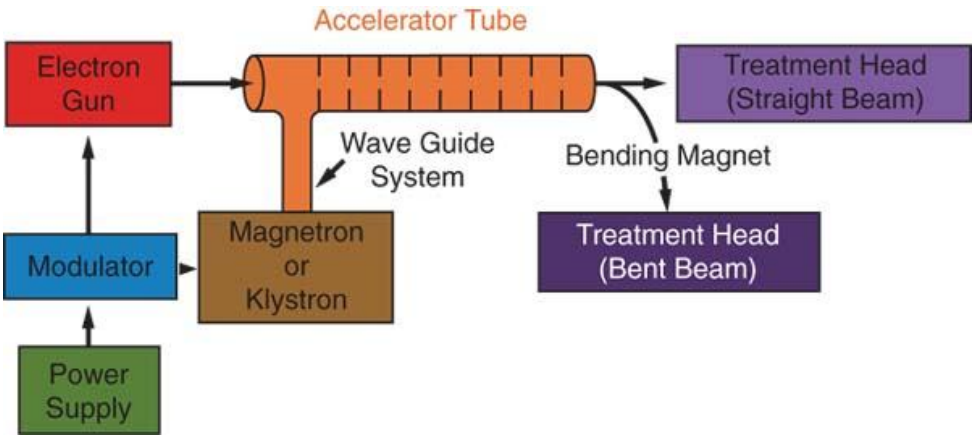

Figure 1. Typical modern linear accelerator (Khan, 2010)[1]

The klystron is a high-energy microwave amplifier used to accelerate the electrons. The klystron does not generate the microwave power. Figure 2 shows a cross-sectional diagram demonstrating a two-cavity klystron. Electrons are produced at the cathode, which contains a wire filament that works as an electron gun. The cathode has a negative charge that causes the electrons to accelerate into the first cavity (buncher cavity) to interact with low energy microwave power.

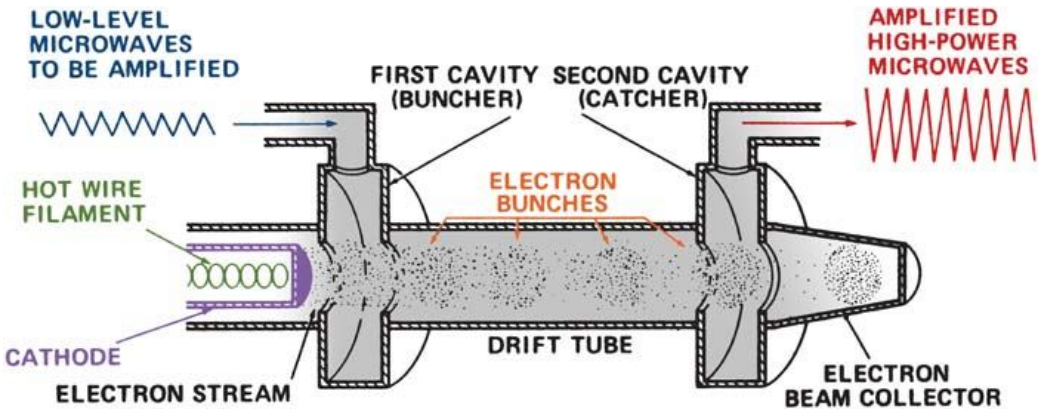

Figure 2. Demonstrating a two-cavity cross-sectional klystron diagram. From (Khan, 2010)[1]

The microwaves causes an alternating electric field across the buncher cavity; this actions causes some electrons to speed up, some others to slow down while some to remain unaffected in a process called velocity modulation. This results in electrons being bunched as they are guided to the field-free space in the drifting tube toward the second cavity. The second cavity generates a retarding field due to the induced charge at the ends of the cavity from the bunched electrons. This process leads to deceleration of electrons by converting their kinetic energy into high intensity microwave power used to energize the linear accelerator structure (Khan, 2010)[1].

These pulsed high-power microwaves are injected into the accelerator tube structure (accelerator waveguide tube) in synchrony with the pulsed electrons from the machine electron gun. The linear accelerator structure tube consists of a copper tube of consisting long series of adjacent cylindrical cavities located in the machine gantry that is evacuated to high vacuum (Karzmark *et al*, 1998)[2]. Electrons accelerate by interacting with the electromagnetic field of the microwaves in a process analogous to that of a

surfer (Khan, 2010)[1]. Higher speed gains to nearly the speed of light increases the mass of the electrons, which corresponds to higher kinetic energy (Karzmark et al, 1998)[2]. As the high-energy electrons emerge from the exit window of the accelerator waveguide tube, they are in the form of a pencil beam of about 3 mm in diameter (Khan, 2010)[1].

For low-energy linacs up to 6 MV, the accelerated electrons may proceed straight on and strike a target for x-ray production. However, high-energy linacs require a longer accelerator structure tube; therefore, a bending magnet turns the beam exiting the accelerator structure tube causing it to become perpendicular to the treatment table. In addition, electrons emerging from the accelerator structure have a range of electron energies. The bending magnet ensures the beam is as monoenergetic as possible. For example, Varian uses an achromatic three-sector 270-degree magnet turn; each sector includes magnetic poles slits of 90-degree turn as demonstrated in figure 3. Each slit ensures that electrons of energy ± 3% of the targeted energy proceed to the next pole.

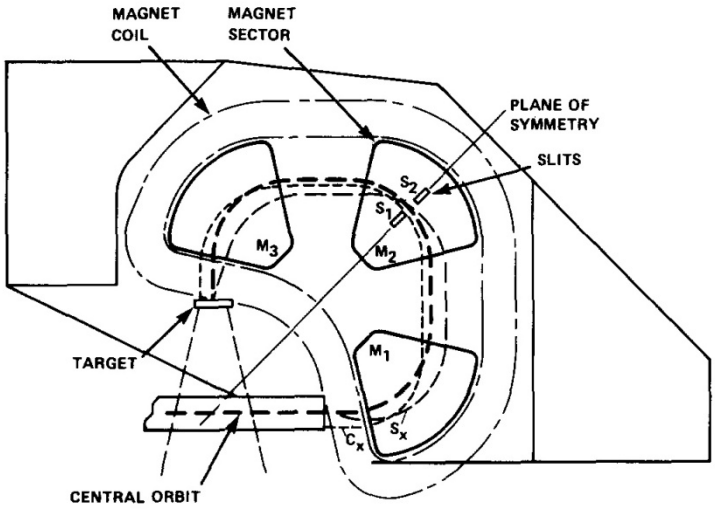

Figure 3. Cross-section view of achromatic three-sector 270-degree bending magnet. (C. J. Karzmark, 1984)[3]

The magnetic field causes the lower energy electrons to bend too sharply, while causing the higher energy electrons to bend not sharply enough to pass through the energy slits. Thus, each turn acts as an energy filtration and focusing device. As a result, the energy spread after passing through the bending magnet is within ± 1% (C. J. Karzmark, 1984)[3].

1.1.1 - Linear Accelerator Head Component:

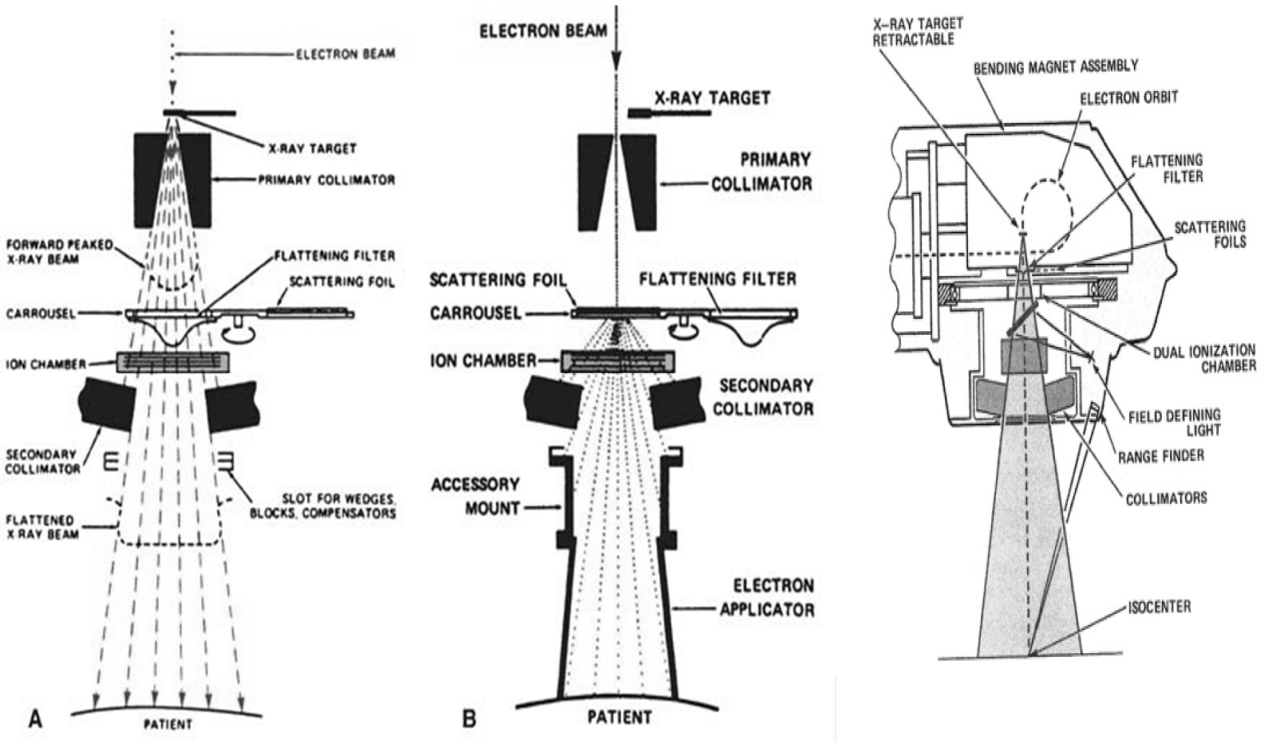

Figure 4. Treatment head component representing A: X-ray mode, B: Electron mode (Karzmark *et al*, 1998)[2]

The linear accelerator head consists of a thick shell of high-density shielding material such as lead, tungsten and lead tungsten alloy. It also contains an x-ray target, scattering foil, flattening filter, ion chamber, primary fixed collimator and secondary

moveable collimator and a light localizer system (Khan, 2010)[1]. The shielding in the head is considered sufficient against radiation leakage. For the electron beam mode, the target is retracted allowing the accelerated electron beam to proceed as demonstrated in figure 4-B. Since the electron beam is in the form of a pencil beam, an **electron scattering foil** is introduced to provide uniform electron fluence across the treatment field. The scattering foil consists of a thin metallic foil, usually of lead, that has the required thickness to scatter the electron beam rather than converting it into a bremsstrahlung x-ray. However, some small fraction of the total energy is still converted into a contamination bremsstrahlung x-ray beam. In order to minimize this, some machine designs replace the scattering foil with electromagnetic scanning of the electron pencil beam over a large area. However, contamination x-rays are still produced by the interaction of electrons with high Z materials such as the collimator walls (Khan, 2010)[1].

In x-ray mode, the accelerated electron beam is incident onto a high Z material **target** such as tungsten, as shown in figure 4-A (note that the Varian 21ex uses Tungsten-Copper). As a result, bremsstrahlung x-rays are produced in a spectrum of energies that has a maximum energy equal to the energy of the incident electrons before hitting the target; and an average energy equal to approximately 1/3 of the maximum energy. Therefore, since the x-rays produced are heterogeneous in energy, they are designated by the nominal acceleration potential in units of megavolts as if the x-ray beam was produced by applying that voltage across the x-ray tube, whereas since electron beams are almost monoenergetic before incident on a patient surface, they are designated by million electron volts (Khan, 2010)[1].

The x-ray beam is collimated first by **a primary collimator**, which is located immediately beyond the target. The high-energy x-ray intensity is peaked in the forward direction giving more intensity along the center of the beam; this intensity falls off in proportion to the distance from the center. In order to make the beam uniform across the field, **a flattening filter** is inserted in the beam as shown in figure 4-A. It is designed in a shape similar to the shape of the beam intensity before hitting the filter. This filter attenuates more photons at the central axis of the beam and fewer photons toward the edge of the field producing a uniform dose distribution at a certain depth. As a consequence, this results in some degree of beam hardening toward the center of the beam with higher energy photons near the central axis and relatively lower energy photons far from the central axis.

The beam then passes through **a dose monitoring chamber** consisting of two independent ionization chambers, which are transmission type and cover the entire beam (Khan, 2010)[1]. The first ionization chamber monitors the integrated dose, dose rate and field symmetry, while the second ionization chamber works as backup to the first one.

A secondary movable x-ray collimator then further collimates the beam where treatment field size can be defined. The secondary collimators are composed of two pairs of lead or tungsten blocks (jaws) that can work independently of one another. Nevertheless, these jaws are limited only to square or rectangular field sizes from 0 x 0 to a maximum of 40 x 40 cm^2. This collimation works in x-ray mode. For electron mode, further electron collimation is required as shown in figure 4-B since electrons scatter more readily in air. Therefore, the beam must be collimated very close to the skin

surface of the patient by using **electron collimation systems** (Khan, 2010)[1]. Nevertheless, to fit the radiation field to the exact treatment shape desired by the physician for either modes, Cerrobend blocks may be used. Cerrobend is an alloy that is composed of 50% bismuth, 26.7% lead, 13.3% tin and 10% cadmium. It has a density of 9.4 g/cm^3 (in comparison to lead, which has a density of 10.66 g/cm^3) and a melting point of 70º C. This makes it easy to cast it into any shape and use it for blocking. The blocks can be mounted on a Lucite plate or blocking tray to be used as customized blocks (Khan, 2010)[1]. A drawback to blocks is that the process of cutting and shaping is considered time consuming and messy, especially when a change to the field is needed, and the whole process has to be repeated.

A light localizing system is used to define the treatment field size. It consists of a mirror and a light source that is located in the space between the ion chambers and the jaws, which projects the light beam as if it is emitted from the x-ray target focal spot, making this light corresponded to the radiation field (Khan, 2010)[1].

1.1.2 - Multi-Leaf Collimation System:

The MLC system works only for photon mode; it consists of two opposing banks that contain a large number of collimating leaves (blocks) that can be driven automatically independent of each other along the x-axis to create a field of any shape. The leaves are made of tungsten alloy that has a density from 17-18.5 g/cm^3. For example, the Varian Millennuim MLC consists of 120 attenuating leaves, 0.5 to 1 cm in width as projected at isocenter (100 cm source to axis distance) and a thickness of 5.65 cm. This thickness is usually sufficent to provide less than 2% primary x-ray

transmission through the leaves in comparson with about 1% transmission for jaws and 3.5% for cerrobend blocks (Khan, 2010)[1].

The MLC leaf ends have one of two designs. A double focused leaf end design has leaves following the beam divergence as the field opens and closes as shown in figure 5-A. The advantage of this approach is that it provides a sharp beam cutoff at the field edges, although for a high-energy beam, this is achieved only to a limited extent due to scattered photons and electrons (Khan, 2010)[1]. This approach has been implemented on the current generation of Siemens accelerator.

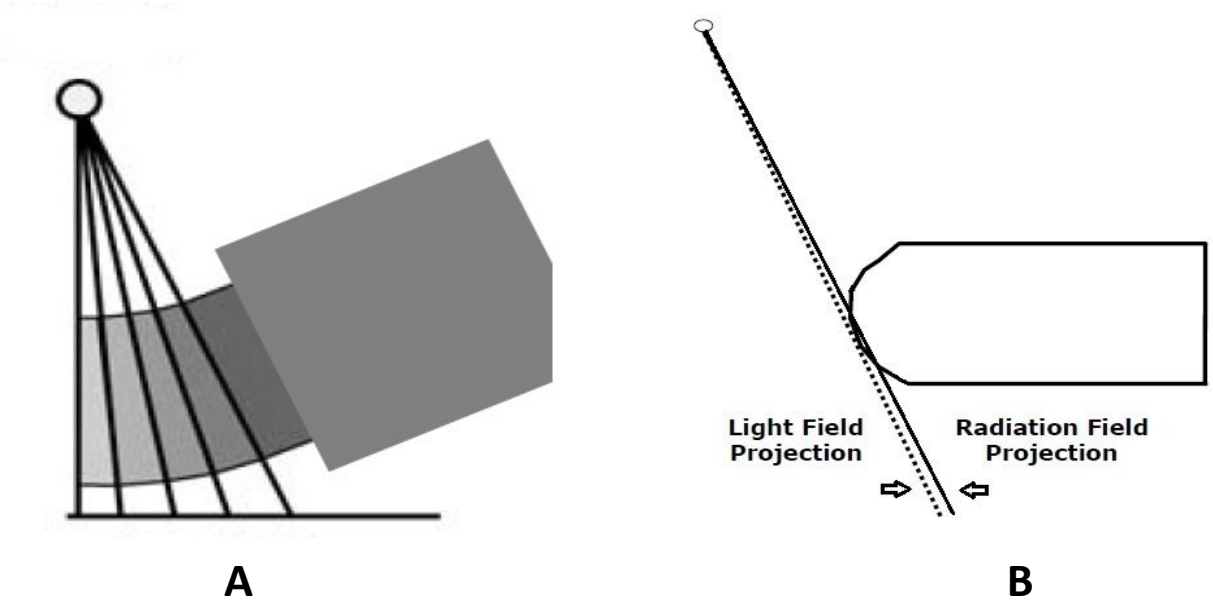

Figure 5. Demonstration of MLC leaves ends design A: Focused leaves, B: Non focused (rounded) leafs ends (44th AAPM Annual Meeting, 2002)

Because of complexity and difficulties in manufacturing, other companies (i.e. Varian and Philips) have implemented a simpler approach where the leaf movement is restricted to a single plane but with the use of rounded leaf edges, as shown in figure 5-B. This implementation provides a constant beam transmission through the leaf edges

regardless of the leaf position. However, a drawback to this design is that penumbra width is larger than that of a focused leaves designs (AAPM TG 50, 2001)[4]. In addition, transmission through the leaf edges is greater when leaves are abutted. Nevertheless, a ray that is tangent to a point at the leaf end surface determines the light-field projection at the isocenter level (Boyer and Li, 1997)[5]. Therefore, in order to match linear leaf translations with linear light-field projections, an offset table has been implemented.

Moreover, another problem associated with the MLC design is the inter-leaf leakage between adjacent leaves. The tongue-and-groove design was introduced to minimize this leakage as demonstrated in figure 6.

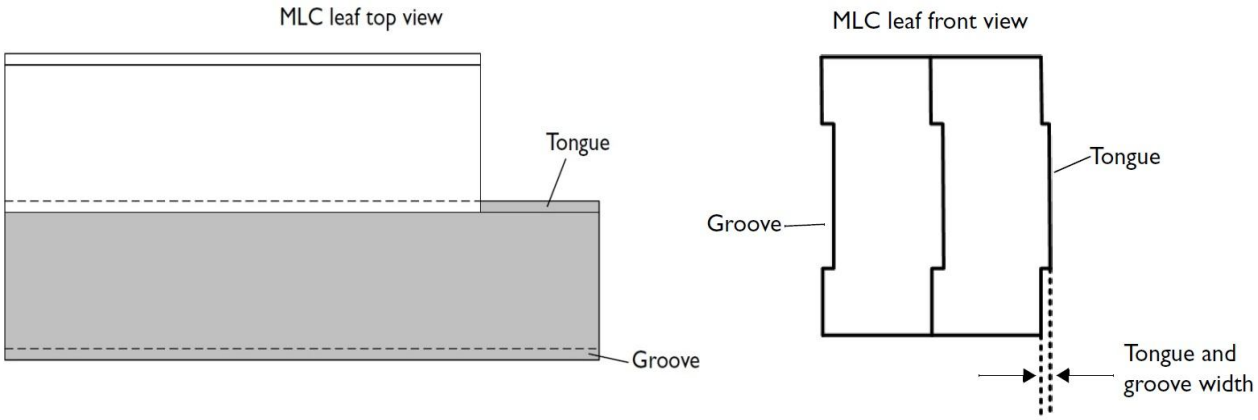

Figure 6. Demonstration of MLC tongue-and-groove design. (Pinnacle[3] Physics Reference Guide, Release 8.0)[6]

The design involves parts of the leaf to be overlapping with an adjacent leaf. Each leaf has a tongue on one side and a groove on the other, which then limits the interleaf leakages by attenuating the radiation by at least half of the MLC thickness (Pinnacle[3] Physics Reference Guide)[6].

On the other hand, this design has a limitation caused by tongue-and-groove effect. Deng *et al*, 2001[7] described this effect as shown in figure 7. The intensity profile in 7-A results when the upper leaf stays in the beam while the lower leaf is out of the beam. Conversely, 7-B shows the intensity profile that occurs when the upper leaf is out of the beam while the lower leaf is in the beam. However, when the two profiles (A and B) are added together, the resultant intensity profile is shown in 7-C, which has a low dose region centered between two adjacent leaves demonstrating the tongue-and-grove effect.

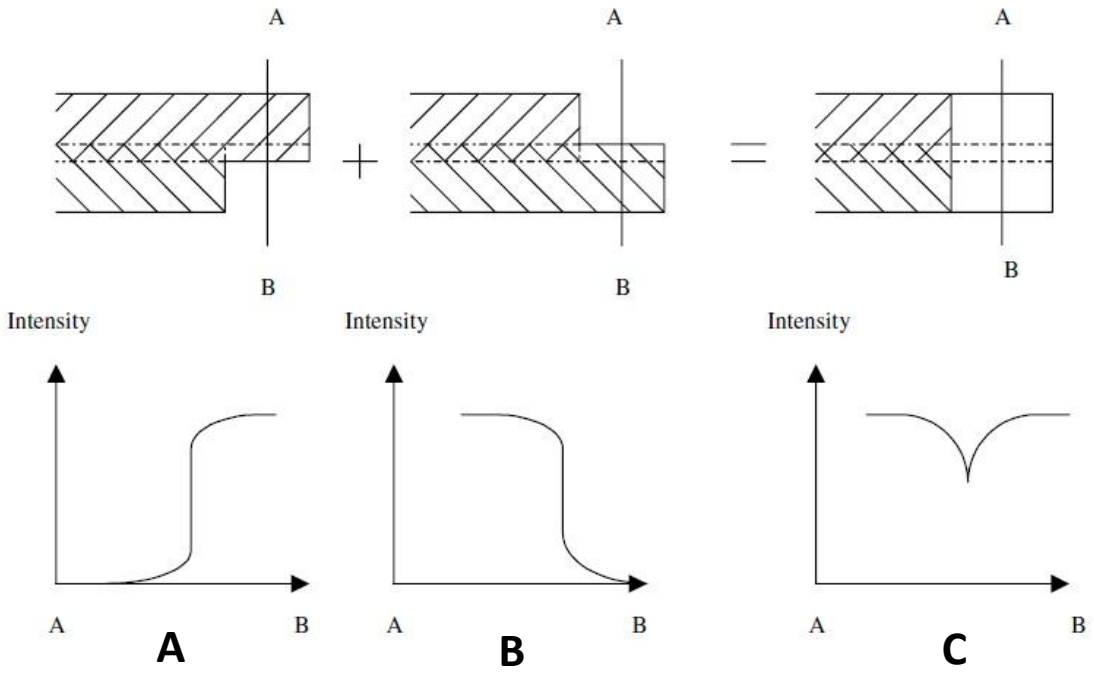

Figure 7. An MLC diagram demonstrating the tongue-and-groove effect, (J Deng *et al*, 2001)[7]

Deng *et al*, 2001[7] pointed out that, "In an IMRT treatment using an MLC, the tongue and groove effect will occur when the overlapping region between two adjacent pairs of leaves is covered by the tongue, or the groove or both for the most of time

during beam delivery". Moreover, based on their study, this effect is negligible on dose distributions when five or more beams are used in the treatment plan (Deng *et al*, 2001)[7].

Apart from that, the use of an MLC has a great impact in modern radiotherapy techniques such as IMRT and VMAT, where field shaping is automated and beam intensity is modulated by controlling individual MLC leaves continuously in order to conform the dose to the target and spare normal tissues (Khan, 2010)[1].

1.2 - Photon Beam Spectra Specification:

In a clinical x-ray photon mode, the energy spectrum exiting the head mainly consists of three components: primary photons, scattered photons and contaminant electrons. The photon energy spectrum contains primary photons coming directly from the target to the patient and scattered photons that are generated or scattered in the accelerator head components other than the target and mainly from the flattening filter.

In addition, electron contamination occurs by the interaction of primary and scattered photons with the accelerator head components. However, the flattening filter and the beam monitoring chamber are the dominant sources of electron contamination (Medina Al *et al*, 2005)[8]. The flattening filter absorbs the secondary electrons that are generated in the target and the primary collimator. Yet, it is responsible for the generation of secondary electrons with wide energy spectra from within the filter whose mean energy is of the same order as that of the photon spectra. Moreover, electron contamination contributes only to the surface dose distribution and the dose at shallow depth (Medina Al *et al*, 2005)[8].

Knowledge of the spectrum and its angular distribution incident on the surface of a patient is required in developing a treatment plan for photon beam therapy (Mohan *et al*, 1985)[9]. However, this spectrum is difficult to determine since it is a complex function that depends on initial electron beam energy, target thickness and material, primary and secondary collimation and flattening filter design. This is due to processes involving absorption, scattering and filtering of the primary photon beam, which as a result, yields a poly-energetic photon beam that has a different energy spectrum compared to that of the primary photon beam.

There have been various experimental methods used to determine the photon beam spectrum [47 - 48 - 49 - 50 - 51]. However, the Monte Carlo method remains the most comprehensive and accurate method (Sheikh-Bagheri *et al*, 2002)[10]. One of the earlier comprehensive Monte Carlo works for determining such spectra for various energies of the Varian linacs was provided by (Mohan *et al*, 1985)[9]. Yet, their spectra suffered from statistical noise due to the limited computing power available at that time. In addition, they did not derive any of the incident electron beam parameters (Sheikh-Bagheri *et al*, 2002)[10]. Calculating such spectra with high accuracy requires more knowledge of the characteristics of the electron beam incident on the target, in addition to better tools for defining and modeling the accelerator head physical components.

BEAMnrc is a general-purpose Monte Carlo user code designed especially for simulation of radiotherapy beams of treatment units based on the EGS4 code system. Sheikh-Bagheri *et al*, 2002[10] reported a work based on BEAMnrc code of nine megavoltage photon beam spectra calculated from three major medical linear accelerator manufacturers for an energy ranging from 4 to 25 MV. They have reported

that the calculated and measured depth-dose data agrees to within 1%. Moreover, the calculated central-axis photon spectra have much reduced statistical uncertainty in comparison to Mohan *et al*, 1985[9] spectra. Table 1 lists results for contributions of direct and scattered photons to the photon energy fluence for 6, 10 and 18 MV beams based on their simulation for the Varian linac.

Energy Mode (MV)	**Photons per 10^6 incident Electron**	**Ψ_{Direct} (%) [$<E_{Dir}>$] (MeV)** Primary Photon	**Ψ_{PC} (%) [$<E_{PC}>$] (MeV)** Scattered Photon	**Ψ_{FF} (%) [$<E_{FF}>$] (MeV)** Scattered Photon	**Ψ_{JAW} (%) [$<EJ_{JAW}>$] (MeV)** Scattered Photon
6	1647 ± 1	94.97 ± 0.07 [1.63]	2.14 ± 0.01 [1.39]	2.61 ± 0.01 [1.16]	0.213 ± 0.003 [1.91]
10	2869 ± 3	94.56 ± 0.06 [3.04]	1.15 ± 0.01 [1.77]	4.00 ± 0.01 [1.79]	0.234 ± 0.002 [2.44]
18	7207 ± 5	94.64 ± 0.08 [4.86]	0.81 ± 0.01 [2.32]	4.28 ± 0.01 [2.71]	0.218 ± 0.003 [2.80]

Table 1. Contributions of direct and scattered photons to the energy fluence, Ψ, for Varian linac at 10 x 10 cm^2 field at 100 cm. Where PC represent primary collimator, FF represent the flattening filter, JAW represent the Jaws and $<E_A>$ represent average energy of type A (Sheikh-Bagheri *et al*, 2002)[10]

The table shows that over 94% of the energy fluence is due to primary photons exiting the target while the rest is due to photons scattered from interactions of a primary photon with the linac head components for 10 x 10 cm^2 field projected at 100 cm for Varian Linac. Scatter from jaws contributes to less than 1% in total (Sheikh-Bagheri *et al*, 2002)[10]. It is also observed that as the energy increases, the fraction of scattered photons generated by the primary collimator decreases, since high-energy photons tend to scatter more in the forward direction of the beam. Table 2 and graph 1 present the tabulated photon fluence spectra for 6 MV beam on the central axis based on BEAMnrc code for Varian Linac. Sheikh-Bagheri *et al*, 2002[10] report that the precision used in the

calculation is high as indicated by the low uncertainty in each of the 250 keV wide bins, except for the high-energy end of the spectra.

Varian 6 MV Energy	**Photon Fluence Spectra** (photons per MeV per incident electron)
0.25	2.14E-05 (1.0%)
0.5	1.26E-04 (0.4%)
0.75	1.31E-04 (0.3%)
1	1.14E-04 (0.3%)
1.25	9.76E-05 (0.4%)
1.5	8.36E-05 (0.4%)
1.75	7.25E-05 (0.4%)
2	6.23E-05 (0.4%)
2.25	5.35E-05 (0.5%)
2.5	4.59E-05 (0.5%)
2.75	3.95E-05 (0.5%)
3	3.47E-05 (0.5%)
3.25	2.98E-05 (0.6%)
3.5	2.61E-05 (0.6%)
3.75	2.25E-05 (0.6%)
4	1.91E-05 (0.7%)
4.25	1.66E-05 (0.7%)
4.5	1.38E-05 (0.8%)
4.75	1.14E-05 (0.8%)
5	9.04E-06 (0.9%)
5.25	6.55E-06 (1.0%)
5.5	4.09E-06 (1.3%)
5.75	1.40E-06 (2.2%)
6	4.34E-08 (11.4%)

Table 2

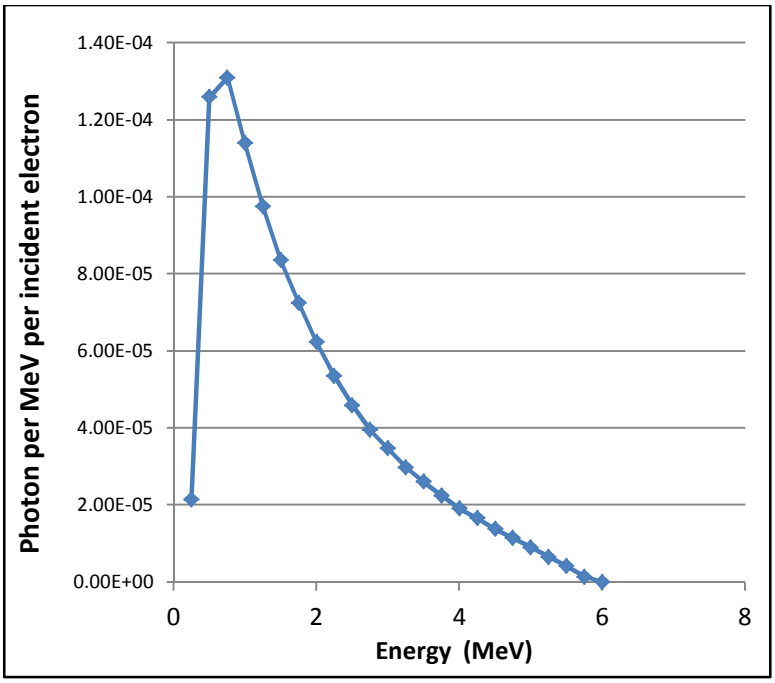

Graph 1

Table 2 and Graph 1. Represent the photon fluence spectra on central axis (photons per MeV per incident electron) for radial bin 0 ≤ r ≤ 2.5 cm. Each bin is 250 keV wide, the tabulated fluence is at the end of each pin involving pin uncertainty (Sheikh-Bagheri *et al*, 2002)[10]

Sheikh-Bagheri *et al*, 2002 also shows that the electron contamination contribution to central axis-depth dose for 10 x 10 cm^2 field at 100 cm SSD is about 6% of maximum dose for a 4 MV beam and 11% for a 25 MV beam. Moreover, in another investigation based on BEAMnrc code, electron contamination for 6 MV Varian 21EX

was up to 7% for 10 x 10 cm^2 field and 21% for 40 x 40 cm^2 field at the surface (Ding, 2002)[11]. Ding, 2002[11] also reported that the increase of surface dose with increases of field size is mainly associated with the increase of incident contaminant electrons; yet electron incident fluence is less than 1% of the incident photon fluence.

1.3 - 6 MV Beam Characteristics:

Beam characteristics are usually defined in terms of the percentage depth-dose (PDD) and the dose profile curves. PDD distribution represents the percentage ratio of the absorbed dose at any depth to the absobed dose at a fixed reference depth along the central axis of the beam; where the reference depth is always the depth of maximum dose, which is typically 1.5 cm for an energy of 6 MV. There are many conditions that influence the PDD distribution since it is dependent on beam energy, depth, field size and distance from the source (Khan, 2010)[1]. Thus, the dose at 10 cm depth for 10 x 10 cm^2 field size is typically 67% for a 100 cm SSD setup.

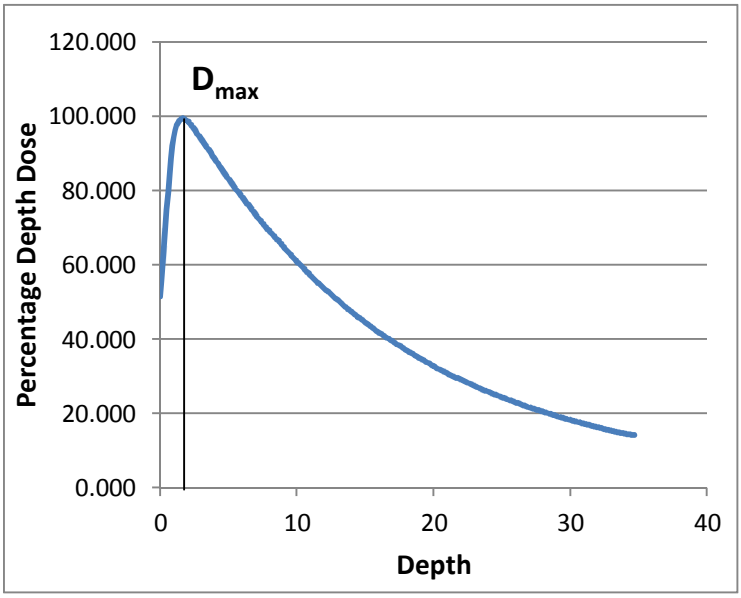

Graph 2. 6 MV PDD distribution in water

As shown in graph 2, PDD is characterized by 3 regions. First, the buildup region where absorbed dose increases with depth due to the ejection of high-speed secondary electrons at various depths that travel downstream until they reach a maximum depth where electronic equilibrium occurs. However, photon fluence continuously decreases with depth resulting in less production of secondary electrons and hence, a net decrease in electron fluence. That causes the absorbed dose to decrease exponentially beyond the maximum depth. Nevertheless, since the dose depends on the electron fluence, contaminant electrons influence the entrance-absorbed dose.

However, central axis PDD distribution is not sufficient to characterize the radiation beam that produces a dose distribution in a three-dimensional volume (Khan, 2010)[1]. In order to achieve this, distributions are visualized by lines that are drawn through points representing the lateral dose distribution at the same depth referred as dose profile plot curves as shown in graph 3.

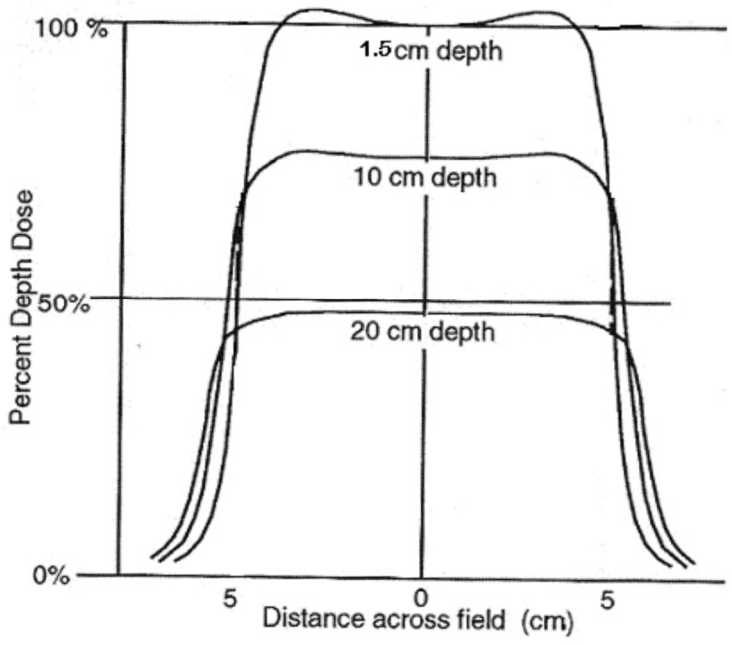

Graph 3. 6 MV dose profile distribution (Bentel, 1996)[12]

At shallow depth, the dose increases gradually toward the edges of the field causing areas of higher dose (horns), while the dose decreases gradually toward the edges of the field at deeper depths. This is as we discussed before in section 1.1.1, due to the effect of the flattening filter beam hardening on the central-axis and beam softening at off-axis positions. However, at a depth of 10 cm, the flattening filter yields a uniform dose profile. Besides that, the horns are dependent on field size, since they will appear more pronounced with large field size, which increases the amount of scatter contribution.

The dose at the edges of the field falls off due to the loss of side scatters in addition to geometric penumbra effects. Moreover, dose outside the field is due to side scatter and leakage from the accelerator head (Khan, 2010)[1].

1.4 - Treatment Planning Software Dose Calculation Methods:

The purpose of the treatment-planning software is to produce a uniform dose distribution within the target volume (typically between 95 and 107%) while minimizing the dose received by normal tissues outside the target. Beam energy, field size, field position and orientation, beam-shaping devices to shield critical structure from radiation exposure (blocks and MLC) and relative weighting between fields are typically modified. In addition, the calculated dose must correspond to the real absorbed dose in the patient as accurately as possible. Thus, uncertainties in the calculation should be minimized as much as possible especially when it comes to more advanced techniques, where high dose is prescribed close to critical organs. This is because, certain organs in the body have a critical tolerance dose level that should not be exceeded.

In general, the calculated absorbed dose distribution is the convolution of the TERMA (total energy released per unit mass) with the energy deposition kernels (EDKs) (PW Hoban *et al*, 1994)[13] as demonstrated on figure 8.

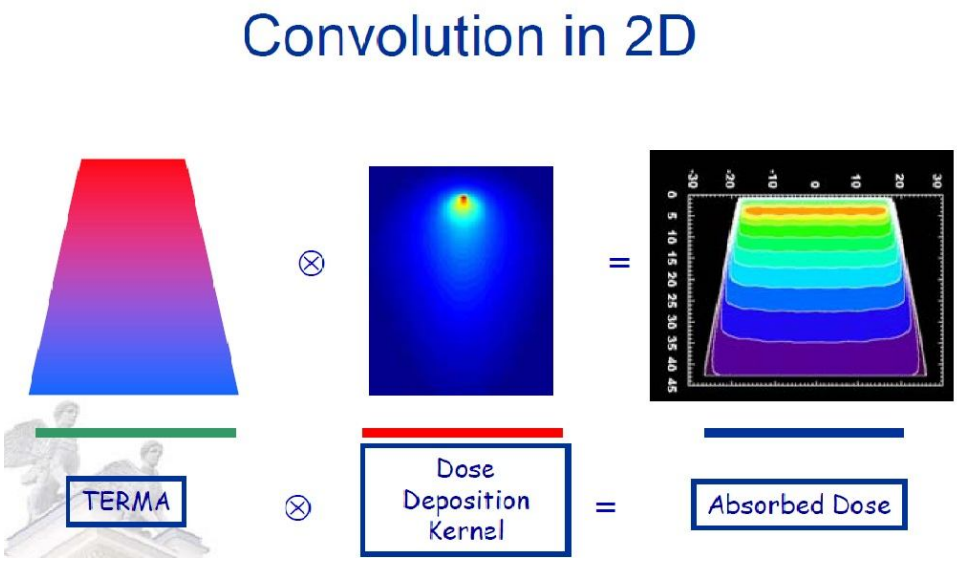

Figure 8. Demonstration of absorbed dose distribution in 2D [(14)]

The TERMA represents the energy released when primary photons exiting the accelerator head interact at some point within a volume. It is influenced by the energy fluence spectra. The EDKs represent the energy deposited about a primary interaction site (PW Hoban *et al*, 1994)[13]. Hoban *et al*,1994[13] reported that, EDKs could be obtained by a Monte Carlo simulation by forcing primary photons to interact at a point and recording the distribution of energy deposited about this point. If the primary photons used to generate the EDKs have a spectrum of energies, then it is called a polyenergetic EDK, while if the primary photons contain a single energy, then it is called a monoenergetic EDK. Hoban *et al*,1994[13] have also reported that, separate primary and scattered EDKs can be produced by keeping track of whether the charged particle that

deposit its energy was set in motion by a primary or a scattered photon. Primary photons here represent photons exiting the accelerator head, while scattered photons represent those scattered by Compton scattering within the volume. The total EDK is the sum of both primary and scattered EDKs.

Convolution calculation requires an accurate determination of TERMA, which accurately accounts for spectral hardening. This requires using an accurate incident spectrum along with linear attenuation coefficients that correspond to each of the energy components of the incident beam for calculation of TERMA (PW Hoban *et al*, 1994)[13]. Thus, beam hardening can be fully accounted for if the dose calculation is the sum of convolutions for each energy component (Mohan *et al*, 1986)[9].

In order for kernel based convolution-superposition planning software to work, it requires a spatially varying photon energy fluence spectrum calculated by ray tracing from the photon source. The photon source is approximated using a multiple source model (Liu *et al*, 1997)[15]. This includes a point source for the modeling of the primary photons from the target, a Gaussian-shaped source for modeling the extra focal radiation corresponding to the scattered photons in the flattening filter, primary collimator and secondary jaws, and a third source to model the electron contamination. This multiple source model contains free parameters that can be adjusted to correspond to individual treatment unit characteristics.

Some radiation therapy planning software employ algorithms that can automatically optimize parameter values for the clinical machine based on comprehensive water-phantom measurements; Eclipse® adopts this approach on their

system. Other planning software may employ manual beam model parameter fitting. This is accomplished based on evaluating the agreement between calculated PDDs and dose profiles with measurements. This approach requires fewer measurements, but more time is spent on fitting parameters. Pinnacle[3] allows this approach on their planning system. Moreover, some venders require sending the measured data for centralized processing in order to develop a machine model.

Kernel-based superposition calculation methods can be based on the pencil beam approximation or on collapsed cone kernels (AAPM, 2009)[14].

The collapsed cone convolution algorithm refers to the modeling of cones in space using a single ray corresponding to the central axis of each cone. The algorithm uses a number of collapsed cones to characterize the scatter distribution around the primary site of photon interaction as shown in figure 9.

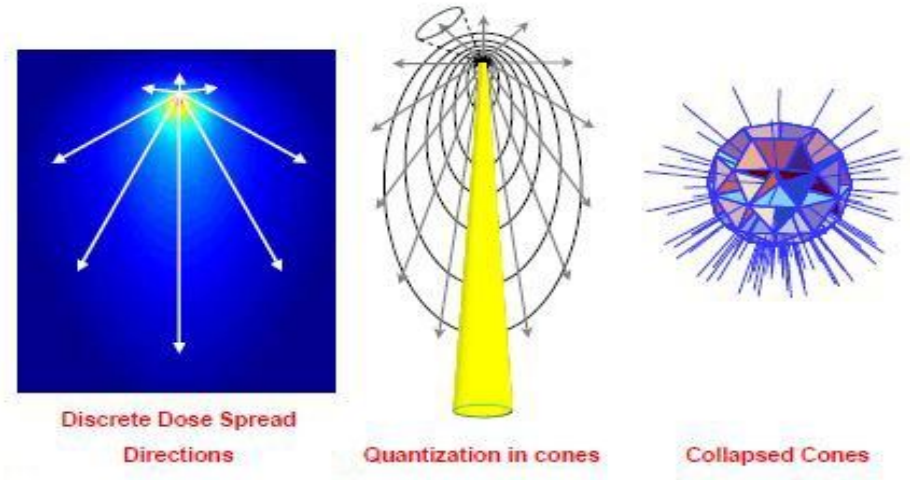

Figure 9. Demonstration of collapsed cone kernels convolution [(14)]

The dose kernels are discretized along a set of collapsed cone axis. For example, CMS: XiO (Elekta - Computerized Medical Systems XiO Release 4.2.0) uses 128 collapsed-cones for scattering contribution to the dose, while OMP (Nucletron - Oncentra MasterPlan V1.4.1.2) uses 106 collapsed-cones (Knöös *et al*, 2006)[21]. Ahnesjo, 1989[16] reported that, "all energy released into coaxial cones of equal solid angle from volume elements on the cone axis is rectilinearly transported, attenuated and deposited in elements on the axis". However, calculation speed is influenced by the number of lines. Moreover, the algorithm accounts for heterogeneities by scaling the cone axis with density to account for electron transport laterally and longitudinally (AAPM, 2009)[14]. Therefore, collapsed cone convolution is appropriate for determining the dose in heterogeneous media.

The kernels are pre-computed using Monte Carlo simulation of monoenergetic photon energy distribution. A poly-energetic kernel is pre-computed based on the energy fluence weighting of specific energy bins. The kernels are not aligned with the diverging photon ray-path; the same orientation is used for all depths at each angle. Papanikolaou *et al*, 1993[17] proposed applying an inverse-square correction at the dose deposition site in the final step of the calculation to handle the titling problem (Papanikolaou *et al*, 1993)[17]. Several others have suggested that further correction requires more computation power and time. For example, Liu *et al*, 1997[18] reported a more appropriate beam divergence correction algorithm to handle the kernel-tilting problem. However, they have reported that, their kernel-tilting correction increases computation time by a factor of 3 (Helen Liu *et al*, 1997)[18]. Collapsed cone convolution calculation could be implemented using several approaches that apply different solutions to the problem.

The convolution calculation would be used to determine the photon dose, while dose from electron contamination source would be used to increment the photon dose close to the surface. For more details regarding collapsed cone convolution functionality and solution, refer to section 4.1.1 and 4.2.

The Pinnacle treatment planning system uses collapsed cone kernels. However, the adaptive CCC (collapsed cone convolution) algorithm used in Pinnacle applies a further approximation to reduce the computational times. In practice, each voxel is crossed by one ray corresponding to each cone axis. The TERMA is calculated at regular points along each ray and its resulting energy deposition is directed into the associated cone axis to increment the dose along the axis. The point dose is the sum of contributions from each ray for each cone axis. Dose due to each ray is the accumulation of the effect of TERMA at all points on the ray (M J Butson *et al*, 2000)[19]. However, Pinnacle performs a convolution only at every 4th point in the TERMA array (AAPM, 2009)[14]. The Pinnacle adaptive CCC algorithm uses a dose gradient differences method to reduce the calculation time further. At high dose gradients (e.g., high-density gradients or at beam edges), convolution is performed at every point, while at low dose gradients, dose is interpolated over four points, since TERMA does not change significantly (Knöös *et al*, 2006)[21] and (AAPM, 2009)[14]. Butson *et al*, 2000[19] reported that, no difference in results was observed when using either the full or the adaptive method.

The second kernel based method uses a pencil beam approximation (PB). The algorithm divides the beam into small beamlets, while the patient body volume is divided into a matrix of 3D calculation voxels along these beamlets. The selected calculation

grid dimensions determine the dimensions of these beamlets. Furthermore, this grid geometry is divergent in order to align the coordinate system with the beam fan-lines. Every voxel is associated with a mean electron density determined from the CT images according to a defined calibration curve. The final calculated dose distribution is a superposition of the dose deposited by the primary and secondary photons along with the contaminant electrons for every beamlet (Van Esch, *et al*, 2006)[20]. This method provides a shorter computation time in comparison with the collapsed cone convolution.

Varian has adopted this approach into their planning system. Their calculation model is named single pencil beam (SPB). Their pencil beam is parameterized according to five depths; as a result, the convolution with the incident fluence is only performed at theses depths. However, interpolation is performed for the depths in between (Knöös *et al*, 2006)[21]. The pencil beam is extracted from measurements in a similar way to the extraction of the scatter formalisms (Knöös *et al*, 2006)[21]. This method considers the variations in density along the pencil beam fan-line. However, several studies show that this leads to a significant limitation in calculation accuracy for heterogeneous media. This is because the pencil beam uses only one-dimension to account for the density correction, while side and back-scatter are not accounted for.

Varian has implemented another algorithm named anisotropic analytical algorithm (AAA). It is also based on a pencil beam convolution technique. Yet, the kernel data are computed from Monte Carlo calculations, while model parameters are adjusted to fit the measurements. Moreover, the longitudinal and lateral extensions of the pencil kernel are scaled with the density relative to water in directions that are normal to the pencil beam. By using this approach, the changes in lateral energy transport with density variation are

modeled in the irradiated object (Knöös *et al*, 2006)[21]. The Eclipse AAA algorithm separates the energy deposition into depth dependent component calculated along the central fan-line and lateral component perpendicular to the fan-line. The lateral energy transport is modeled by photon and electron scatter kernels discretized in 16 lateral directions (Van Esch *et al*, 2006)[20].

1.5 - Uncertainties in Radiation Therapy:

In radiation therapy, dosimetry techniques have been developing rapidly over the last few years. These developments began with conventional three dimensional conformal radiation therapy (3DCRT) and led to more advanced techniques such as Intensity Modulated Radiation Therapy (IMRT) and Volumetric Modulated Arc Therapy (VMAT). These techniques have allowed us to deliver a more conformal dose distribution to the target volume while better sparing the surrounding at risk normal tissue in patients receiving's radiotherapy (Jin *et al*, 2008)[22]. Sparing normal tissue helps to minimize toxicities, but the increased treatment complexity has an impact on treatment planning, quality assurance and delivery (McNiven *et al*, 2010)[23]. Furthermore, it has been shown that there is a tradeoff between complexity and treatment quality when achieving the desired planning objectives (Craft *et al*, 2007)[24]. The increased complexity of advanced techniques such as IMRT and VMAT may lead to an increase of potential uncertainties, which may in turn negate the clinical benefit (Jin *et al*, 2008)[22].

1.5.1 - Source of Uncertainties in Radiation Therapy:

Uncertainties in radiation therapy can arise during planning and/or delivery stages. In general, they can be categorized as follows: First, geometric uncertainties

relate to variation due to the mechanical limitations of the linear accelerator (e.g. the rotation of the gantry head and collimator, the movement of the collimator jaws and multileaf collimator (MLC), patient couch movement and laser alignment). This uncertainty requires that the linac be subject to a regular quality assurance program to ensure performance within recommended tolerances (e.g. AAPM TG #40 "COMPREHENSIVE QA FOR RADIATION ONCOLOGY").

Second, dosimetric uncertainties, which are due to the limitation of how accurately the treatment geometry can be modeled. These limitations depend on organ of interest characteristics (i.e. target volume complexity and tissue density variations).

Third, dosimetric uncertainties not related to treatment geometry, but could be due to unreliable measured data used to commission the model in the planning software (such as when partial volume affects influence the dose measured using an ion chamber in a region of high dose gradient). An inappropriate choice of beam modeling parameters can further contribute to the inaccurate calculation of a dose distribution or monitor units (MU) (Boyer and Schultheiss, 1988)[25].

In this work, the uncertainty in choosing model parameters and its implications on phantom dose distribution and MU calculation will be investigated.

1.6 - Research Focus and approach:

The photon fluence spectra used in Pinnacle machine model was found to be harder than that predicted by Monte Carlo simulation based on BEAMnrc code. The Pinnacle spectrum was generated using the auto modeling function that matches computed and measured PDD data. An alternative approach is to attenuate the Monte

Carlo BEAMnrc spectrum to best match PDD data. In this work, we study the implication of adopting such a spectra on PDD, dose profile and output factor calculation. Furthermore, the use of the MLC has been extended as advanced techniques are developed. Rather than being a device only used to shield anatomical structures, it is now being used to generate in-field modulation of the incident photon fluence. Therefore, in this work, we also study the implication of adjusting the effective leaf tip radius of curvature and the MLC offset table (which offset the leaf in order for the projected light field to agree with the nominal programmed leaf position) on computation of dose profile and the output factor.

Rather than relying only on conventional methods to validate our new model, setups have been created to study the effect of model parameters on MLC abutment leakage and output factors calculation for long and narrow MLC defined fields, and square MLC and jaws defined fields along with measurements. These setups are used to fine-tune the model.

CHAPTER 2: MATERIAL AND EXPERIMENTAL SETUP

2.1 - Pinnacle Planning Software:

The main focus of this thesis is to enhance the existing clinical machine model within the Pinnacle radiation therapy planning software (at Juravinski Cancer Center, Hamilton, CA). The new optimized model was examined against the clinical model in order to further improve the calculation accuracy of 6 MV intensity modulated photon beam.

Pinnacle is a model based planning system that uses model parameters to fit measured PDD and dose profile data from the linear accelerator. The model parameters are determined by either iterative manual adjustment or by using the provided auto tuning function.

2.1.1- Photon Energy Spectrum Modeling:

An important element of the machine model is the incident energy fluence exiting the accelerator head defined in a plane perpendicular to the beam at the isocenter. In the auto modeling sequence, Pinnacle adjusts the fluence to account for the effects of the flattening filter (Pinnacle^3 Physics Reference Guide)[6].

To model the incident energy fluence spectrum, the Pinnacle manual suggests starting with one of the published spectra that corresponds to the nominal energy of the beam. By comparing the measured and the computed depth doses for various square field sizes, adjustments to the relative number of photons in successive energy bins are made, until the set of depth doses match well at depths beyond the depth where

electron contamination contributes dose. This is because the buildup region electron contamination dose is further adjusted separately.

Flattening filter attenuation changes the photon fluence and the photon energy distribution as a function of off-axis distance. The radial fluence can be accounted for by using an arbitrary profile where relative number of incident photon is adjusted as a function of radial distance from central axis. A Spectral Off-Axis Softening Factor parameter accounts for the changes in the distribution of photon energies as function of radial distance (Pinnacle^3 Physics Reference Guide)[6].

The effective source size parameters model the shape of the penumbra. They can be adjusted independently in directions perpendicular to the gantry axis (X-axis) and parallel to the gantry axis (Y-axis). Increasing the effective source size makes the shoulders and the tails of the dose profile more rounded, while decreasing it makes them more square. Thus, geometric penumbra is proportional to the source size.

The flattening filter scatter source parameter is modeled by a 2D Gaussian function characterized by a Gaussian height, which defines the fraction of the central axis energy fluence that is due to the flattening filter, and a Gaussian width, which specifies the width (in centimeters) of the Gaussian curve that is used to model the flattening filter source. The effect of this scatter source is most pronounced at the tails of the dose profile. By integrating over the region of the scatter source visible from the calculation point, Pinnacle determines the amount of the head scatter radiation reaching any point in the incident fluence plane. Furthermore, the scatter source affects the computation of output factors (Pinnacle^3 Physics Reference Guide)[6].

The field is shaped by cutting out the fluence array under jaws blocks or MLC, leaving behind the corresponding transmitted fluence. In case of the use of beam modifiers, such as wedges or compensator, the energy fluence array is attenuated using the corresponding thickness of the modifiers (Pinnacle^3 Physics Reference Guide)[6].

This thesis is limited only to the modeling of a 6 MV photon beam energy for a Varian 21EX machine. A new method for determining the Pinnacle photon energy fluence spectrum is proposed. This fluence spectrum is compared to that of clinical machine, which was determined by conventional means. This novel photon energy fluence spectrum will be discussed later on in section 2.3.

2.1.2 - MLC Modeling Parameters:

Pinnacle planning software provides tools and options to define and characterize different types of MLC devices from various venders. The Varian 21EX is equipped with a Millennium MLC that contains 120 leaves. The leaf motion is parallel to the lower x-axis jaws and perpendicular to the upper Y-axis jaws. The leaves have a thickness of 5.65 cm and the bottom edge are 53.83 cm from the source in a plane perpendicular to the central axis. The maximum leaf tip position is 20 cm (projected to the isocenter plane), which defines how far the leaves can be opened; and a minimum leaf tip position of -20 cm, which defines how far the leaves can go across the center of the beam. However, 15 cm is the maximum difference in distance between two adjacent leaves on the same carriage when one leaf is fully extended, while the other is fully retracted. Therefore, if more than 15 cm of travel is required, the whole carriage must be shifted in order to extend this limit.

The Pinnacle defined MLC can be configured to conform to these limits. Moreover, MLC intra-leaf and jaw transmission factors specify the fraction of the energy fluence transmitted. Interleaf leakage transmission, and tongue and groove characteristics are accounted for in the modeling process. The additional interleaf leakage transmission is added to the MLC transmission in the small area where leakages occurs and the total thickness through the tongue and groove is less than the total thickness of the center of the MLC leaves in regions where two adjacent leaves intersect, as shown in figure 6.

Varian MLC leaves have rounded leaf ends (as discussed in section 1.1.2). However, the actual profile shape of the leaf is not perfectly circular. Nevertheless, the Pinnacle model approximates the rounded leaf profile shape by modeling it as a circle segment that extends between the top and the bottom surfaces of the MLC separated by leaf thickness as shown in figure 10.

The transmitted radiation is reduced by the MLC Transmission Factor, while at the leaf ends, transmitted radiation is attenuated by the thickness of the leaf at each point in the tip (Pinnacle[3] Physics Reference Guide)[6].

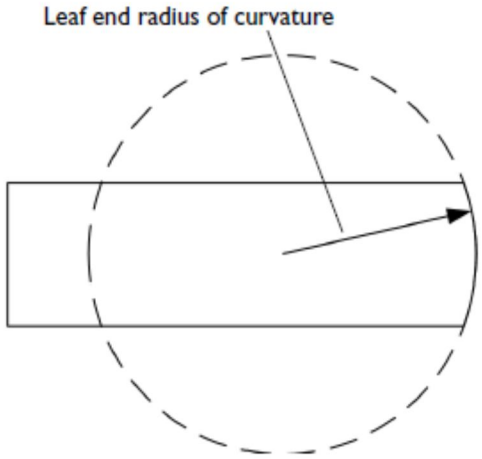

Figure 10. Demonstration of pinnacle rounded leaf end approximation (Pinnacle[3] Physics Reference Guide)[6]

For Varian MLC leaves, the leaf end radius of curvature is 8 cm according to literature (LoSasso T *et al*, 1998)[26]. The pinnacle model allows this parameter to vary from 4-20 cm in order to achieve optimal agreement with the measured dose profiles. The clinical machine used at the Juravinski Cancer Center model has the leaf end radius set to 6 cm. However, adjusting the radius to give the best fit of the dose profile may not lead to the best model. The impact of adjusting this parameter will be investigated and discussed in sections 2.5 and 2.6.

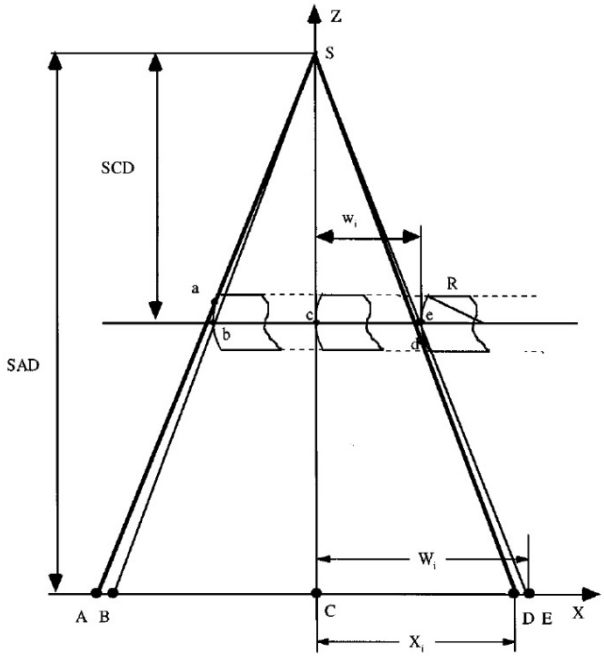

Figure 11. Diagram shows the relation between the light field edge (X) and the leaf-tip projection (W) at isocenter level (Boyer and Li, 1997)[5]

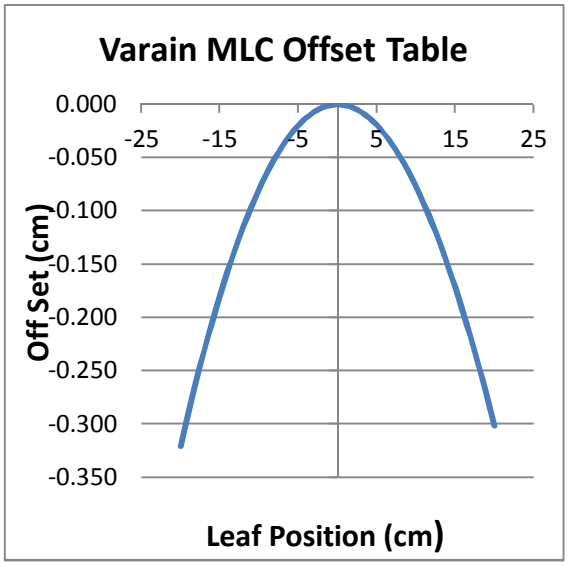

Graph 4. Represent Varian MLC calibration table that specifies the relationship between the leaf tip projection and the light field edge at the isocenter [27]

As shown in figure 11, the geometric dimension of the field is specified by the projection of the center of the leaf tip at points (b, c, and e) to the points (B, C, and E) at the isocenter plane respectively. Where SCD represents the distance from the x-ray source to the center of the leaf. However, the ray tangent to a point at the leaf end

specifies the light field edge for each leaf position. These tangent points at (a, c, and d) for the leaf positions at (b, c, and e) respectively have an isocenter projection at points (A, C, and D) respectively, which shows that this tangent point moves around the rounded end as the leaf moves. Nevertheless, it is also clear that the difference between the tip point and the tangent point increases as the leaf position moves further from the center of the field (Boyer and Li, 1997)[5]. The Varian MLC controller device uses an offset table to specify the relationship between the leaf tip position and the light field edge projected to the isocenter level. This default calibration table is set up to position the MLC leaves so that the projected light field size agrees with the nominal programmed leaf position. Graph 4 shows the Varian mlctable.txt representing the MLC leaf tip default offset table. Note that the sign of the offset values is such that the leaves are always retracted in the direction of the offset.

The leaf positions stored and exported by Pinnacle match the nominal leaf positions programmed for the accelerator. Therefore, the Pinnacle model must account for the differences between leaf tip point and the tangent point by introducing a leaf offset table. For dose computation, the actual leaf position is the nominal position plus the offset determined from the same leaf offset table as used by the MLC controller (Pinnacle^3 Physics Reference Guide)[6]. In this work, we study the impact of adjusting the default Varian table on output factors and dose profiles.

Section 2.4 of this thesis provides a summary of the Pinnacle machine model investigated in our study. These include the photon energy spectrum, rounded leaf tip radius, and MLC offsets. The effect of these parameters on MLC abutment leakage and output factors is discussed in detail on section 2.5 and 2.6.

2.1.3 - Output Factor Computation:

For the calculation of absolute dose distributions, Pinnacle multiplies the standard incident energy fluence by an output correction factor before performing the convolution. The dose distribution is in units of cGy/MU. Therefore, the true energy fluence/MU exiting the accelerator head is accounted for by scaling the incident energy fluence by the output correction factor (OFc) (Pinnacle^3 Physics Reference Guide)[6].

The absolute calibration factor is specified at a reference depth (usually 10 cm) and a reference field size (10 x 10 cm^2) in units of cGy/MU. Pinnacle calculates the dose to the calibration point first, and then compares this dose to the user specified calibrated output dose. Then the software corrects the ratio of measured and computed data using the incident energy fluence. This absolute calibration factor is used for every field size when creating the incident energy fluence image. The final incident energy fluence for each beam is therefore the product of the fluence from the standard head model, the absolute calibration factor, and the field-size dependent OFc (Pinnacle^3 Physics Reference Guide)[6].

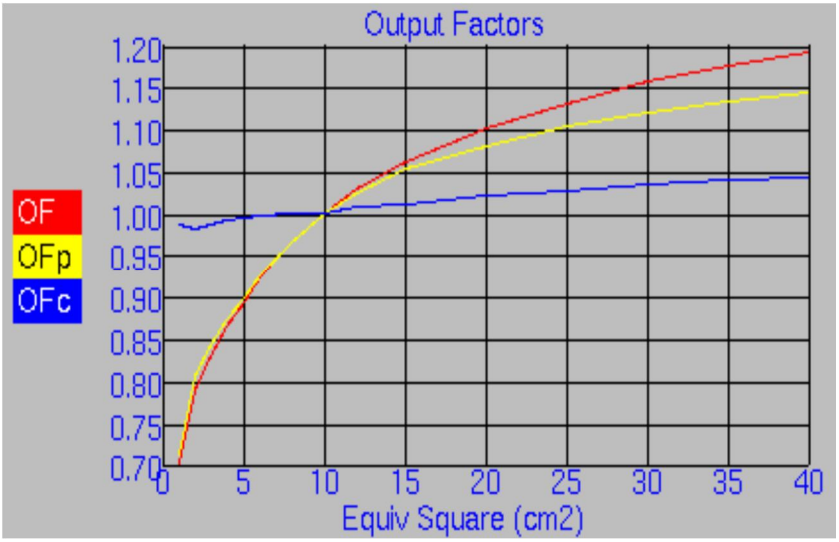

Graph 5. 21EX-JCC clinical machine Pinnacle computation of output factor computation [(27)]

Graph 5 shows the output factor and output factor correction behavior with equivalent- square field size. The OF (red curve) represents the measured relative output factor, while the OFp (yellow curve) represents the calculated output factor. Since Pinnacle model does not fully account for head scatter effect, OF is not equal to OFp. Therefore, Pinnacle adjusts its calculated output by the ratio of OF to OFp which is equal to OFc shown as the blue curve on graph 5. Generally speaking, if the model accounts for the head scatter perfectly, OFc should be 1.00 for all field sizes. Therefore, modeling parameters must be carefully tuned to achieve a uniform OFc for all filed sizes (Pinnacle^3 Physics Reference Guide)[6]. However, this tuning may be inconsistent with that needed to fit dose profiles. The degree of inconsistency will be investigated for various machine models using various incident photon energy spectra.

2.2 - Preliminary Investigation of Beam Modeling:

Preliminary beam modeling in Pinnacle lead us to conclude that the best agreement between computed and measured dose can only been achieved by defining two separate machine models. The first machine model is tuned to give better agreement at shallow depths (up to 15 cm in water), while the second machine model is tuned to give the best agreement for depths beyond 15 cm in water. This approach was accomplished by adjusting the effective source size and the flattening filter scatter source parameters. In the second model, more scatter was needed to compensate the lack of scatter at deeper depths. The two models resolved the discrepancy in agreement between measured and calculated central-axis dose profiles, but did not resolve the corresponding discrepancy for off-axis dose profiles as demonstrated in graph 6.

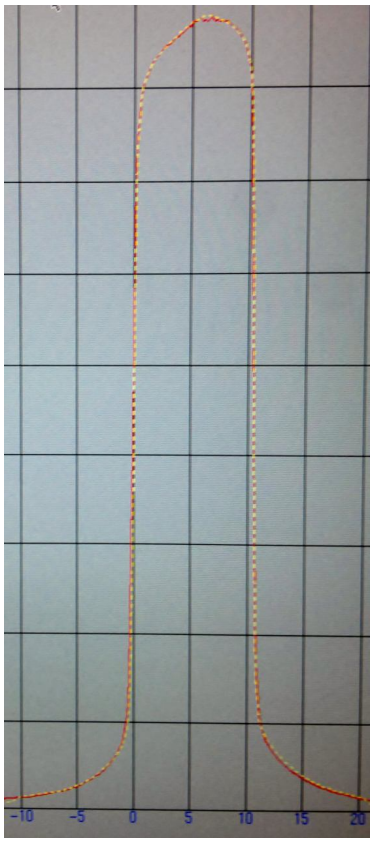

(A): Off axis at depth of 5 cm

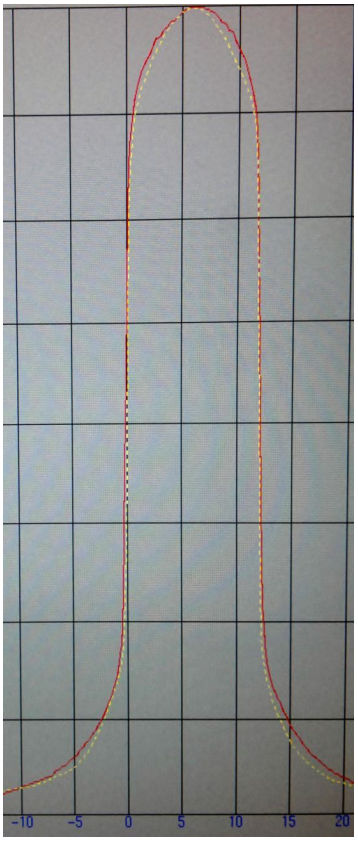

(B): Off axis at depth of 20 cm

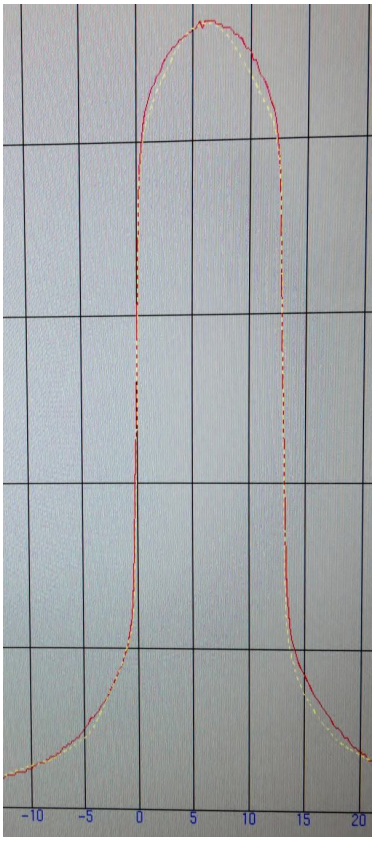

(C): Off axis at depth of 30 cm

Graph 6. Discrepancy in agreement at various depths for 5 x 5 cm^2 off-axis dose profile. The red curve represents the measured data while the yellow represents the computed data. Pinnacle Computation, 21ex- JCC Clinical Machine [27]

Increasing the radial fluence to compensate for the loss of scattering for these off-axis dose profiles at deeper depths does not solve the discrepancy. Moreover, implementing multiple field size dependent models within the same machine does not resolve the discrepancy as well. Therefore, the development of field size dependent models was abandoned.

2.3 - Pinnacle Spectrum Investigation Process:

The Pinnacle photon energy fluence spectrum is defined as the relative number of photons of each energy that exit the linear accelerator head including primary photons from the target and secondary photons scattered by the other head components i.e. flattening filter, primary and secondary jaws, MLC, monitor chamber and so on. The 21ex-JCC clinical machine spectrum was compared with a 6 MV Monte Carlo photon fluence spectrum derived from BEAMnrc code simulation of Varian 21EX linear accelerator (Sheikh-Bagheri *et al*, 2002)[10]. As demonstrated in graph 7, the blue curve corresponds to the 21ex-JCC clinical machine 6 MV relative photon fluence spectrum used at the Juravinski Cancer Center for Pinnacle modeling. The red curve corresponds to the BEAMnrc 6 MV spectrum that exits the accelerator head, while the green curve represent the primary photon spectrum coming out of the target (Varian documents)[29].

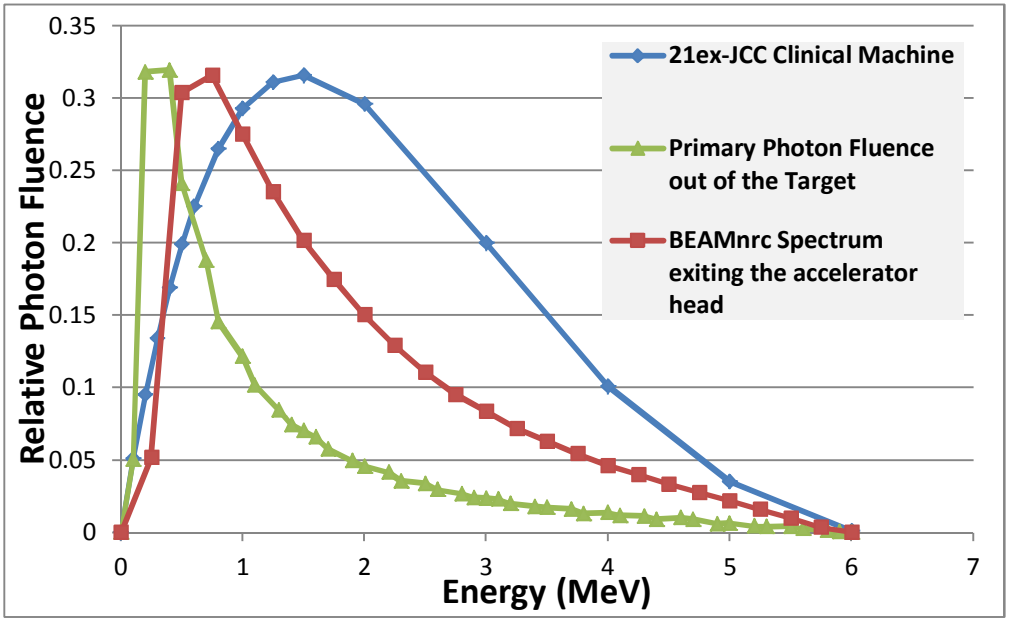

Graph 7, 6 MV photon fluence spectra. Blue curve represents the 21ex-JCC clinical machine spectrum. The red curve corresponds to BEAMnrc spectrum (Sheikh-Bagheri *et al*, 2002)[10]. The green curve represents the primary target fluence spectrum (Varian Eclipse AAA Beam Configuration)[28]

The primary target and BEAMnrc photon fluence spectra were renormalized so that the peaks correspond to that of the 21ex-JCC relative photon fluence spectrum for the comparison purposes. The graph shows that the BEAMnrc spectrum is harder than the target primary photon spectrum, since low energy photons are preferentially attenuated by the flattening filter. However, the 21ex-JCC clinical machine spectrum used in Pinnacle planning is much harder in comparison with BEAMnrc spectrum, yet it gives an acceptable agreement between the computed depth dose and dose profile data in comparison to the measurements.

In this work, we studied the effect of replacing the 21ex-JCC spectrum in Pinnacle with the BEAMnrc photon fluence spectrum, which is physically more realistic. The realistic spectrum was then attenuated through various thicknesses of water to best fit calculated to measured depth dose curves.

2.3.1 - Validation of Photon Fluence Spectrum:

To validate the use of the BEAMnrc photon fluence spectrum as input to the Pinnacle model, a coarse calculation of TERMA was performed using both the existing 21ex-JCC and BEAMnrc spectrum. The TERMA ray on central-axis was calculated and compared with measured PDD for 1 x 1 cm^2 field size. This was done to minimize the lateral contribution of scatter to the central-axis depth dose. The relative photon fluence spectrum was first converted to an energy fluence spectrum by multiplying the relative number of photons within an energy interval by the energy of the interval.

The energy fluence was calculated as a function of energy and depth using the following equation:

$$\Psi(E,d) = \Psi_0(E)e^{-\mu(E)d}\left(\frac{SSD}{SSD+d}\right)^2 \qquad (1)$$

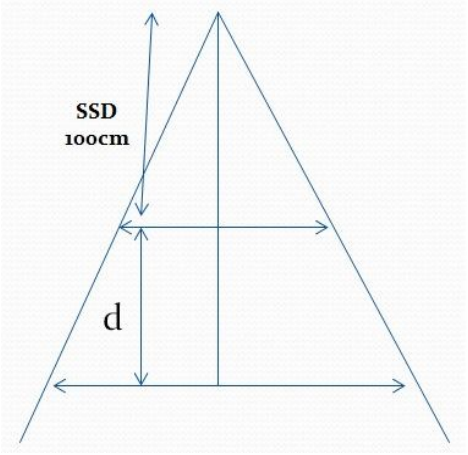

Figure 12. Energy fluence calculation

Where Ψ_0 (E) represents the initial energy fluence spectrum at the phantom surface based on either the 21ex-JCC or BEAMnrc relative photon fluence spectrum as a function of energy bin E,

μ(E) represents the attenuation coefficient in water as a function of the photon energy bin (NIST)[29], **d** corresponds to the depth in water and **SSD** represent the distance from the source to the surface (=100 cm). The inverse square law correction was implemented to take into account the beam divergence with distance from a point source. The setup was simplified as shown in figure 12.

The total TERMA was calculated as a function of depth for up to 30 cm in water by using the following equation:

$$T(d) = \sum_E \Psi(E,d)\, x\, \frac{\mu(E)}{\rho} \qquad (2)$$

Where **μ/ρ** represents the mass attenuation coefficient of water (NIST)[29].

The BEAMnrc 6 MV photon fluence spectrum tabulated in table 2 has a uniform energy bin width of 250 keV. Since energy bins are of equal width, the photon fluence from

each bin is multiplied by the bin energy to yield energy fluence for the TERMA calculation.

For the Pinnacle 21ex-JCC photon fluence spectrum, the energy bins are not of equal width. Accordingly, the calculated energy fluence as a function of energy must be appropriately weighted before determining the TERMA. The calculation of the energy fluence weighted spectrum was done using the following equation:

$$\Psi(E) = \frac{\frac{\Delta\varphi(E)}{\Delta E} \cdot \Delta E_i \cdot E_i}{\sum \frac{\Delta\varphi(E)}{\Delta E} \cdot \Delta E_i} \qquad (3)$$

Where **Δϕ/ΔE** represents the photon fluence in energy bin of width **ΔE**. $\mathbf{E_i}$ represent the energy of the bin containing the photon fluence.

The results and analysis will be presented in section 3.1.

2.3.2 - Implementation of BEAMnrc Spectrum in Pinnacle:

The BEAMnrc spectrum shown in graph 7, resulted in an under estimation of Pinnacle calculated percentage depth dose in comparison with the measurement as illustrated in graph 8. Accordingly, harder spectra were derived by attenuating the BEAMnrc spectrum by different depths of water in order to determine an equivalent depth of water to which the ideal spectrum corresponds. The spectrum was attenuated by up to 20 cm depth of water and the resulting spectra were normalized to the 21ex-JCC spectrum as shown in graph 9. These spectra were applied and examined using Pinnacle beam modeling application. The implications and analysis will be presented in section 3.2, 3.3 and 3.4.

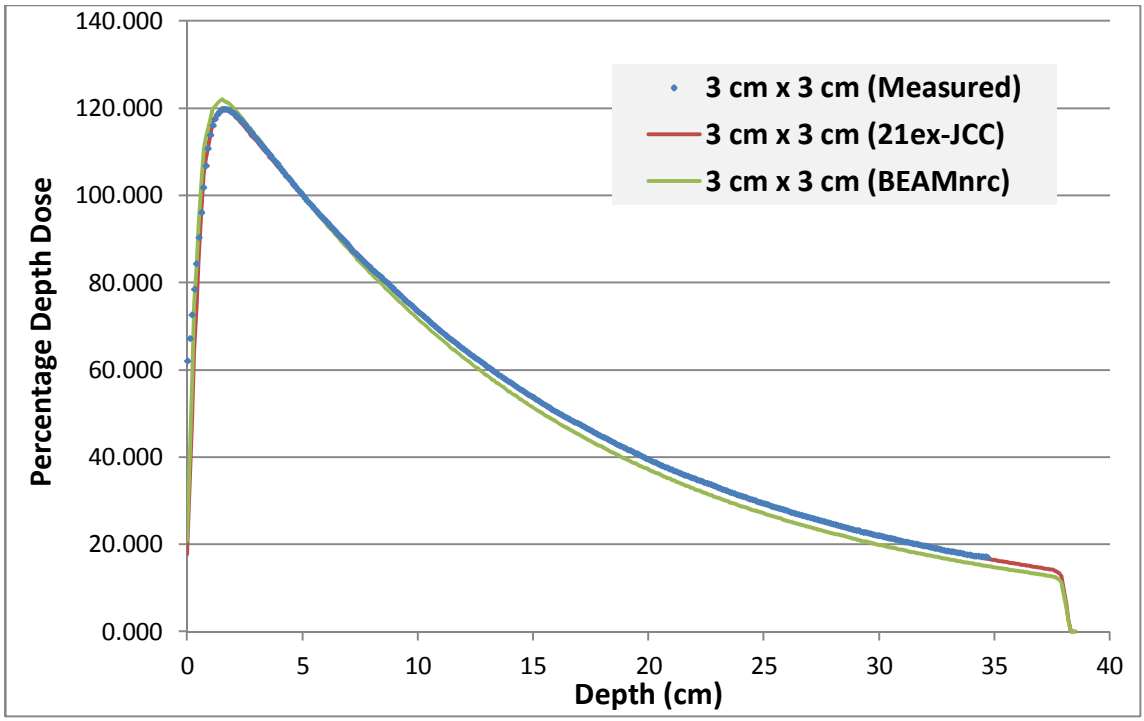

Graph 8. A comparison of 3 x 3 cm^2 field size depth dose normalized to 5 cm depth calculated using either the 21ex-JCC (red line) or the BEAMnrc (green line) spectra. The measured curve is also plotted (blue dots)

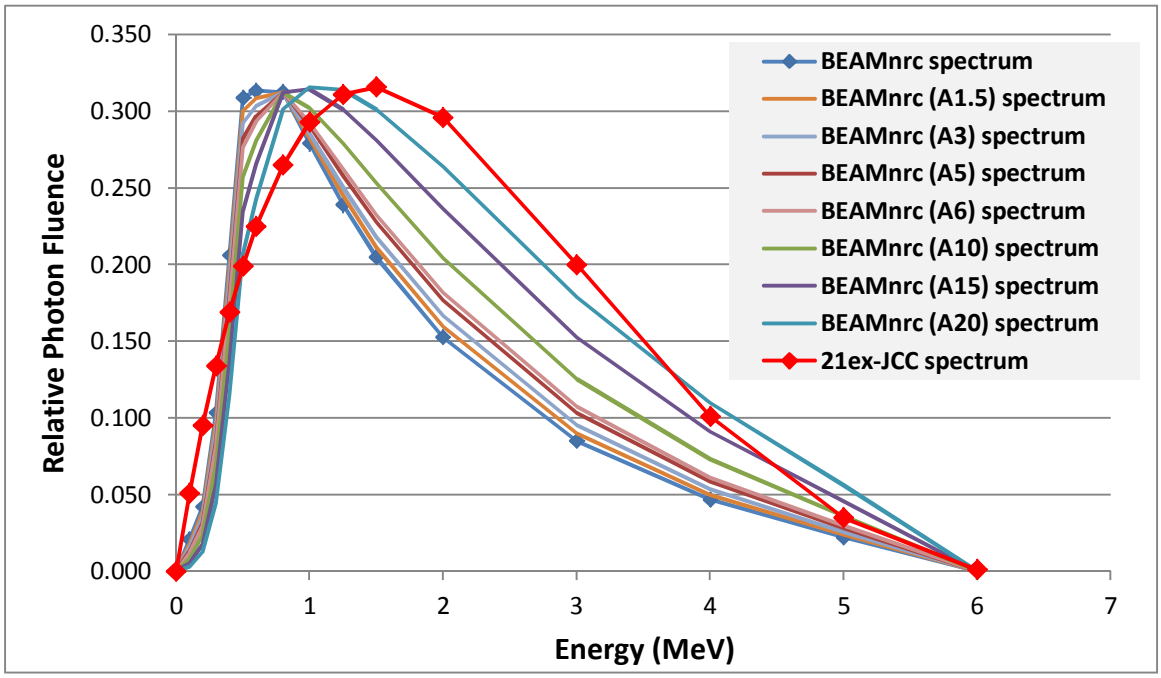

Graph 9. A comparison between the 21ex-JCC, BEAMnrc and various harder spectra derived by attenuating the BEAMnrc spectrum by different depths of water (e.g. BEAMnrc (A15) means the BEAMnrc spectrum attenuated by 15 cm depth in water). The resulting spectra were normalized to the 21ex-JCC spectrum

2.4 - New Machine Model Parameters Definitions:

The 21ex-JCC clinical machine was used as the starting point for studying the effect of energy fluence spectrum, MLC leaf tip radius, and the MLC calibration offset table. The other parameters were kept the same as the clinical machine.

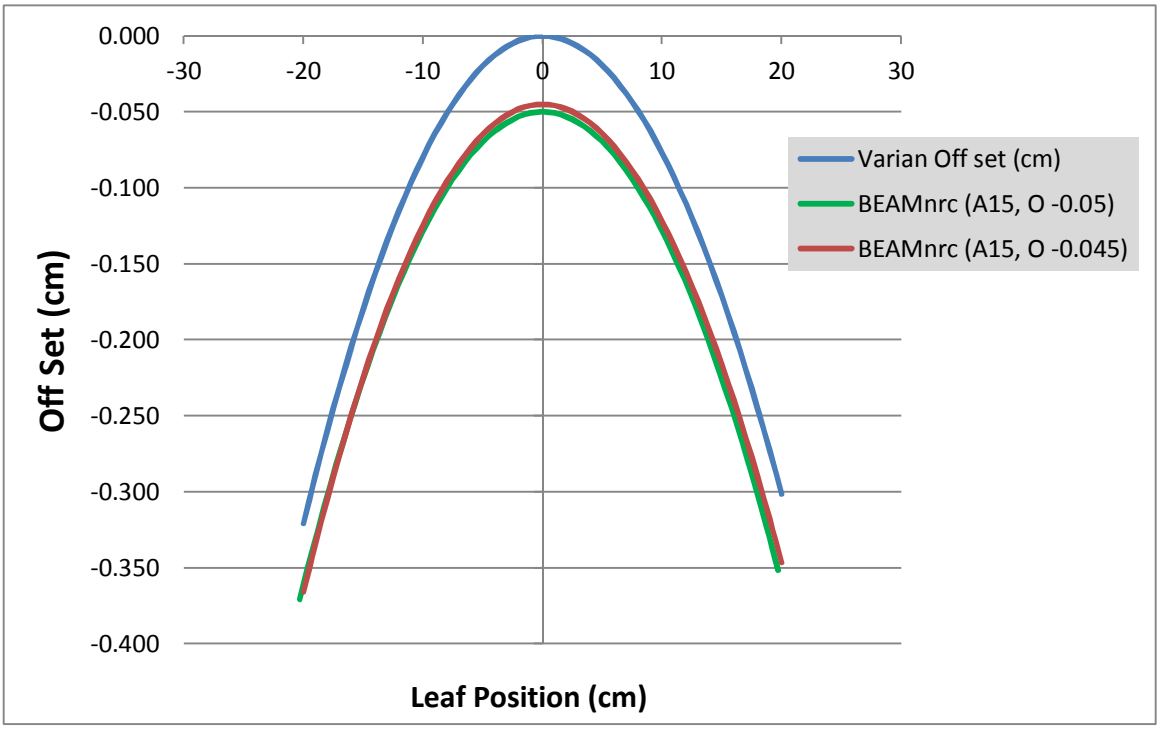

Graph 10. Adjustment to the MLC calibration offset table implemented in Pinnacle, i.e. the (O -0.05) means that 0.05 cm was subtracted from the original offset table and so on

Graph 10 shows how the MLC calibration offset table (presented in graph 4) was adjusted. The adjustments resulted in changes to the projected MLC defined field size at the isocenter level (100 cm). For example (O -0.05) means that 0.05 cm was subtracted from the original Varian offset table, resulting in a slight increase to the projected MLC defined field size of 1 mm (0.05 cm leaf shift from banks A and B respectively) on the x-axis plane direction.

The differences in the MLC calibration offset table should affect the computed dose profiles as well as the output factors for small MLC defined fields. Similar effects may be observed due to changes in leaf tip radius.

Table 3 below summaries the machine models that were studied in this thesis:

Machine	Description			
	Energy Spectrum	Off-Axis Softening Factor parameter	Leaf Tip Radius	MLC Calibration Table
21ex-JCC	Pinnacle 21ex-JCC clinical spectrum	8.45312	6.5 cm	Varian original offset table
BEAMnrc (R6.5)	BEAMnrc relative spectrum	8.45312	6.5 cm	Varian original offset table
BEAMnrc (A15, R6.5)	BEAMnrc relative spectrum attenuated to 15 cm depth of water	8.45312	6.5 cm	Varian original offset table
BEAMnrc (A15, R8)	BEAMnrc relative spectrum attenuated to 15 cm depth of water	8.45312	8 cm	Varian original offset table
BEAMnrc (A15, R8, O -0.05, S6.5)	BEAMnrc relative spectrum attenuated to 15 cm depth of water	6.5	8 cm	0.05 cm subtracted from the whole Varian offset table
BEAMnrc (A15, R8, O -0.045, S6.5)	BEAMnrc relative spectrum attenuated to 15 cm depth of water	6.5	8 cm	0.045 cm subtracted from the whole Varian offset table
BEAMnrc (A15, R8, O -0.045)	BEAMnrc relative spectrum attenuated to 15 cm depth of water	8.45312	8 cm	0.045 cm subtracted from the whole Varian offset table
BEAMnrc (A15, R9, O -0.045)	BEAMnrc relative spectrum attenuated to 15 cm depth of water	8.45312	9 cm	0.045 cm subtracted from the whole Varian offset table
BEAMnrc (A15, R12, S6.5)	BEAMnrc relative spectrum attenuated to 15 cm depth of water	6.5	12 cm	Varian original offset table
BEAMnrc (A15, R12)	BEAMnrc relative spectrum attenuated to 15 cm depth of water	8.45312	12 cm	Varian original offset table

BEAMnrc (A15, R8, S6.5, O -0.045, A.I.L. 0.5%)	BEAMnrc relative spectrum attenuated to 15 cm depth of water	6.5	8 cm	0.045 cm subtracted from the whole Varian offset table. The additional interleaf transmission was set to 0.0005 (0.5%)
BEAMnrc (A15, R8, No offset)	BEAMnrc relative spectrum attenuated to 15 cm depth of water	8.45312	8 cm	The whole MLC offset table set to zero value

Table 3.1. Summaries of the machine models studied in Pinnacle beam modeling. Note that the little gray box means a similar set as of the 21ex-JCC clinical machine. The other parameters were kept the same as the clinical machine

The 21ex-JCC clinical machine model also incorporates the following out of the field beam model parameters characteristics:

Machine	Effective Source Size		Flattening filter scatter source		Transmission factors	
	Perpendicular to gantry axis (cm)	Parallel to gantry axis (cm)	Gaussian Height	Gaussian Width	Jaw transmission	MLC transmission
21ex-JCC clinical machine	0.04	0.04	0.08	1.4	0.007	0.015

Table 3.2. Out of the field machine model characteristic for the 21ex-JCC clinical machine [27]

2.5 - Setup to Determine Effect of Machine Parameters on MLC Abutment Leakage:

MLC abutment leakage is sensitive to leaf model parameters. In order to investigate the effect of energy fluence spectrum, leaf tip radius and MLC offset table, three fields, left, right, and center, were programmed to deliver a series of abutments as shown in figure 13-A. The abutments had a 1 cm spacing and covered the entire 40 cm

field length. Three fields were required to accommodate the MLC leaf carriage motions needed to cover the full field range.

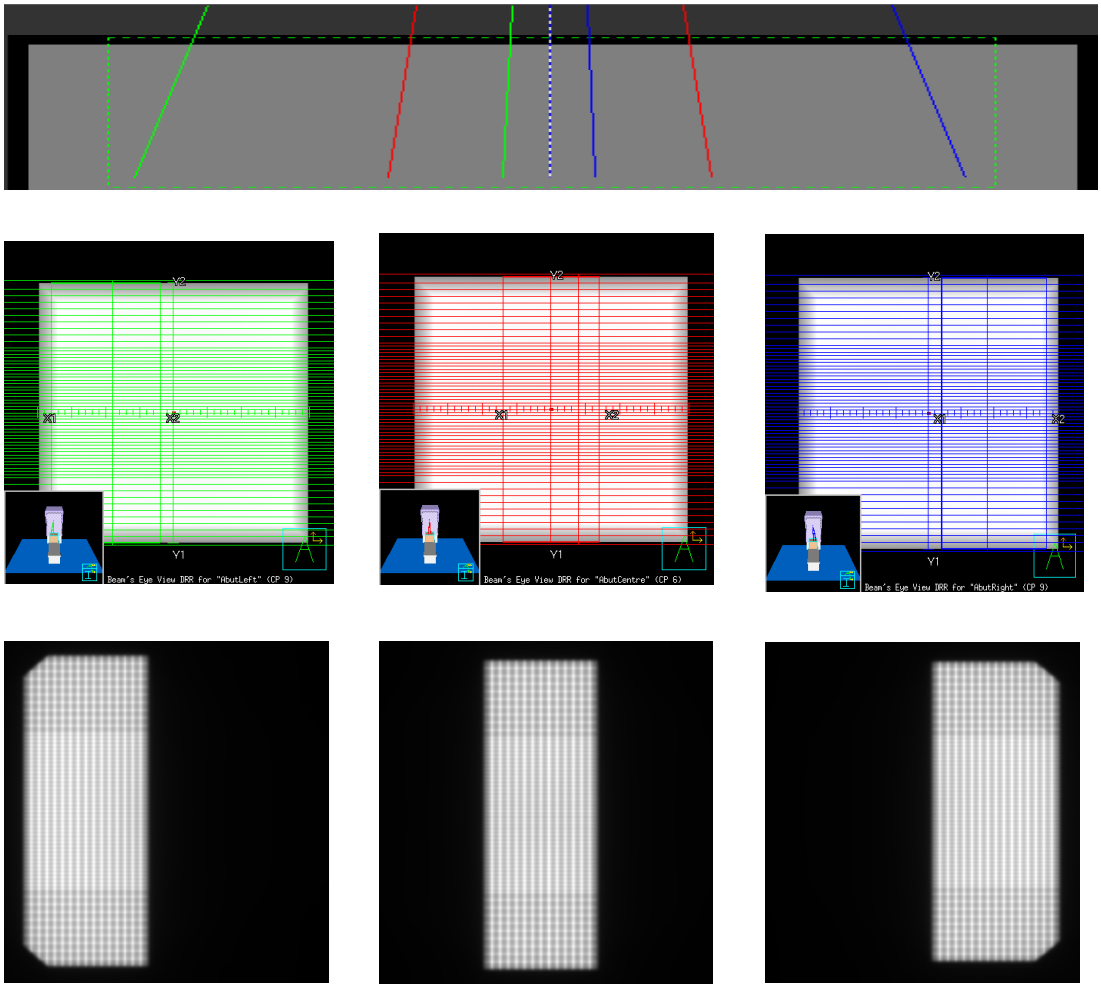

Left abutment setup **Center abutment setup** **Right abutment setup**

Figure 13-A. Setup of the programmed abutment followed by demonstration of dose planer calculation in Pinnacle. The gap between each abutment was set to 1 cm [(27)]

The abutment leakages were first calculated using the machines described in table 3.1, then the planar dose maps at depth of 5 cm were exported for analysis using

image-processing software (ImageJ). This software can be used to calculate statistical information and generate geometrical transformations for different images.

These abutment fields were also delivered to GAFCHROMIC EBT2 films using the linear accelerator. The GAFCHROMIC EBT2 film is self-developing, near tissue equivalent, and water resistant. It can also be handled in room light and has a photon response that is nearly energy independent from about 50 keV into the MeV range [30]. The exposed films were scanned using an EPSON model scanner with film holder to ensure reproducible positioning. The scanned films were saved in TIFF format.

Figure 13-B. Computed 8-step wedge plan used for conversion of films exposure into dose

An 8-step wedge plan that has equal spacing (figure 13-B) was programmed, calculated, and delivered to GAFCHROMIC EBT2 films. This plan contains eight dose levels, which was tuned to address the maximum and minimum transmission observed in our calculated abutment dose profiles. To obtain the conversion of film optical density to measured dose, the red channel data of the scanned images were extracted and processed using ImageJ. The calibration curve was obtained from Pinnacle step wedge dose map and film step wedge exposure using an ImageJ script file. The script program also applied the conversion to each of the delivered scanned abutment field images. Results and details are discussed in section 3.6.

2.6 - Setup to Determine Effect of Machine Parameters on Output Factors:

2.6.1 - Small Square Jaw and MLC Defined Fields:

Output factors for small jaws and MLC defined fields have been reported in a recent publication by Klein *et al*, 2010[31]. They measured the output factors using a plastic scintillation detector (PSD) of 0.5 mm diameter and 2 mm length. Due to its small size, the PSD was less susceptible to volume-averaging effect and perturbation due to the loss of charged particle equilibrium. They performed their irradiations using a Varian Clinac 21EX machine equipped with the millennium 120 MLC collimation system, and 6 and 18 MV photons, identical to the linear accelerator used for the irradiation carried out in this thesis.

Klein *et al*, 2010[31] measured square fields were defined by either jaws or MLC. Their collimated jaw fields comprised of 0.6, 0.8, 1.0, 1.2, 1.5, 2.0, 2.5, 3.0, 4.0, 5.0, 6.0, 8.0, and 10.0 cm on a side, while the MLC leaves were retracted to their maximum (40 x 40 cm^2) to minimize their influence. Their MLC fields were comprised of 0.5, 1.0, 1.5, 2.0, 2.5, 3.0, 4.0, 5.0, 6.0, 8.0, and 10.0 cm on a side, while jaws were set at 20 x 20 cm^2 so it should not influence the measurement. The MLC abutment was placed either at the centerline (MLC-0) or at 4 cm away from the centerline (MLC-4), as shown in figure 14. The detector was positioned at the beam isocenter (100 cm source to axis distance) at a depth of 10 cm in water. In addition, it was placed in the center of the field for all measurements. However, for some particular field sizes defined by the MLC (i.e., 0.5, 1.5, and 2.5 cm on a side) to be centralized, the detector was shifted by 0.25 cm

superiorly as represented in figure 14. Moreover, their output factors for fields defined by jaws were normalized to 5 x 5 cm^2 fields. While for fields defined by MLC, the output factors were normalized to 5 x 5 cm^2 set by MLC.

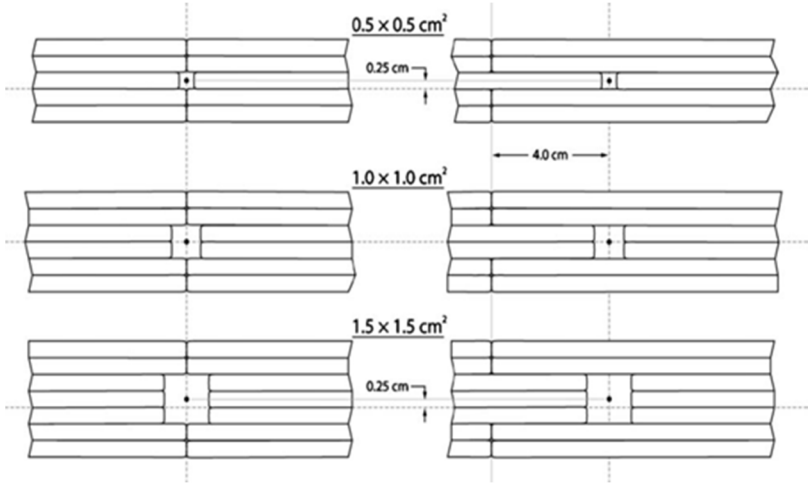

Figure 14. Demonstration of MLC-0 and MLC-4 setup (Klein *et al*, 2010)[30]

Klein *et al*, 2010[31] irradiations were reproduced in Pinnacle to assess the accuracy with which the new beam model could calculate small field output factors. The measurements were also reproduced using a Sun-point diode detector. The detector has an active size of 0.8 x 0.8 mm^2 and an active volume of 0.000019 cm^3 making the diode a better selection than an ion chamber for accurate measurement of small field output factors. Figure 15 demonstrate some of the improvements obtained by employing a small volume detector to measure small fields [(32)].

In addition, the Sun-Point diode detector provides excellent stability (± 0.5% over 100,000cGy) and sensitivity characteristics (32nC/Gy) while suffering negligible energy and dose rate dependence. The Pinnacle calculated output factors dose were normalized relative to 10 x 10 cm^2 field using jaws for fields defined by jaws, or MLC for fields defined by MLC. The Klein *et al*, 2010[31] output factors data were renormalized

to a 10 x 10 cm^2 field and compared with both Pinnacle computed output factors using the new models and the Sun-point diode detector measurements. Results will be discussed in section 3.7.1.

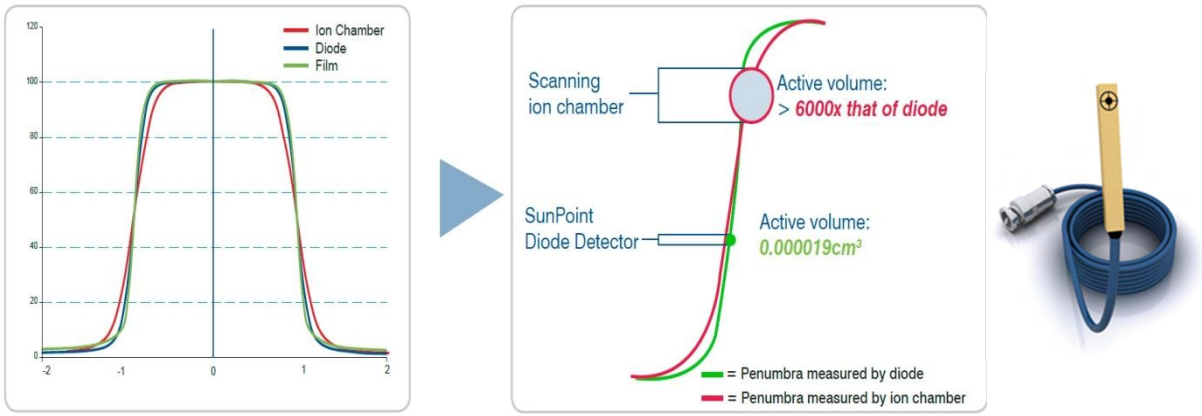

Figure 15. 2 x 2 cm^2 profiles measured with the Sun-point diode and an ion chamber. The excellent precision and less volume averaging affect associated with small diode is able to measure the field edges more accurately [32]

2.6.2 – MLC defined Long and Narrow Irregular Fields:

Another sensitive test of the model is its ability to accurately calculate the dose to small MLC defied fields particularly when the fields are long and narrow with scalloped edges. Fields with a fixed length of 15 cm and widths of 5, 10, 12, 15, 20, 25 and 30 mm were created. All rectangular fields were collimated using the MLC with the long side of the rectangle parallel to the gantry axis of rotation. To achieve this, the collimator was rotated to 0º, 30º, 45º, 60º, 75º, 83º and 90 degrees as shown in figure 16. Pinnacle calculations were repeated for each width and collimator rotation. The jaws were set to 15 x15 cm^2 in order to reduce their influence on the measured output factors. The

detector was positioned at the beam isocenter (100 cm source to axis distance) at a depth of 5 cm in water.

The output factors were calculated relative to a 10 x 10 cm^2 jaws open field using the Pinnacle machines defined in table 3.1, and then compared to measured output factors and those calculated using Varian Eclipse AAA treatment planning software. Measurements were performed using a water phantom and the Sun-point diode detector for an accurate precision. Results will be discussed in section 3.7.2.

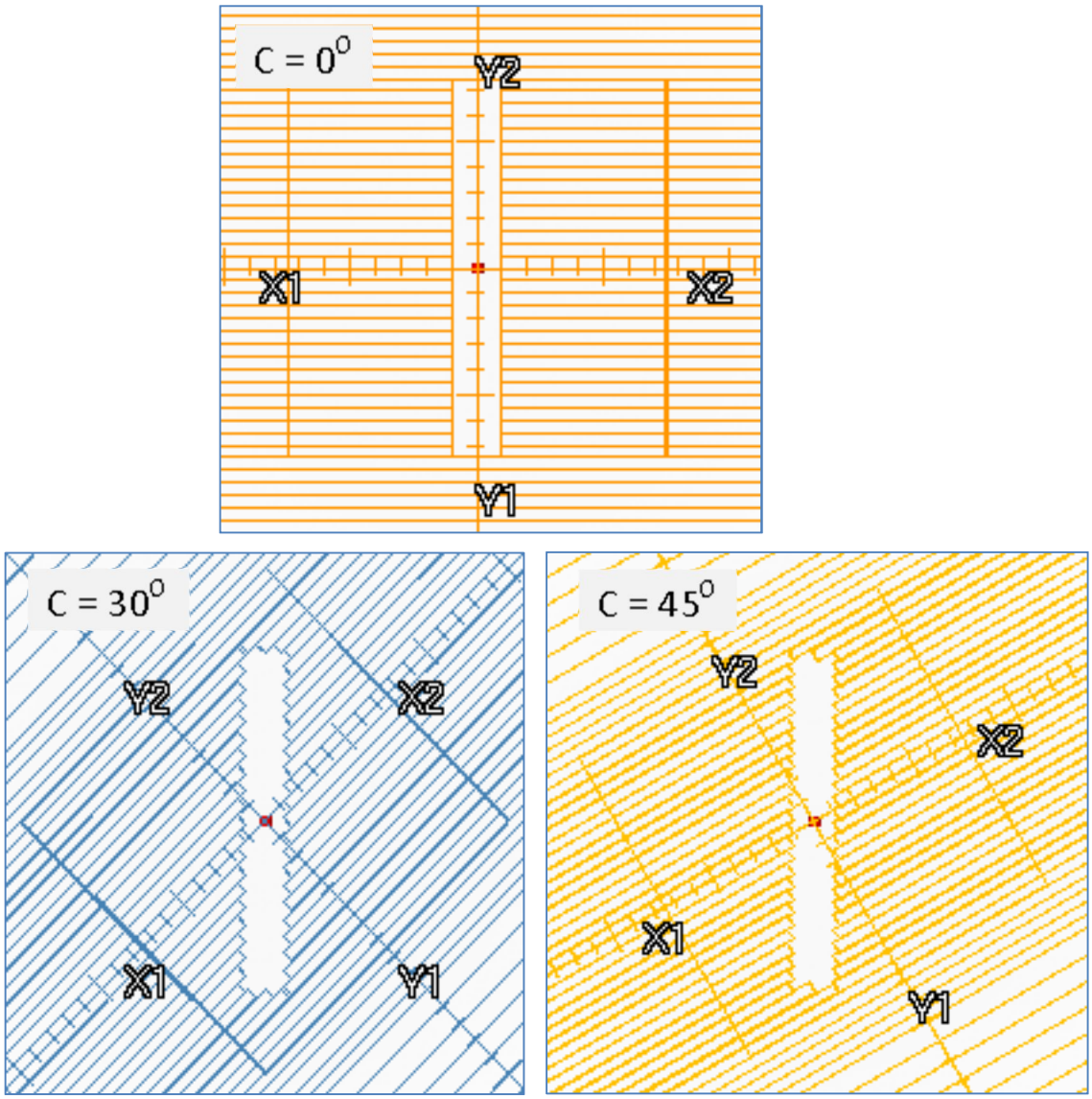

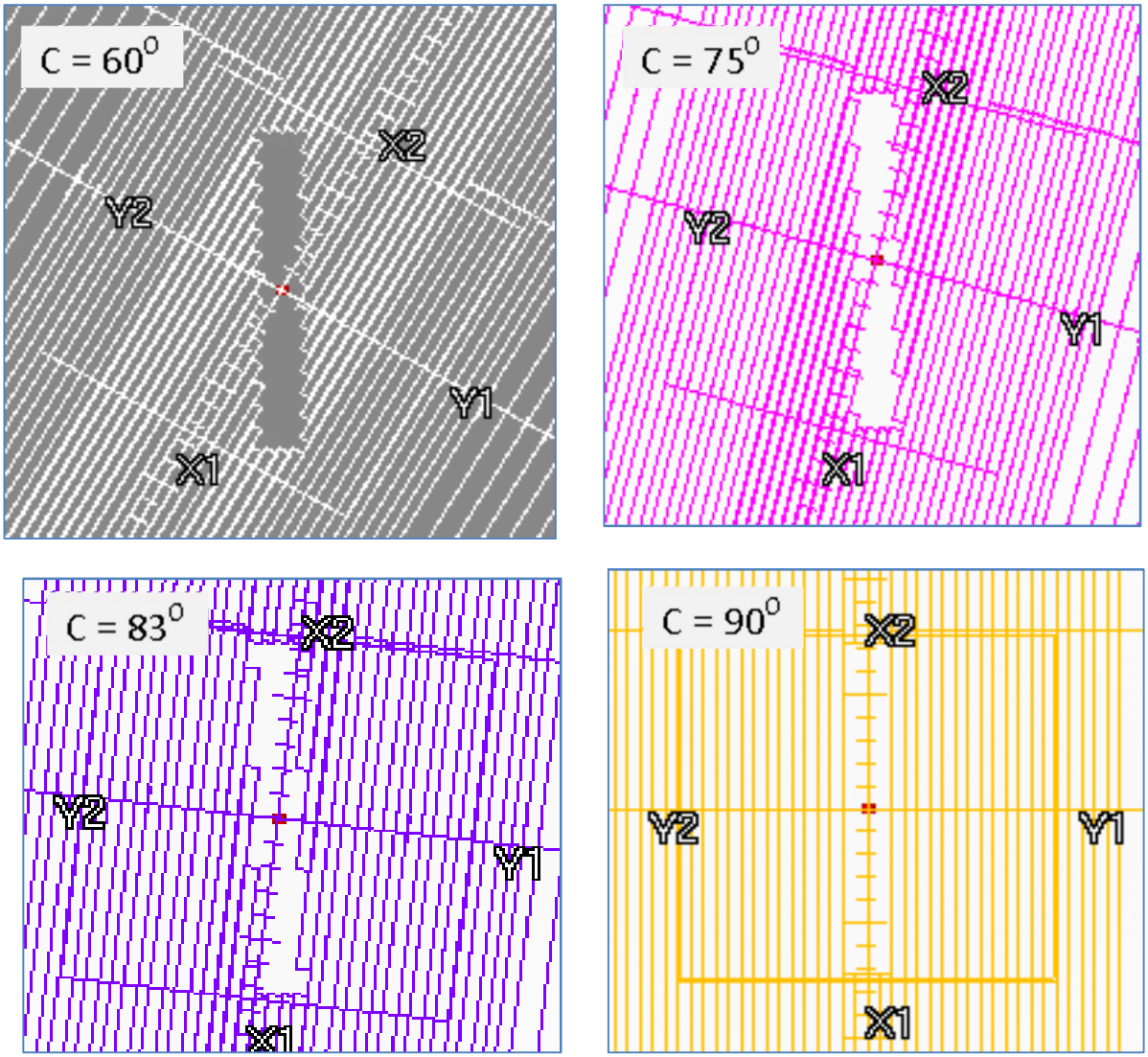

Figure 16. Demonstration of the setup at different collimator rotation for field width of 20 mm [27]

CHAPTER 3: RESULTS AND ANALSIS

3.1 - TERMA and KERMA Calculation vs. PDD Measurement:

TERMA (which represents the total energy released at the point of interaction per unit mass) was calculated using the process described in section 2.3.1 for the 21ex-JCC and BEAMnrc spectrum. Graph 11 shows the plot of the calculated TERMA at central axis as function of depth in water for both energy fluence spectra against the 1 x 1 cm^2 field size percentage depth dose measurement. However, for the purpose of comparison, the curves were normalized at a depth of 5 cm.

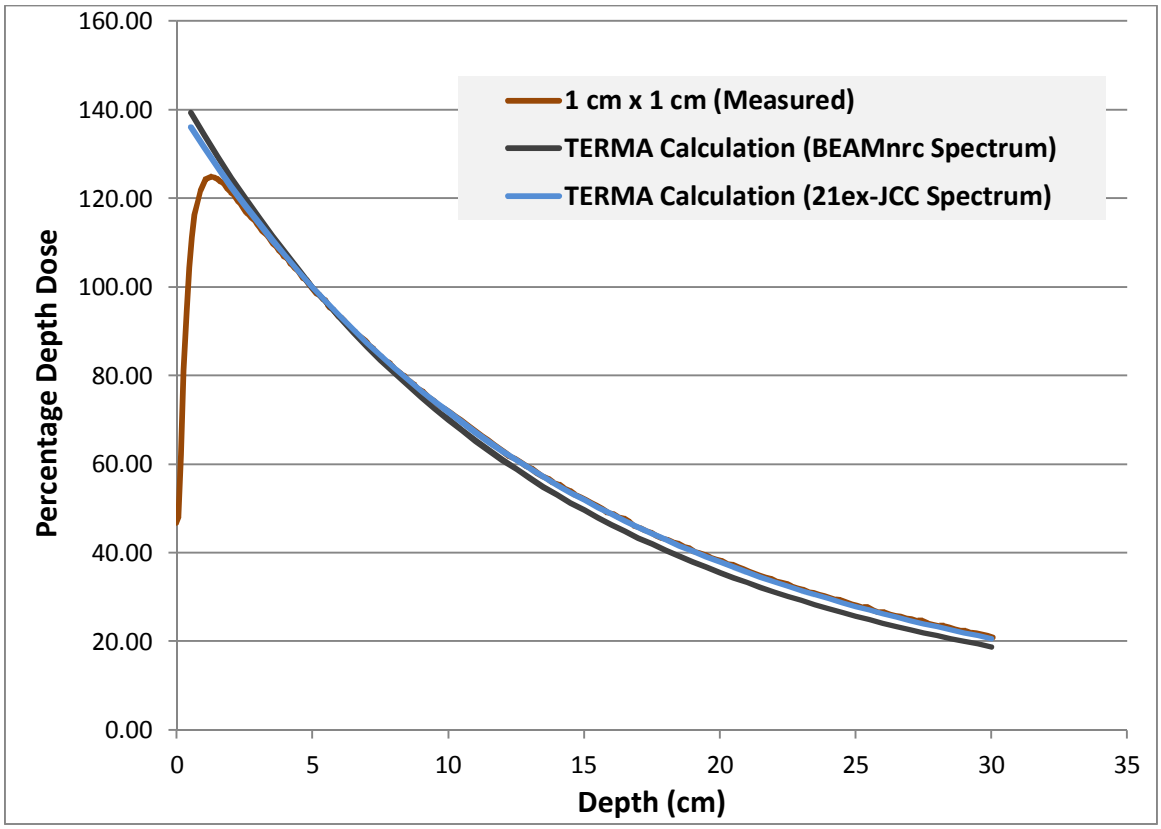

Graph 11. Demonstration plot of TERMA calculation at central axis as function of depth in water for the 21ex-JCC and BEAMnrc energy spectrum against the 1 x 1 cm^2 field size measured depth dose. Note that the whole curves normalized to depth of 5 cm

A 1 x 1 cm^2 field size was used to minimize the contribution of lateral scatter to the central axis percentage depth dose. However, it must be noted that the energy released at the interaction location may not be fully absorbed at that location since energy would be deposited along the path of the secondary charged particles set in motion by primary photons and from the scattered photons from Compton interaction at the primary site of interaction. Therefore, TERMA includes dose from photons that should deposit energy far from the interaction site. As a result, the dose would not be determined accurately without the convolution of TERMA with EDKs. Yet, the graph shows that the 21ex-JCC clinical spectrum was very close to the measured depth dose data in comparison with the BEAMnrc spectrum. This indicates that the 21ex-JCC spectrum was already a harder spectrum. Nevertheless, convolving the calculated TERMA with EDKs would likely result in 21ex-JCC spectrum depth dose being over estimated.

In order to evaluate the BEAMnrc spectrum, KERMA, which represents the kinetic energy of charged particles liberated by uncharged ionizing particles (photons) released per unit mass, was calculated. However, KERMA has two parts: Collision KERMA (K_{Col}) representing the production of electrons that dissipate their energy through ionization and excitation due to the interaction between the charged particles and the atomic electrons. Radiative KERMA (K_{rad}) representing the production of radiative photons due to the interaction between the charged particles and the atomic nuclei resulting in bremsstrahlung x-ray, or from annihilation in flight (E.B. Podgorsak, 2005)[33]. Therefore, since part of the energy will be lost in the form of bremsstrahlung escaping from the volume of interest, collision KERMA may be related to absorbed dose.

The collision KERMA calculation involves the same process described in section 2.3.1 except for equation number 2, which is replaced by:

$$K_{col}(d) = \sum_{E} \Psi(E,d)\, x\, \frac{\mu_{en}(E)}{\rho} \qquad (4)$$

where $\mu_{en}(E)/\rho$ represents the mass-energy absorption coefficient in water as a function of the photon energy bin (NIST)[29].

Graph 12 shows the plot of the calculated collision KERMA as function of depth in water for BEAMnrc energy fluence spectrum compared to the 1 x 1 cm^2 field size percentage depth dose measurement.

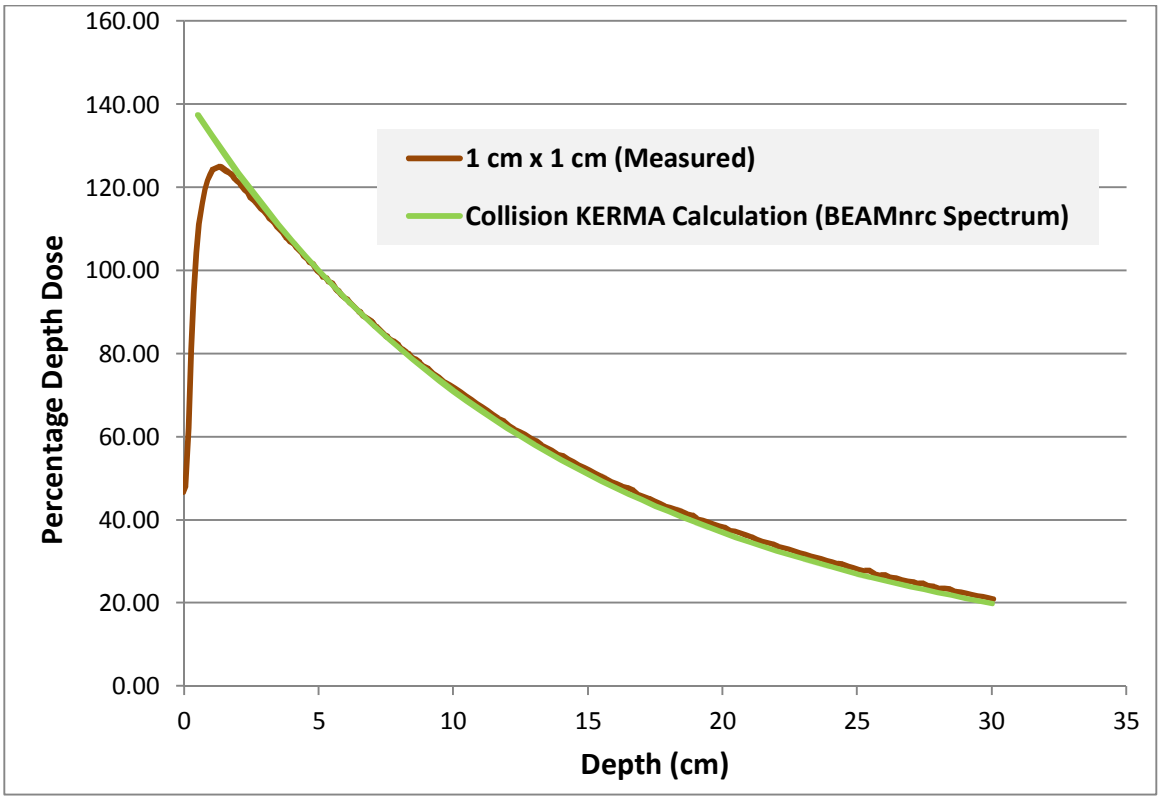

Graph 12. Plot of collision KERMA calculated along the central axis as function of depth in water for BEAMnrc energy spectrum and the 1 x 1 cm^2 field size measured depth dose. Note that the both curves normalized to depth of 5 cm

The graph shows that the difference between the calculated TERMA and collision KERMA against the 1 x 1 cm^2 measured percentage depth dose was minimal for the BEAMnrc spectrum. However, it has to be understood that KERMA can be approximated as the absorbed dose for low energy. While for high energy, fast secondary emission electrons would deposit some of their energy outside the region of interest, whereas, absorbed dose is the energy per unit mass absorbed along the path of the charged particles (E.B. Podgorsak, 2005)[33]. Consequently, the difference between the calculated Collision KERMA using the BEAMnrc spectrum and the measurement is understandable.

3.2 - The Implications of Adopting the BEAMnrc Spectrum on Depth Dose Calculation:

In section 2.3.2, the BEAMnrc spectrum was attenuated by different depths of water to determine a depth equivalent spectrum where the ideal spectrum applied to Pinnacle should correspond. Consequently, the BEAMnrc spectrum that is attenuated to a depth of 15 cm of water gives the closest agreement between the computed and measured depth dose. This attenuated spectrum will be referred to as BEAMnrc (A15). Graph 13 compares the 21ex-JCC, BEAMnrc, and the most important spectra based on our study.

A manual calculation of the mean energy shows that the 21ex-JCC has a mean energy of 2.117 MeV at central axis, while the BEAMnrc and BEAMnrc (A15) have 1.773 MeV and 2.111 MeV respectively. Graph 13 shows that the BEAMnrc (A15) spectrum

shape differs from that of the 21ex-JCC spectrum. However, the calculation shows that they both have nearly the same average energy at central axis.

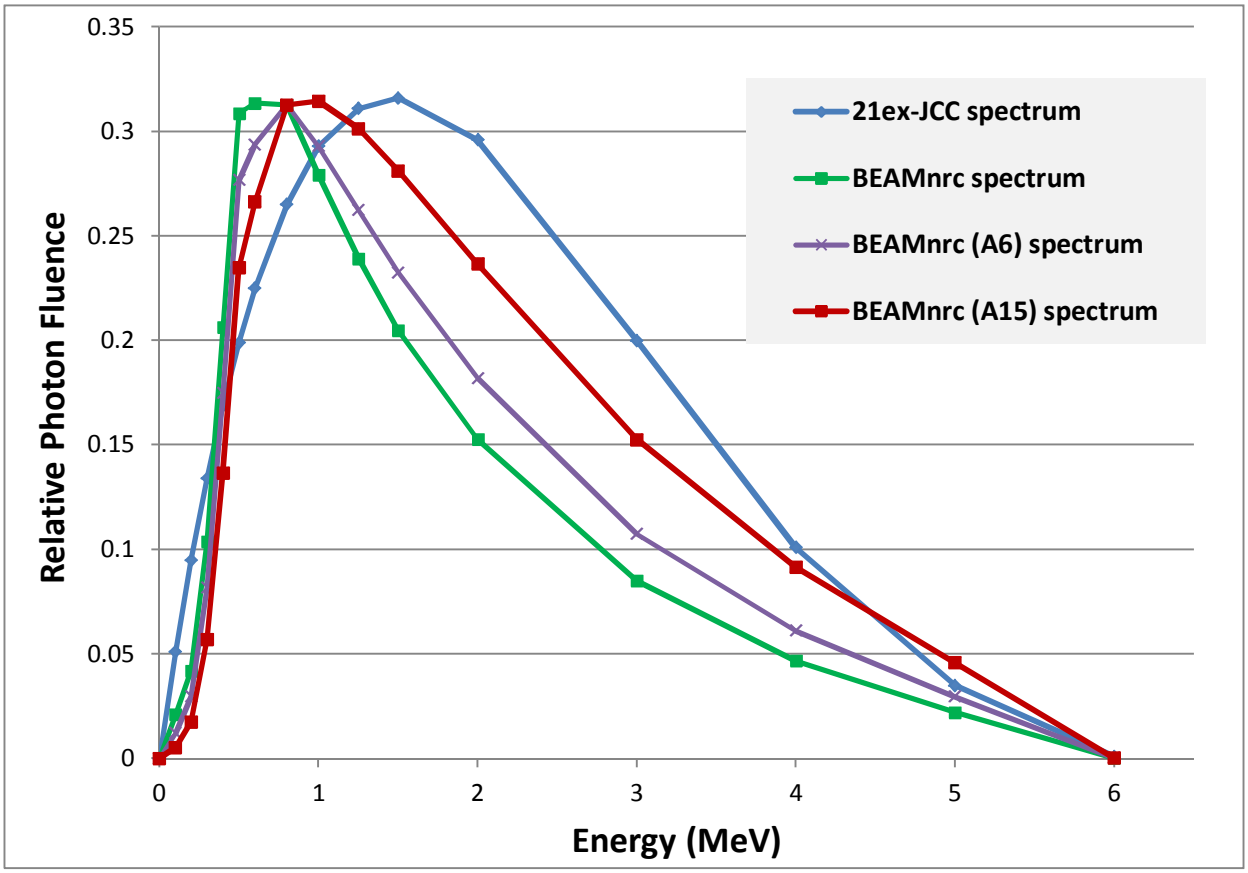

Graph 13. A comparison between the 21ex-JCC, BEAMnrc, BEAMnrc (A6) and BEAMnrc (A15) all normalized to 21ex-JCC spectrum. BEAMnrc (A6) represents the BEAMnrc spectrum attenuated by 6 cm depth of water; BEAMnrc (A15) represents the BEAMnrc spectrum attenuated by 15 cm depth of water

Although the BEAMnrc (A15) spectrum is a slight softer than the 21ex-JCC spectrum, it yields excellent results when tested in Pinnacle beam-modeling calculations of depth dose against measurements for field sizes ranging from 3 x 3 cm^2 to 40 x 40 cm^2 fields. Graph 14 shows an example of 3 x 3, 10 x 10 and 20 x 20 cm^2 percentage depth dose calculation compared to measurements.

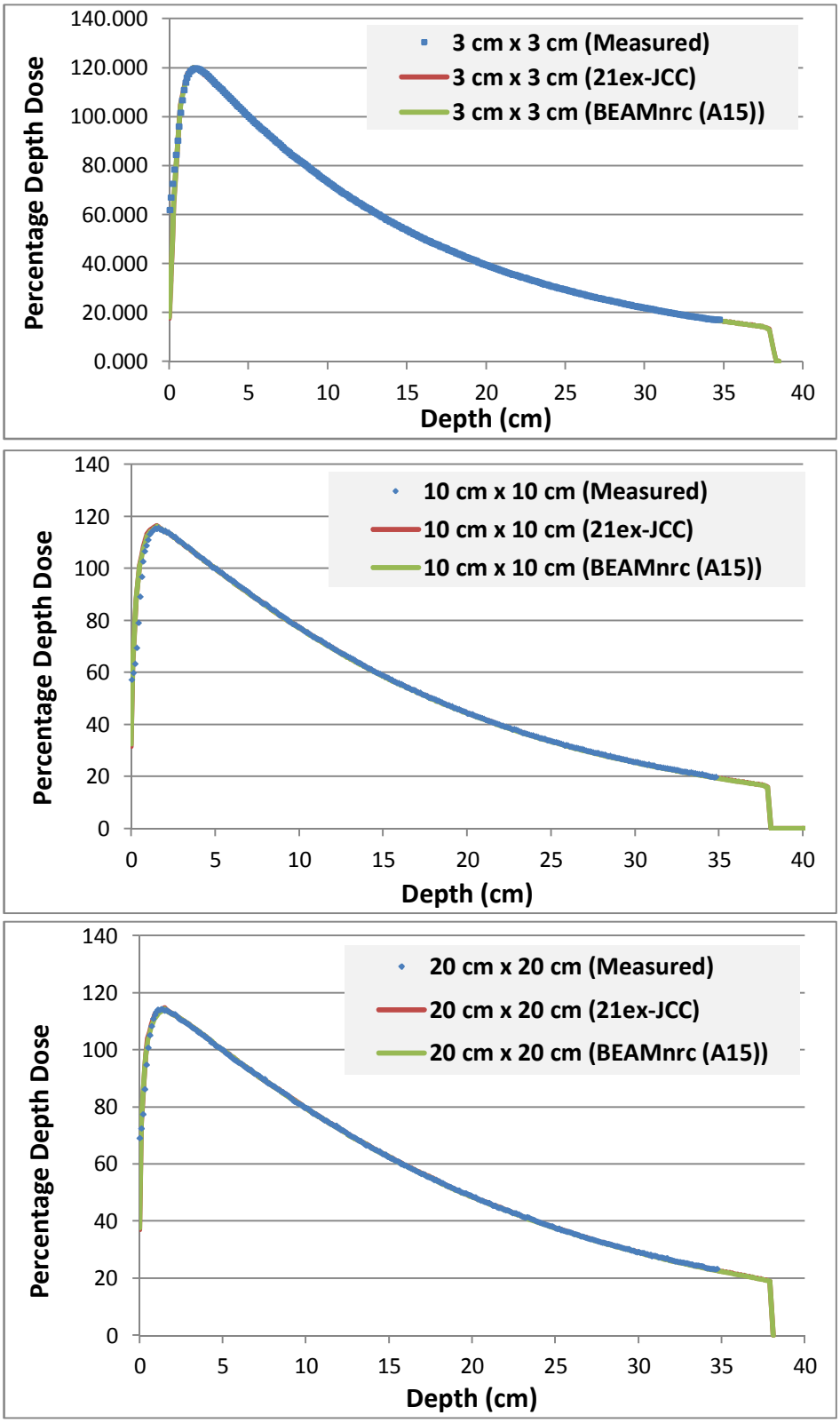

Graph 14. A comparison of depth doses normalized to 5 cm depth for different field sizes calculated using either the 21ex-JCC (red line) or the BEAMnrc (A15) (green line) spectra. The measured curve is also plotted (blue dots)

Note that for a 1 x 1 cm^2 field, both the 21ex-JCC and BEAMnrc (A15) spectrum fail to model it accurately since they both overestimate the depth dose. However, when we used the BEAMnrc spectrum that is attenuated to a depth of 6 cm of water shown in graph 13, the Pinnacle calculation matches the measured depth dose curve as shown in graph 15. At larger field sizes, that spectrum resulted in an underestimation of the depth doses.

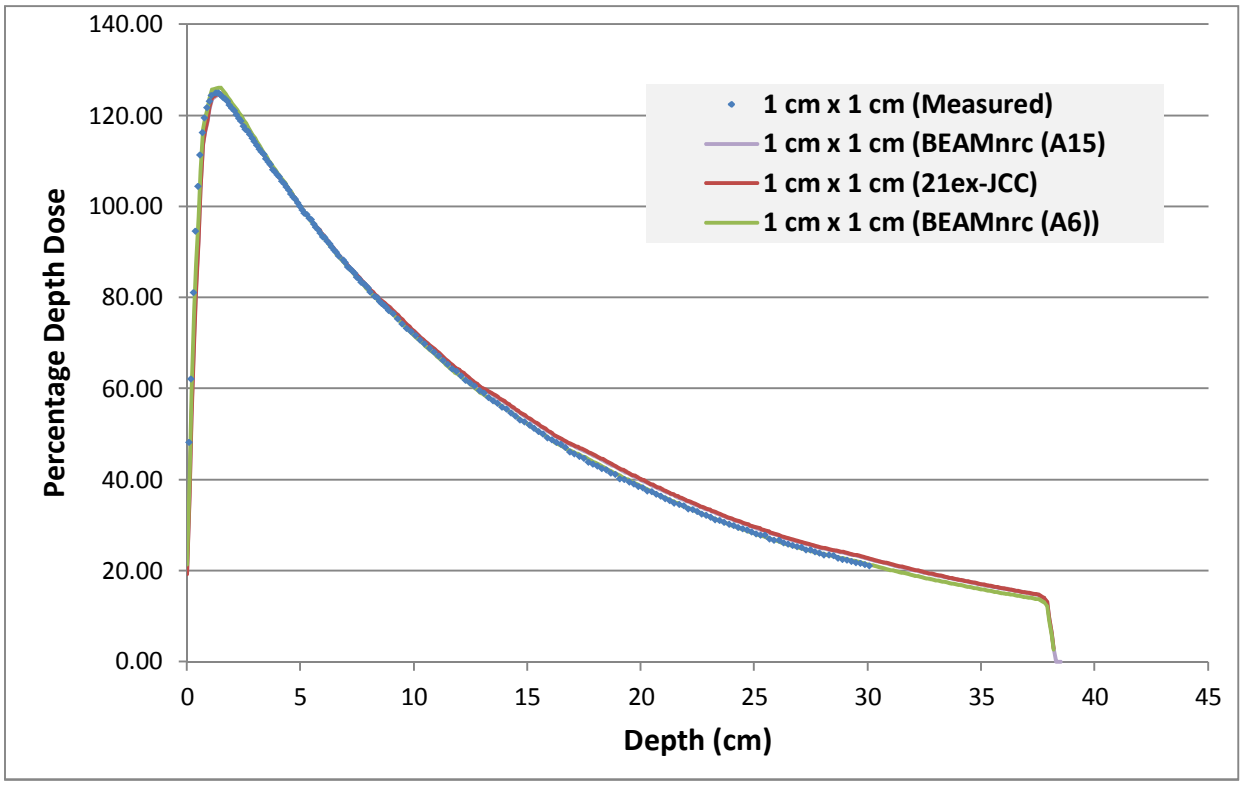

Graph 15. A comparison of 1 x 1 cm^2 field size depth dose normalized to 5 cm depth calculated using either the 21ex-JCC (red line), the BEAMnrc (A15) (purple line) or the BEAMnrc (A6) (green line) spectra. Note that the 21ex-JCC depth dose is overlapping the BEAMnrc (A15). The measured curve is also plotted (blue dots)

3.3 - The Implications of Adopting the BEAMnrc Spectrum on Dose Profile Calculation:

As discussed in section 2.1.1, Pinnacle uses a radial fluence profile to account for the changes of the relative number of incident photons as a function of radial distance, while the changes in the distribution of photon energies as a function of radial distance is managed by the use of Spectral Off-Axis Softening Factor parameter. Pinnacle uses this factor to account for the beam hardening and softening effect by changing the mean energy as function of distance from central axis as illustrated in graph 16.

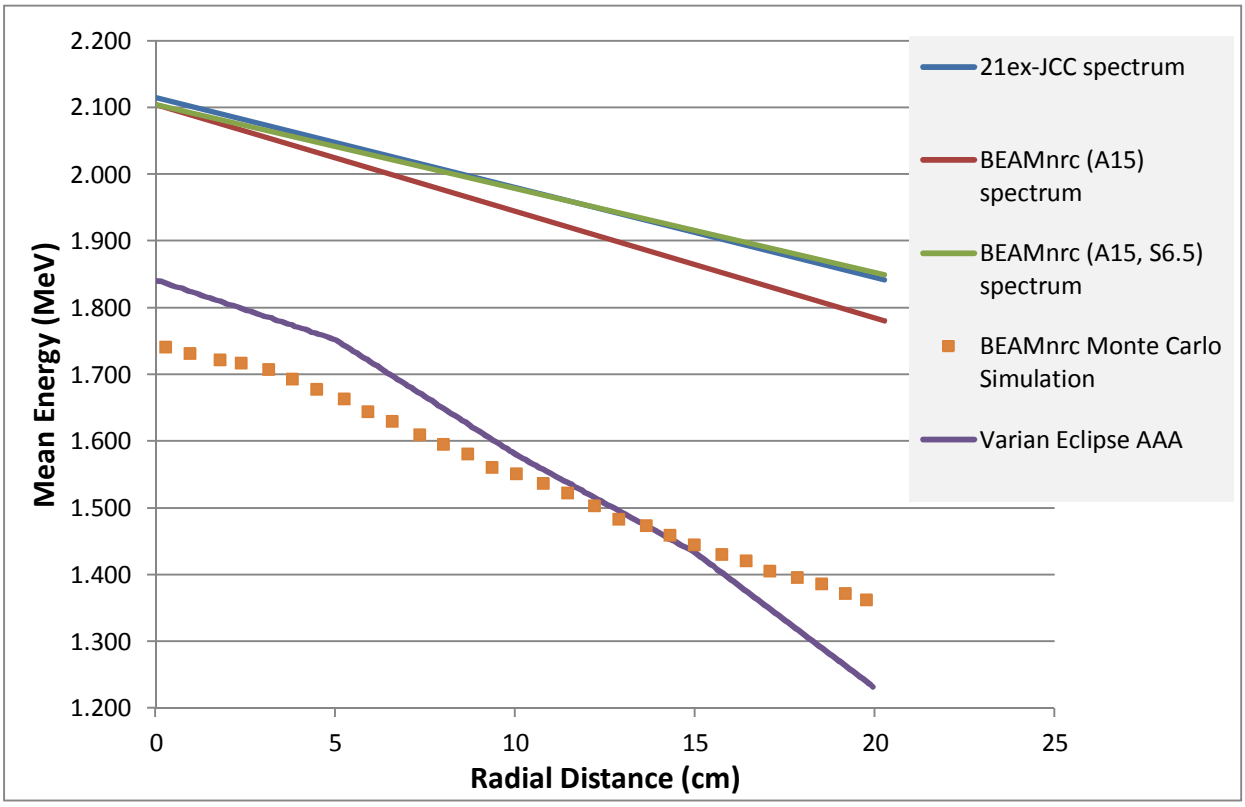

Graph 16. Demonstration of Pinnacle modeling of mean energy as function of distance from central axis for Varian 6 MV photon beam calculated using the 21ex-JCC (blue line), BEAMnrc (A15) (red line) and BEAMnrc (A15, S6.5) (green line) spectrum where Off-Axis Softening was adjusted to 6.5, against Varian Eclipse AAA algorithm (purple line)[34] and BEAMnrc Monte Carlo Simulation for 6 MV Varian Linac (orange square dots)[10]

It can be seen from graph 16 that the mean energy of the photon beam is decreasing with increasing distance from central axis due to flattening filter beam hardening and softening effect. The BEAMnrc (A15) spectrum (red line) resulted in an average energy of 2.105 MeV at central axis calculated by Pinnacle beam modeling in comparison with 2.115 MeV for the 21ex-JCC spectrum (blue line) when both spectra use the same Off-Axis Softening Factor parameter. This is in good agreement with the manual calculation of the mean energy from section 3.2.

The BEAMnrc (A15) mean energy falls more quickly with off-axis distance from the center in comparison with the 21ex-JCC spectrum. Our investigation shows that this has an effect for the calculated dose profiles for fields larger than 10 x 10 cm^2, while it has no effect for smaller fields. Graph 17 shows an example of computed x-axis dose profile for 10 x 10, 20 x 20 and 30 x 30 cm^2 fields at depth of 5 cm using the 21ex-JCC and BEAMnrc (A15) spectrum against the measurement. The graph illustrates that for a 10 x 10 cm^2 field, both spectra yielded approximately an identical dose profile. Yet, 20 x 20 and 30 x 30 cm^2 field shows some differences at the shoulder due to larger horns computed by the BEAMnrc (A15) spectrum.

Conversely, at depths beyond 15 cm of water, the mean energy as a function of distance difference between the BEAMnrc (A15) and the 21ex-JCC spectrum had almost no effect for larger field size dose profiles. Graph 18 shows an example of 30 x 30 cm^2 field x-axis dose profile at depth of 20 cm for the 21ex-JCC and BEAMnrc (A15) spectrum compared to measurement. The graph illustrates that both spectra yielded approximately the same dose profiles.

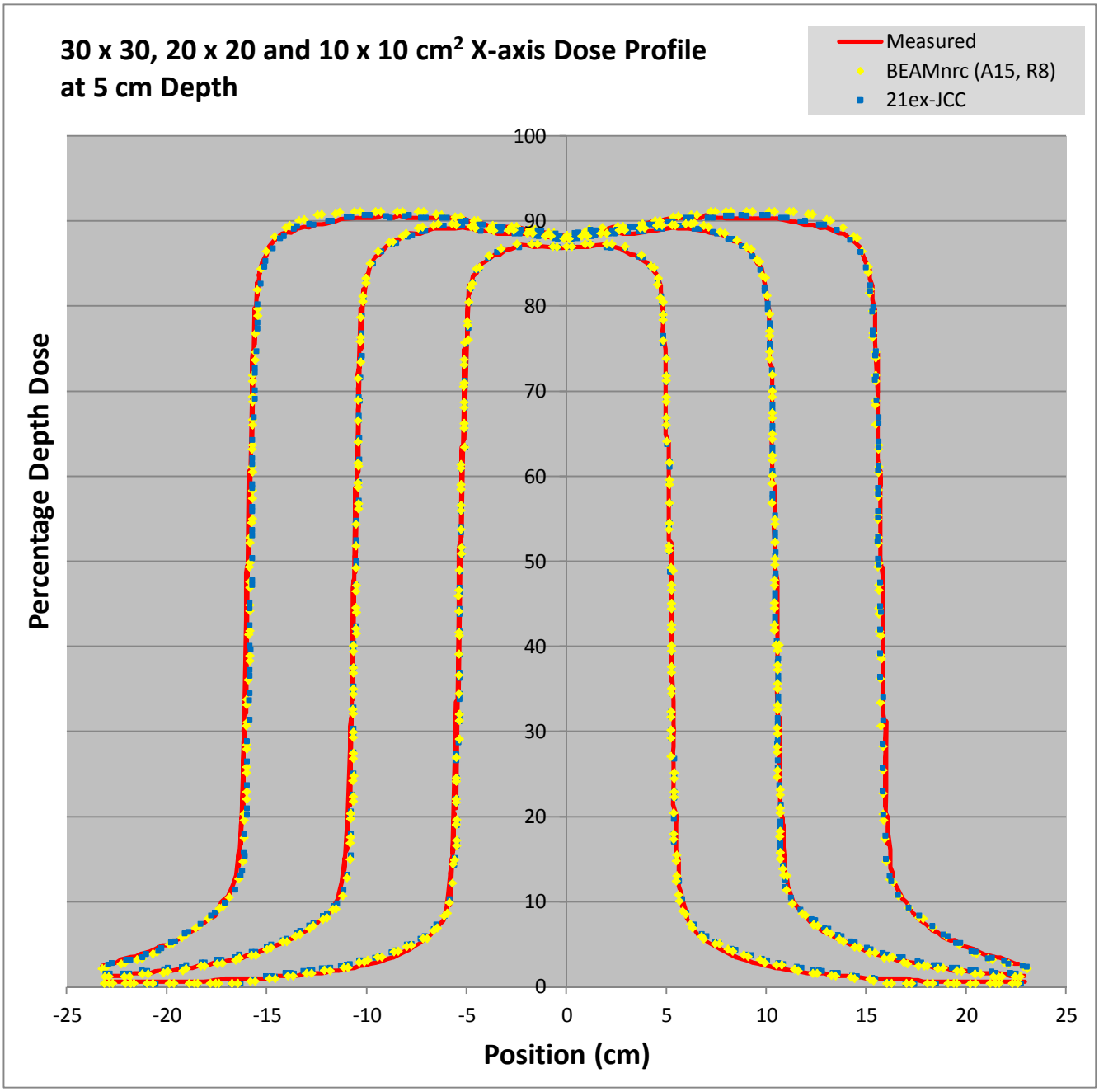

Graph 17. A comparison of x-axis dose profile calculated using either the 21ex-JCC (blue dots) or the BEAMnrc (A15) (yellow dots) spectra against the measurement (red line) for 10 x10 (inner), 20 x 20 (middle) and 30 x 30 (outer) cm^2 fields at depth of 5 cm. The graph shows that both spectra yielded approximately the same dose profile for the 10 x 10 cm^2 field, while differences at the shoulder where the horns become more pronounced for the dose profile computed by the BEAMnrc (A15) spectrum for larger field size dose profile

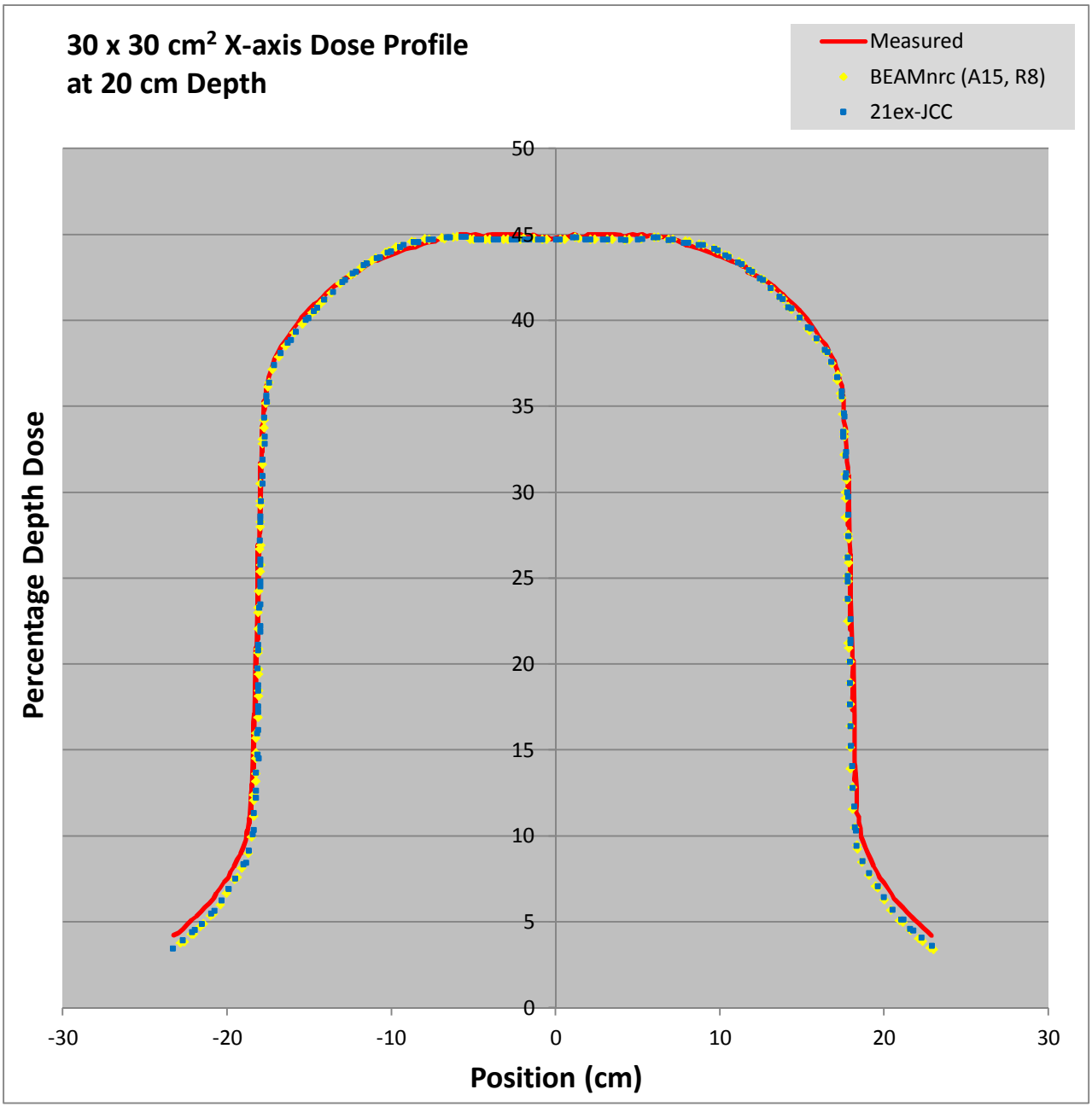

Graph 18. A comparison of x-axis dose profile calculated using either the 21ex-JCC (blue dots) or the BEAMnrc (A15) (yellow dots) spectra against the measurement (red line) for 30 x 30 cm^2 fields at depth of 20 cm. The graph shows that both spectra yielded almost identical dose profiles. The differences in mean energy as function of distance between the 21ex-JCC and BEAMnrc (A15) has no effect for larger field sizes on dose profiles at deeper depths (beyond 15 cm)

In order to account for these discrepancies between the BEAMnrc (A15) and the measurement for larger field sizes at shallow depth, the Off-Axis Softening Factor parameter was changed from 8.45312 to 6.5, while the radial fluence was kept the same. This resulted in the Pinnacle calculation of the mean energy as function of distance as shown in graph 16 for BEAMnrc (A15, S6.5) (green line), where S stands for Softening factor.

As a result, the BEAMnrc (A15, S6.5) has the same mean energy at central axis as the BEAMnrc (A15). However, the mean energy as function of distance does not fall at the same rate. It starts slightly lower than the mean energy calculated by the 21ex-JCC spectrum at central axis, and goes slightly higher at off-axis distance as shown in graph 16. Accordingly, this resulted in a good agreement between the computed and measured dose profiles for larger field sizes at shallow depths. An example is shown in graph 19, for 30 x 30 cm^2 field at depth of 5 cm. Thus, the dose profile calculated using the 21ex-JCC and the BEAMnrc (A15, S6.5) spectrum yielded an almost identical dose profiles.

Furthermore, it can be seen that the mean energy as function of distance calculated by Pinnacle is decreasing linearly in comparison with mean energy simulated using Monte Carlo BEAMnrc simulation for 6 MV Varian linac as illustrated in graph 16. The simulation shows about 1.74 MeV at the central axis, which then falls gradually before going steeply [10]. On the other hand, Varian Eclipse AAA[34] algorithm has a 1.84 MeV mean energy at central axis as shown in graph 16. This mean energy falls more gradually in comparison with the Monte Carlo BEAMnrc simulation.

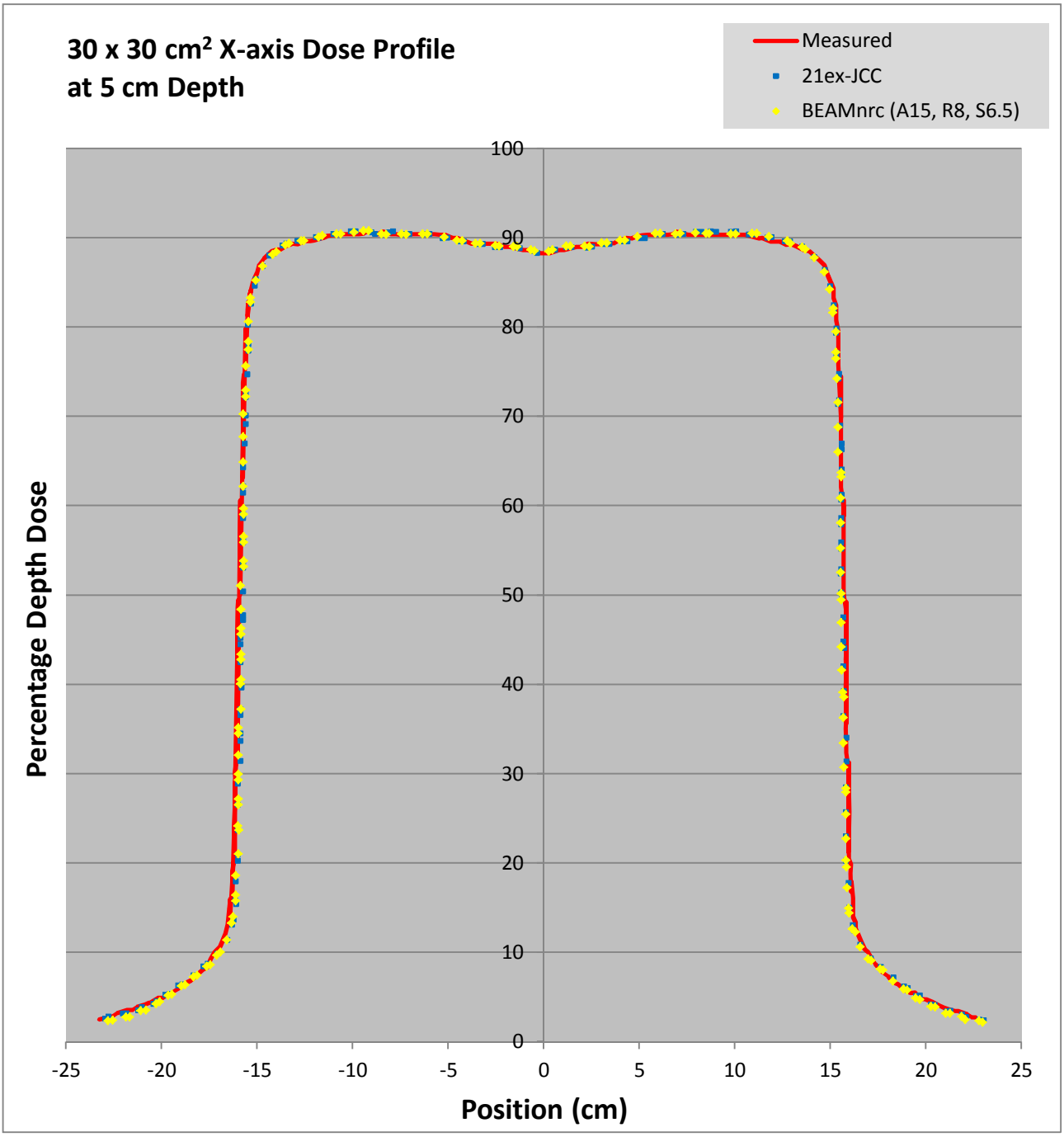

Graph 19. A comparison of x-axis dose profile calculated using either the 21ex-JCC (blue dots) or the BEAMnrc (A15, S6.5) (yellow dots) spectra against the measurement (red line) for 30 x 30 cm^2 fields at depth of 5 cm. The graph shows that both spectrums yielded an almost identical dose profile when Off-Axis Softening Factor parameter was changed from 8.45312 to 6.5

3.4 - The Implications of Adopting the BEAMnrc Spectrum on Pinnacle Output Factor Dependence with Field Size:

In section 2.1.3, we discussed the output factor modulation in Pinnacle beam modeling. It was shown in graph 5, that pinnacle uses the modeling configuration to calculate the output factor (OFp), however, since the model does not account for the whole effect of the head scatter, Pinnacle applies a field-size dependent correction factor (OFc) in order for the computation to match the measurement.

In this section, the effect of applying the BEAMnrc spectrum on the output factor modulation in Pinnacle beam modeling was investigated. For that purpose, the beam modeling parameters were kept the same as the 21ex-JCC except for the spectrum. Graph 20 shows the OFp and OFc computed using the 21ex-JCC, BEAMnrc and BEAMnrc (A15) spectrum.

The Pinnacle manual guide states that in the modeling process, the user should try to achieve uniformity of the OFc among the various field sizes (OFc =1) so that OFp would match the measured relative output factor. Accordingly, graph 20 shows that when we used a softer spectrum such as the BEAMnrc, the calculated OFc (green dots) were much closer to uniformity and the OFp (green line) is closer to the measurement (red line). This indicates that, as we use a softer spectrum, Pinnacle OFp difference with the measurement is reduced. However, the BEAMnrc spectrum was not good in calculation of the PDD and dose profiles since the calculations were always lower than the measurement.

The BEAMnrc (A15) spectrum yielded slightly better calculations of OFc and OFp than the 21ex-JCC spectrum.

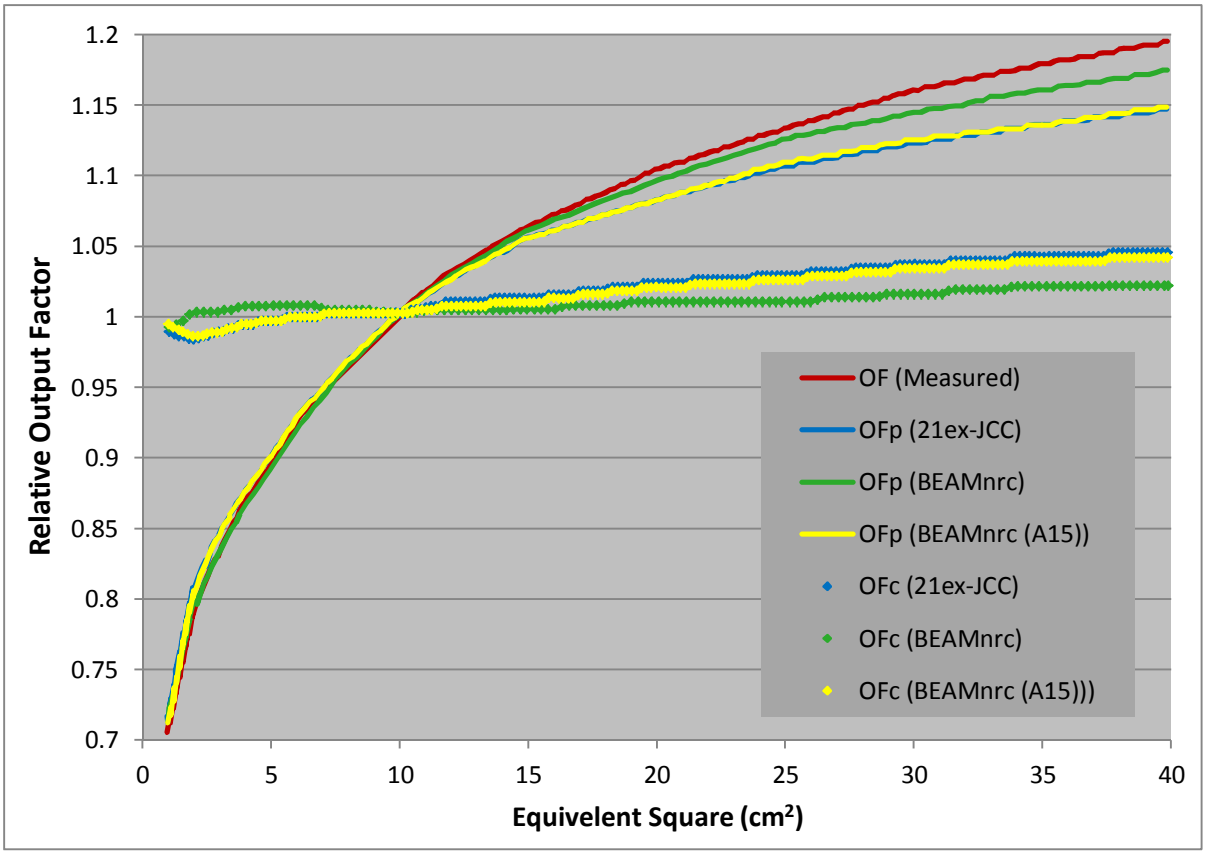

Graph 20. Demonstration of Pinnacle beam modeling of OFp (output factor modeled by Pinnacle) and OFc (field-size dependent correction factor applied by Pinnacle to correct for OFp); using either the 21ex-JCC (blue), BEAMnrc (green) or BEAMnrc (A15) (yellow) spectrum

3.5 - The Implications of Adjusting the Leaf Tip Radius and MLC Offset Table on MLC Defined Fields for Dose Profile Calculation:

In this section, we assess the calculation of dose profiles for fields defined by MLC similar to our investigation in section 3.3. This is to elucidate the MLC model in

Pinnacle. The machine parameters were kept the same as the 21ex-JCC except for the energy spectrum in order to validate the BEAMnrc (A15) model.

The 21ex-JCC and BEAMnrc (A15) models lead to nearly the same result in the calculation of dose profiles especially at high dose gradient regions near the shoulders. However, at low dose gradient regions near the tails of the dose profile, the beam models show slight differences. Since BEAMnrc (A15) has a softer spectrum, that leads to a slightly wider penumbra near the tails of the dose profile. Besides that, both the 21ex-JCC and BEAMnrc (A15) spectra underestimate the shoulders and the penumbra of the dose profile for fields defined by the MLC. Due to that, several adjustments have been implemented to account for those discrepancies.

The Pinnacle manual reports that penumbra widens with smaller leaf tip radius, while increasing the leaf tip radius sharpens the penumbra (Pinnacle^3 Physics Reference Guide)[6]. The 21ex-JCC model uses a 6.5 cm leaf tip radius of curvature for the modeling of the MLC while retaining the original Varian MLC calibration offset table. Boyer and Li, 1997[(5)] reported a dependence of the leaf offset on leaf tip radius of curvature. Since Varian Millennium MLC has a leaf tip radius of 8 cm, we decided to use the radius that corresponds to the Varian MLC calibration offset table. As a result, increasing the leaf tip radius from 6.5 cm to 8 cm sharpens the penumbra for the BEAMnrc (A15) spectrum. This results in an overall slightly better agreement especially in the low dose gradient regions near the tails of the dose profile as illustrated in graph 21. Yet, the BEAMnrc (A15, R8) model still underestimates the penumbra and the shoulders of the dose profile for the fields defined by the MLC. Consequently, the Varian

MLC offset table implemented in the Pinnacle beam model was adjusted to further improve the calculation of the MLC defined fields for dose profile calculation.

Different adjustments were examined as discussed in section 2.4; however, we found that subtracting a fixed value of 0.045 cm from the whole leaf tip calibration offset table leads to the best computation of dose profiles that were better than the clinical machine. For example, a 4 x 4 cm^2 MLC defined field would became:

At X-axis: (2.045 cm + 2.045 cm for right and lift MLC banks) = 4.09 cm

At Y-axis: (2 cm + 2 cm) = 4 cm

The final field size would be = 4.09 x 4 cm^2 MLC defined field. This is because, MLC moves only in the x-axis plane, while the Y-axis field size is determined by the geometrical thickness of the leaf. This means that the MLC defined field would be larger by 0.9 mm in x-axis plane for any fields calculated with our new BEAMnrc (A15, R8, O - 0.045) machine. An example for (2 x 2, 4 x 4 and 6 x 6 cm^2 MLC – 10 x 10 cm^2 jaws) defined fields at depth of 5 cm are shown in graph 22.

It can be seen that this adjustment leads to better agreement at the high dose gradient regions near the shoulders of the dose profile including the penumbra, while it is slightly widens the calculation at the low dose gradient regions near the tails of the dose profile. This could be improved by increasing the leaf tip radius to 9 cm. Moreover, this adjustment is more suitable for smaller MLC defined fields as it becomes less efficient as we increases the field size to a larger field as shown in graph 22.

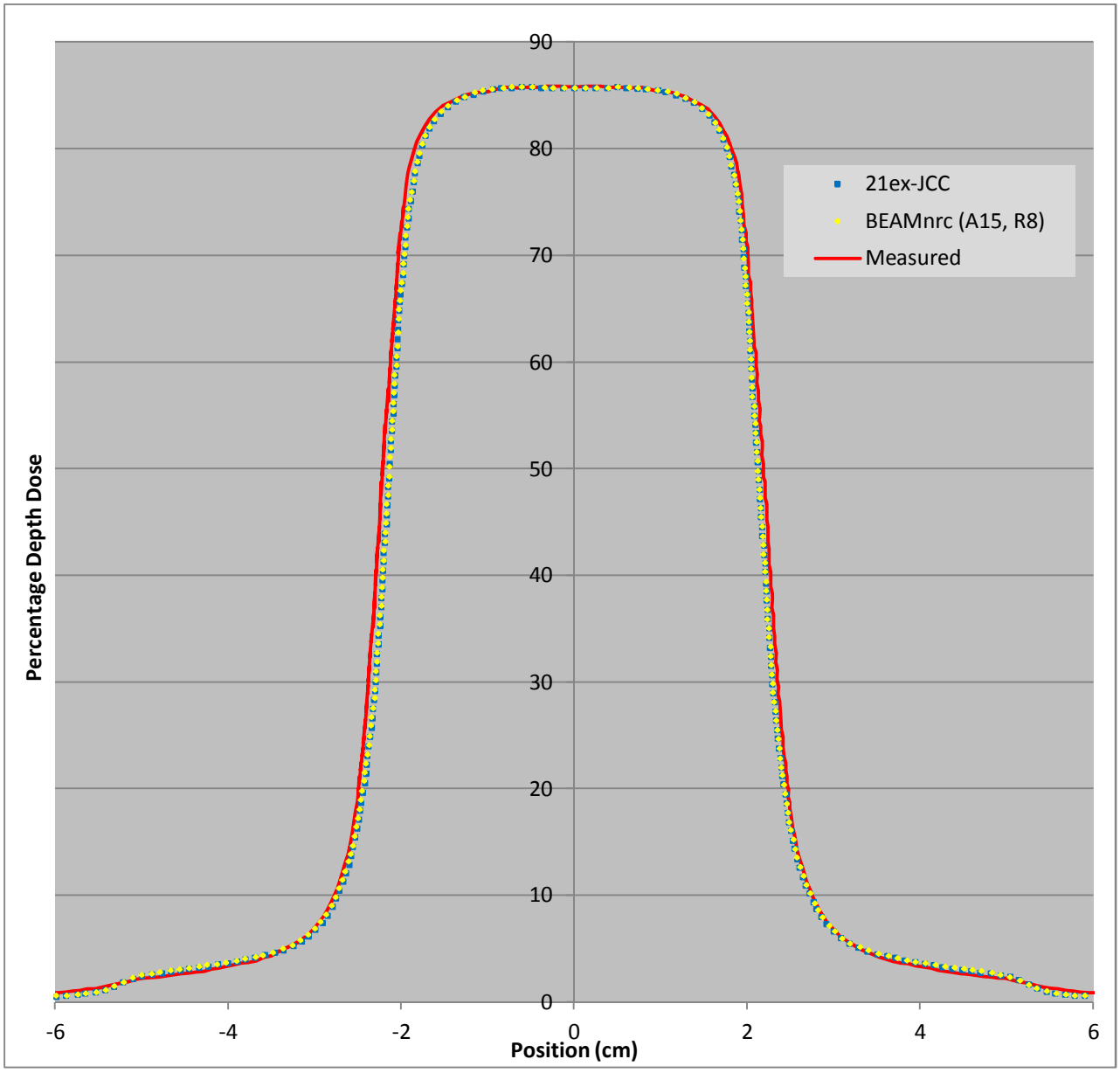

Graph 21. A comparison of (10 x 10 cm^2 Jaws – 4 x 4 cm^2 MLC) defined X-axis dose profile calculated using the 21ex-JCC (blue dots) and BEAMnrc (A15, R8) (yellow dots) spectrum in comparison with the measurement (red line). However, using 8 cm leaf tip radius sharpens the penumbra of the BEAMnrc (A15) and leads to better agreement in the low dose gradient regions near the tails of the dose profile

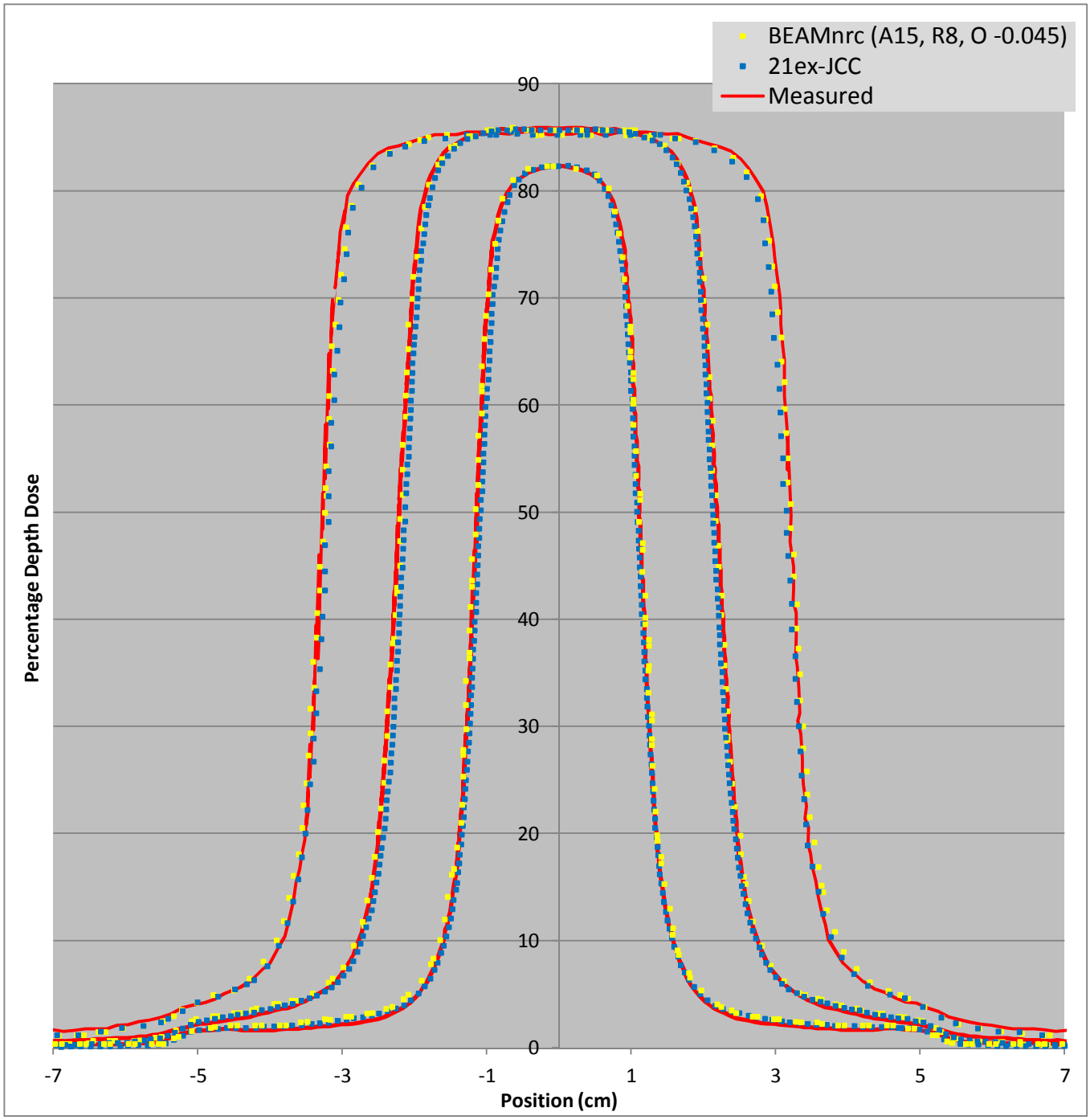

Graph 22. A comparison of x-axis dose profile for fields defined by 10 x 10 cm^2 Jaws and 2 x 2 (inner), 4 x 4 (middle) and 6 x 6 (outer) cm^2 MLC defined fields at depth of 5 cm. calculated using either the 21ex-JCC (blue dots) or the BEAMnrc (A15, R8, O -0.045) (yellow dots) spectra against the measurement (red line). Adjusting the MLC calibration offset table leads to better agreement in the high dose gradient regions near the shoulders of the dose profile and penumbra. However, the profile is a slight wider in the low dose gradient regions near the tails

3.6 - Effect of Machine Parameters on MLC Abutment Leakage:

As discussed in section 2.5, abutment fields were calculated using different machines to assess the Pinnacle beam modeling. The planar dose images were analyzed using ImageJ and plotted for comparison. A demonstration of Left, Central and Right abutment field profiles will be investigated for the examined machines.

From graph 23, it can be concluded that using different energy fluence spectra results in different leakage patterns. For example, using the same leaf tip radius (6.5 cm) for calculating these abutment profiles results in BEAMnrc (R6.5) (olive green line) having slightly higher leakage in comparison with abutment profiles calculated using either BEAMnrc (A15, R6.5) (blue line) or the 21ex-JCC (red line) which have a harder spectrum respectively. Moreover, it can be seen that for those previous machines, the transmission leakage increases with increasing distance from central axis. However, changing the leaf tip radius to a nominal value (8 cm) that corresponds to the Varian Millennium MLC resulted in a more realistic profile. This is shown in the calculation of the left and right field abutment profiles using the BEAMnrc (A15, R8) model (purple line) where profile falls near the edges of the fields. Nevertheless, changing the off-axis softening factor to 6.5 has almost no effect in the calculation of the abutment profiles. This is demonstrated in the calculation with BEAMnrc (A15, R8, S6.5) (orange line) since it overlaps with BEAMnrc (A15, R8) (purple line). Furthermore, Williams and Metcalfe, 2005[(34)] recommended the use of a leaf tip radius of 12 cm to improve dosimetric calculation agreement with measurement. However, the calculation of the abutment profiles using BEAMnrc (A15, R12) (green line) machine resulted in a profile with irregular leakage with increasing distance from central axis as can be seen in

graph 23. Moreover, the whole calculated profile has less transmission leakage observed for peaks and valleys in comparison with the previous machines with the exception at the far edges of the fields that shows an increase in calculated leakage dose.

Furthermore, graph 24, shows that increasing the leaf tip radius from 8 to 9 cm would result in a decrease of the peaks and valleys for the whole calculated abutment profile. Consequently, transmission leakage falls more with increasing distance as demonstrated for the right field abutment profiles.

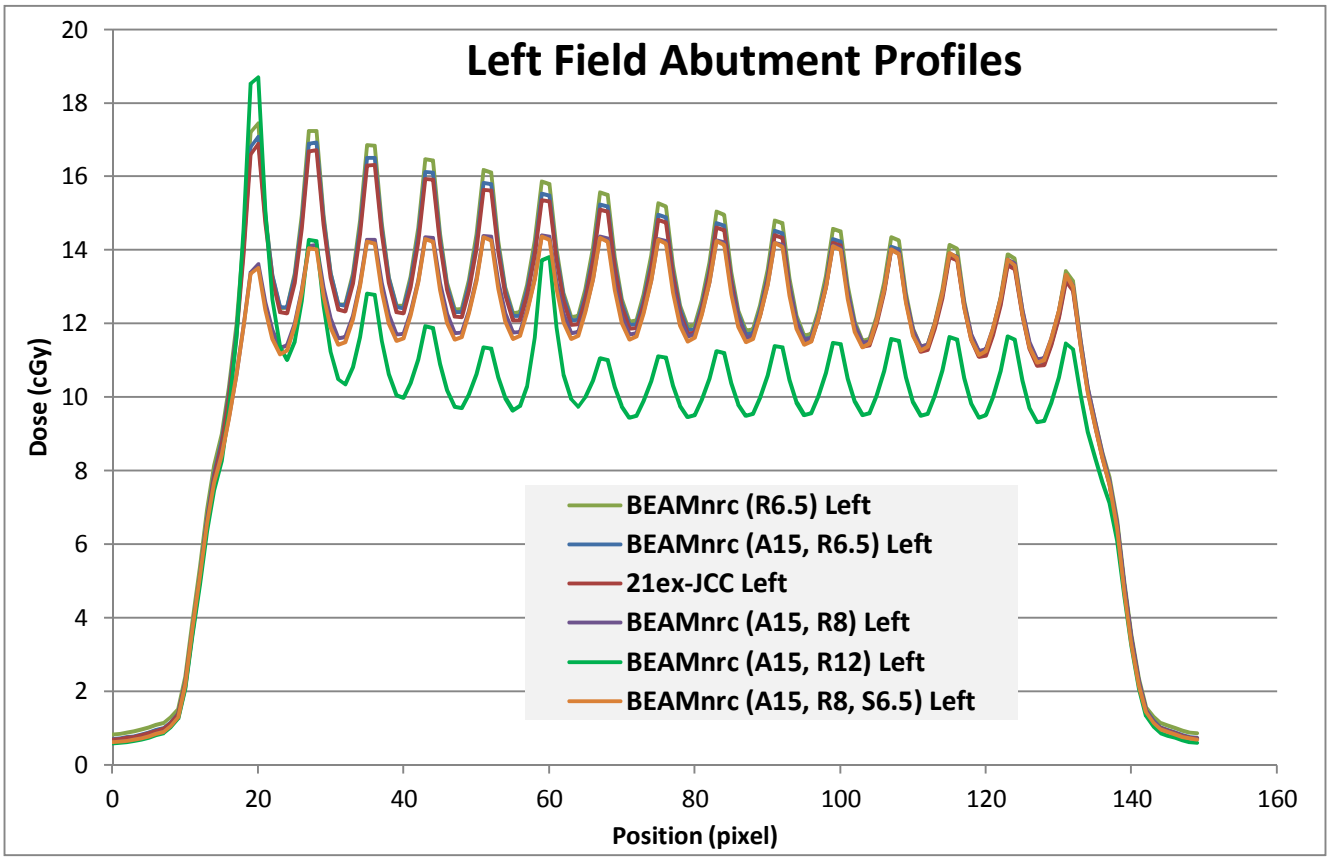

Graph 23. Demonstration of left field abutment profiles calculation. Note that 1 cm equal to 8 pixel based on the resolution of the RAW images exported from Pinnacle

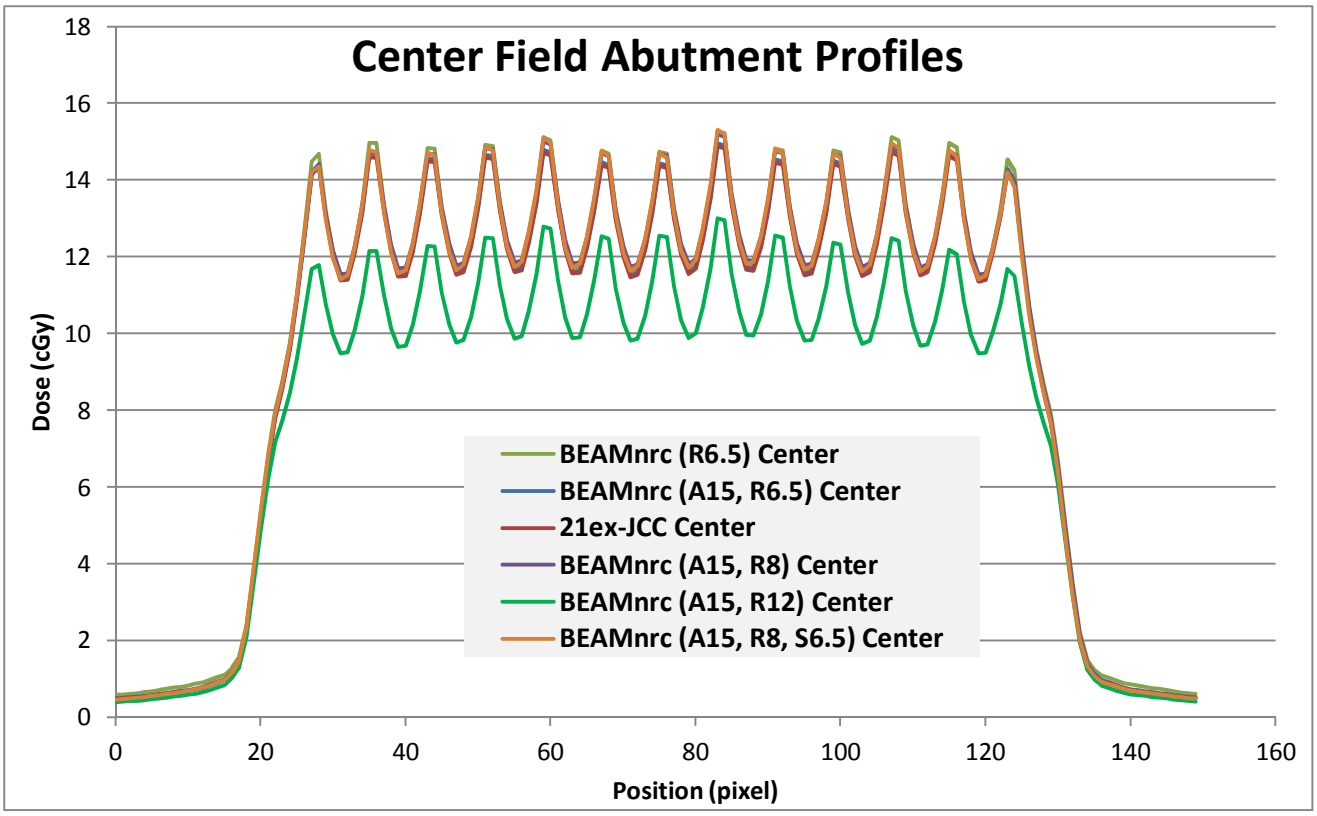

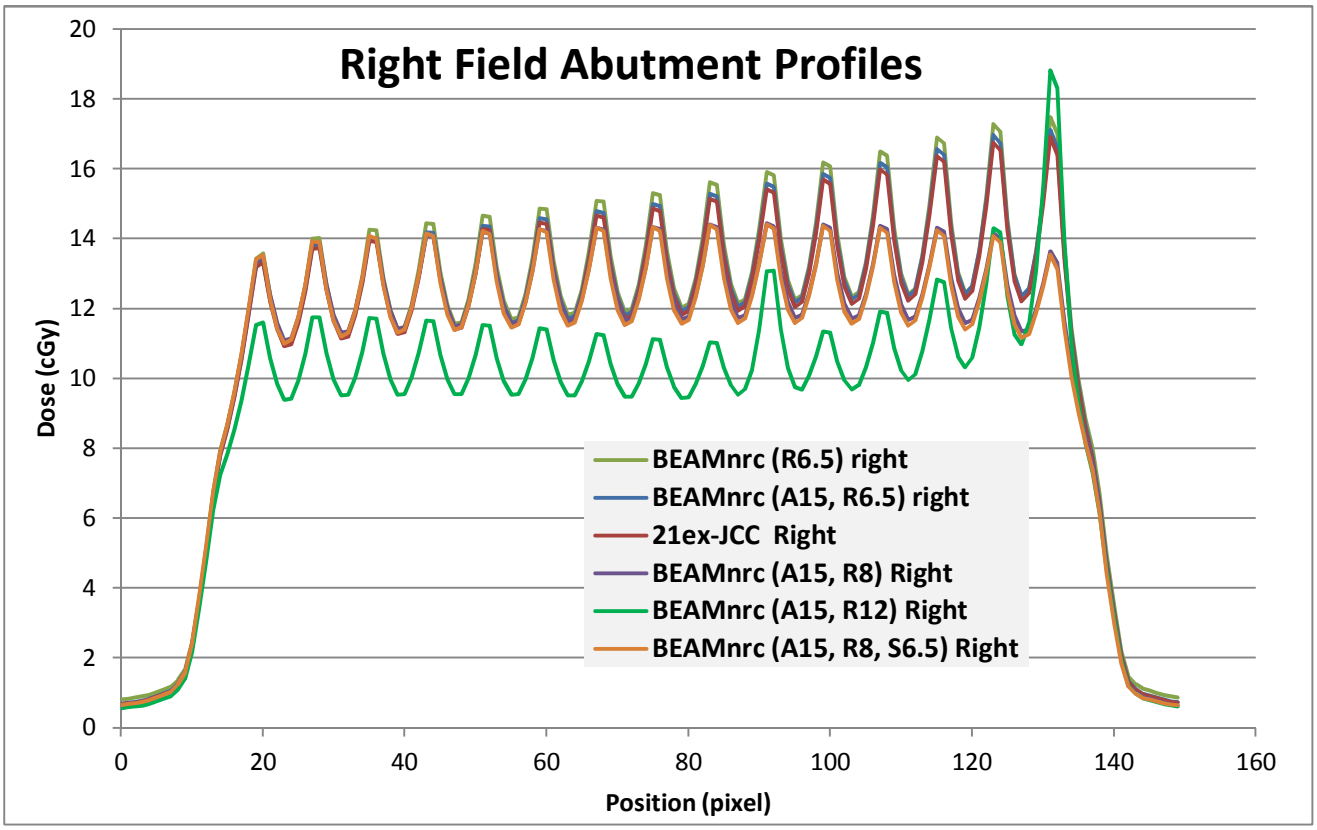

Graph 23. Demonstration of left, center and right fields abutment leakage profiles calculated and examined using different machines. Note that 1 cm equal to 8 pixel based on the resolution of the RAW images exported from Pinnacle

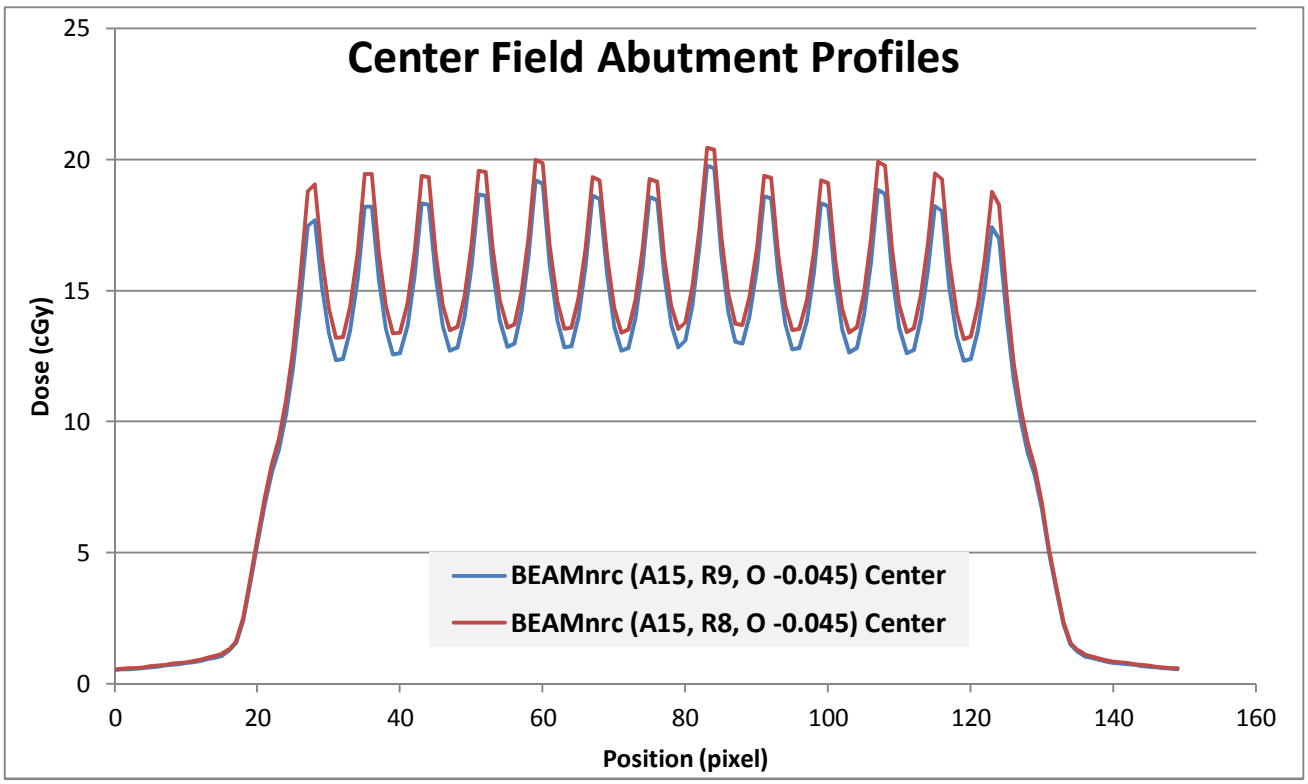

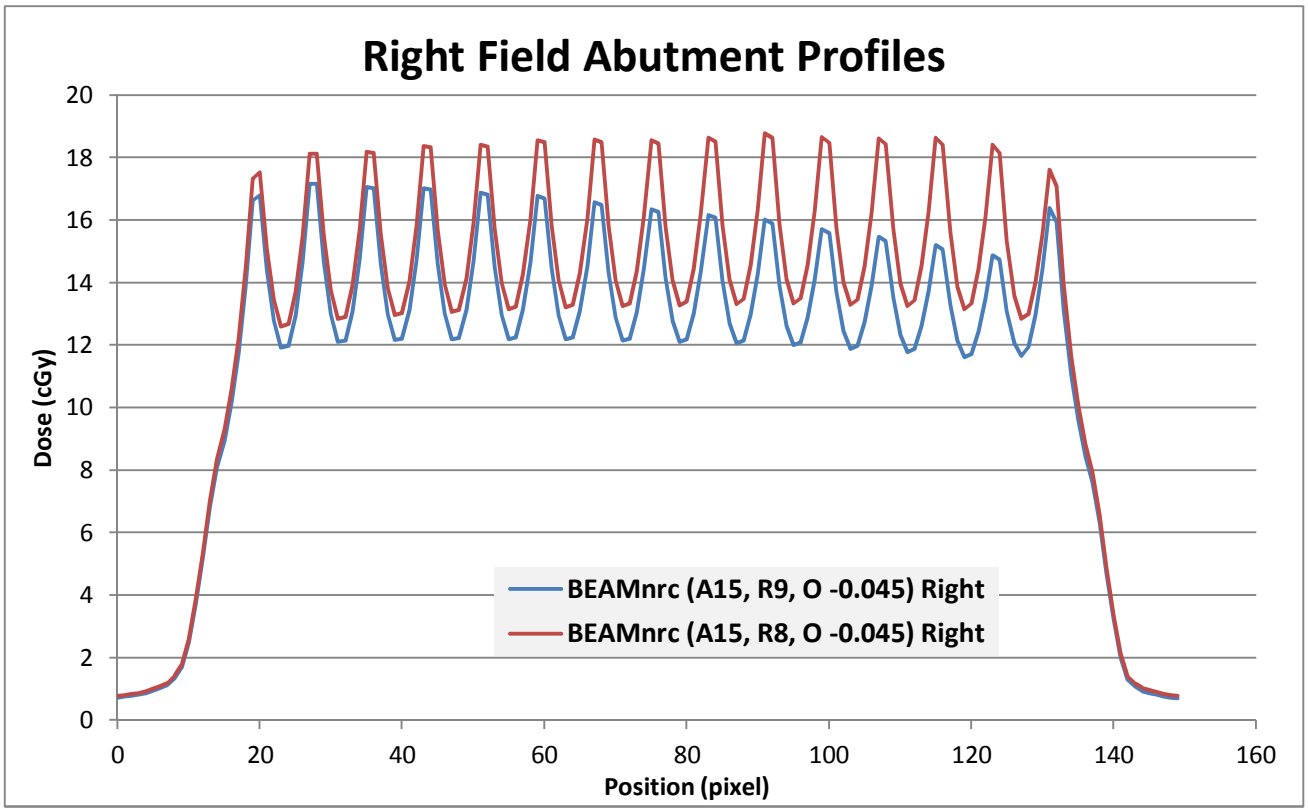

Graph 24. Demonstration of center and right fields abutments leakage profiles calculated for machine with different leaf tip radius. It can be seen that increasing the leaf tip would reduce the leakage. Note that 1 cm equal to 8 pixel based on the resolution of the RAW images exported from Pinnacle

3.6.1 – Calculation vs. Measurements:

Plotting the 21ex-JCC (red line) and BEAMnrc (A15, R8) (purple line) calculated profiles against the film measurement (blue line) shows an unexpected result as demonstrated in graph 25. The calculated center field abutment profile valleys (corresponding to intra-leaf leakage) shows a close match against the measurement at the side of the field for both machines. While the abutment field profile measurements valleys were slightly higher at the center. Conversely, the measurement has higher peaks (corresponding to leakage dose between opposing leaves) in comparison with both calculated machine profiles. Calculated abutment field profiles were widely discrepant with those measured at the field edge farthest from the central axis for both machines. The measurement has higher peaks closer to central axis, while the profile falls down faster near the far edges of the fields.

After investigation, it was found that the Pinnacle planning software has applied the MLC calibration offset table in the calculation of these planned zero gap abutment. Due to that, a small gap between the opposed leaves would always been set depending on leaf position. Conversely, the machine does not apply the MLC offset table when a zero gap between planned opposing leaves is specified. Thus, due to beam divergence far from central axis, a ray would pass through a greater thickness of the leaf body lowering the transmission leakage.

In order to assess the MLC modulation further, we created a machine with zeroed offset table to force Pinnacle not to apply the MLC offset. with zero planned abutment gap. Graph 25, also shows the abutment field profiles calculation using

BEAMnrc (A15, R8, No Offset) (orange line) machine. The center field calculation was very close to the 21ex-JCC and BEAMnrc (A15, R8) calculated profiles with the exception of the reduced peaks near the edges. The right and left field profiles show some irregular trend. The measured abutment leakage was higher than calculated abutment near the central axis; and significant differences between measured and computation were observed away from the central axis. In addition, variation in calculated profiles does not decrease with off axis distance in a way consistent with measurement. This limitation maybe due to the implementation of the Pinnacle MLC beam model.

Furthermore, graph 25 also shows abutment field profiles calculated for the same plan using Varian Eclipse AAA calculation algorithm (green line). The profiles shows that Eclipse AAA algorithm has also applied the MLC calibration offset table similarly to Pinnacle. However, the calculated profiles were far more discrepant from measurement than Pinnacle calculations. This could be due to the different implementation approach in the modeling of the MLC between the two treatment planning systems.

Since version 7.4, Pinnacle has incorporated a model that accounts for the rounded MLC leaf-ends modulation; it also provides separate parameters for inter-leaf transmission, intra-leaf transmission, and tongue and groove properties as was discussed before. Conversely, Eclipse gives only a single averaged transmission factor as an approximation to account for the MLC inter-leaf and intra-leaf transmission; while the rounded leaf-ends are not modeled explicitly, yet it is approximated by an offset value add to the leaf position controlled by the Dosimetric Leaf Separation (DLS). These parameters are depth and field size dependent. The MLC transmission and DLS are

optimized to gives the best agreement between measurement and calculation (Wasb and Valen, 2008)[36]. However, this could explain the differences in the calculated profiles between the two planning systems. The generated gap applied by the MLC offset table and DLS to the opposing leaves is always smaller in Eclipse in comparison with Pinnacle.

Finally, it has to be noted that the combined uncertainties in the EBT2 film dosimetry measurements and scanning procedure could contribute to a dose error of up to 2.8% (Aland *et al*, 2011)[37]. This is the maximum expected uncertainty in the Y-axis, while there is a fixed uncertainty of 0.5 to 1 mm in the x-axis to account for MLC travel and positioning error (not shown in the graph). This limitation could be the reason for some irregular peaks pattern observed in the measured profiles.

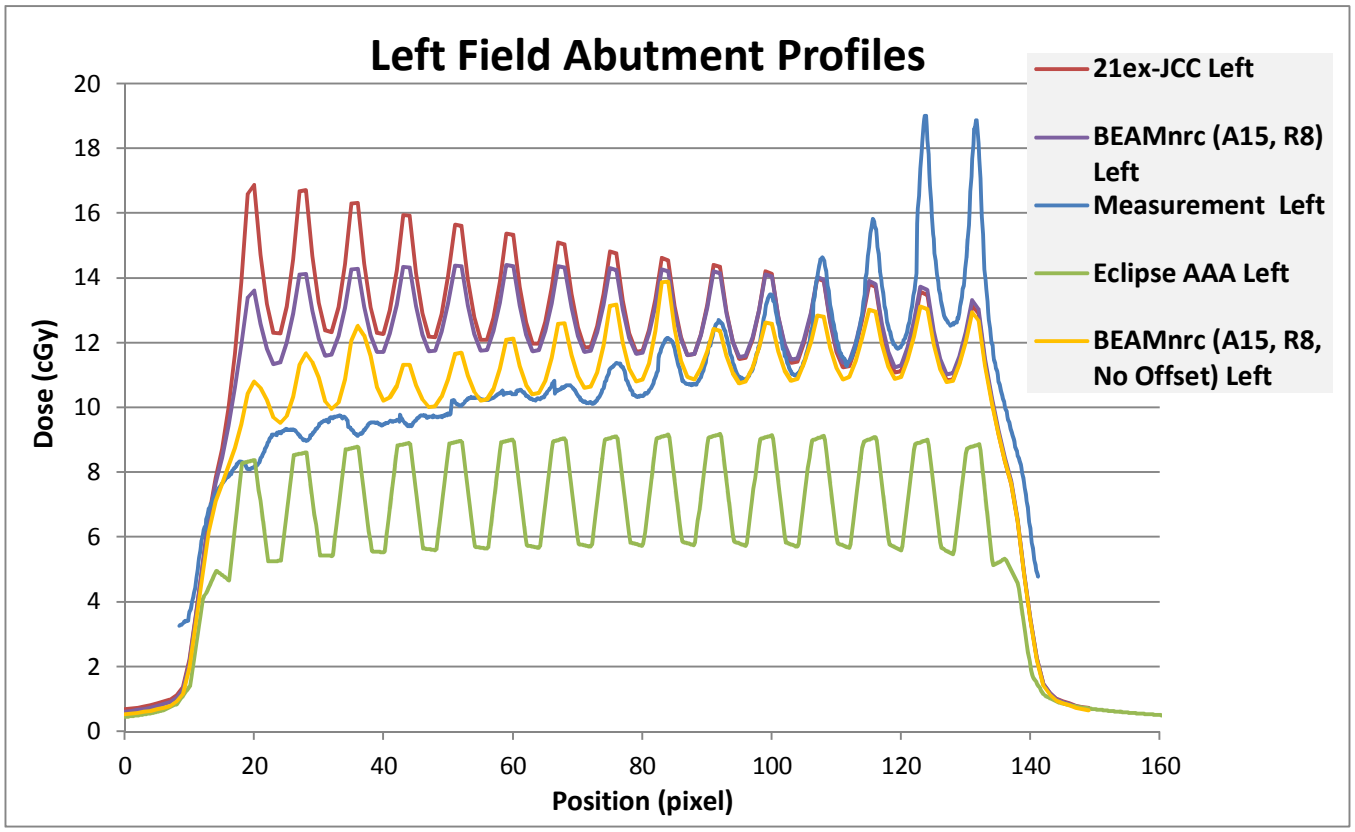

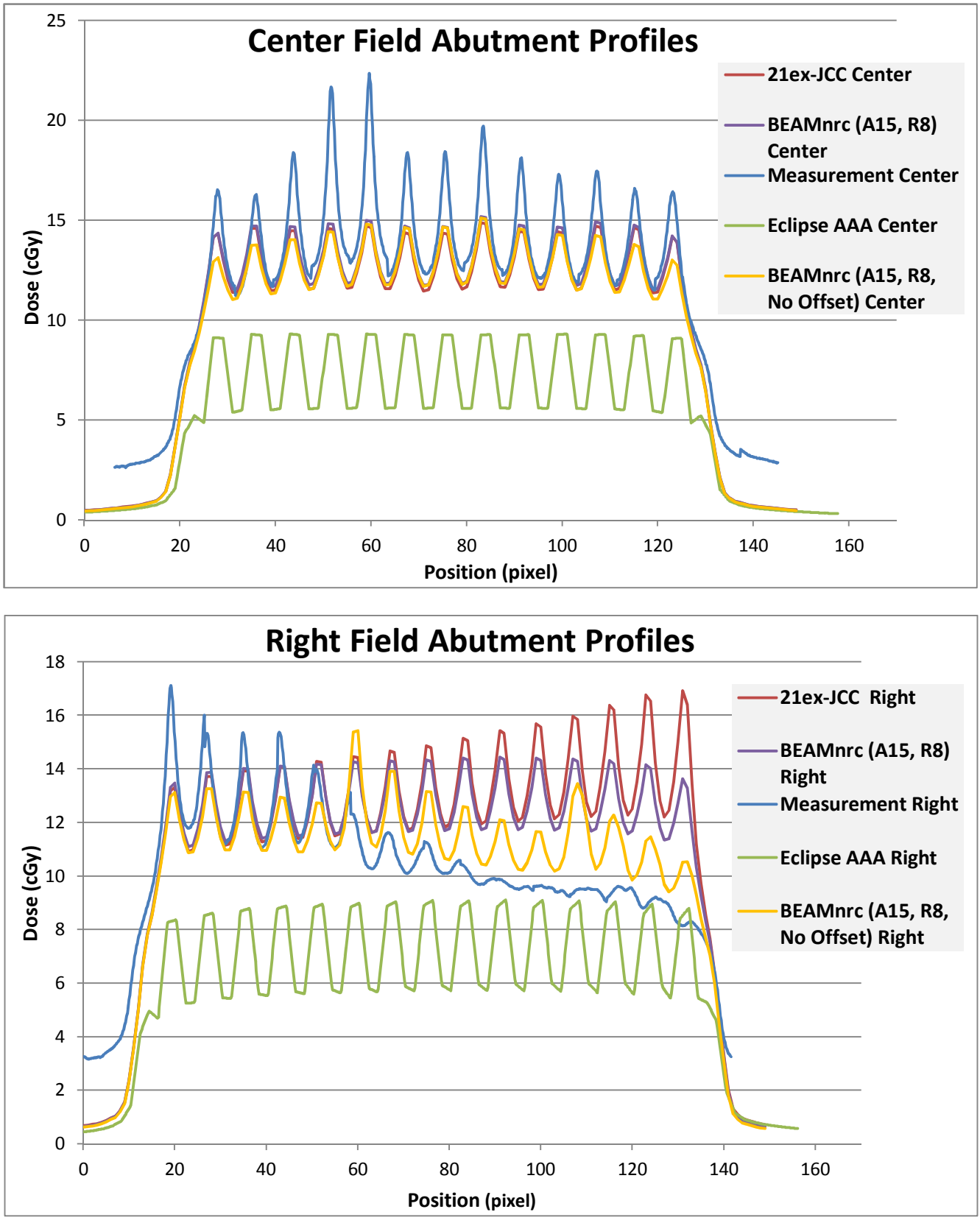

Graph 25. Demonstration of left, center and right fields abutment leakages profiles calculation using different machines against the measurements. Note that 1 cm equal to 8 pixel based on the resolution of the RAW images exported from Pinnacle

3.6.2 - 0.5 mm and 1 mm Gap Abutments Setup:

In this section, the same abutments plan with 0.5 and 1 mm gap have been recreated to insure that the linac would apply the MLC calibration offset table at the delivery level to synchronize with Pinnacle calculations. However, since the left field abutment profiles were an exact mirror of the right field abutment profiles, only center and right abutment profiles will be examined against the film measurements is this section.

Graphs 26 and 27, represent the comparison plot for 1 mm and 0.5 mm gap abutments setup respectively between the film measurements (green line), the 21ex-JCC (blue line) and BEAMnrc (A15, R8) (red line) profile calculations. The center field measured profiles for both setups have approximately the same pattern as the calculation at the profile valleys, while the right field profile excursions were dropping quicker at far edges. However, the right field profile measurements for both setups showed that the machine indeed applied the MLC offset table at the delivery. The calculations are in better agreement with measurements compared to the zero abutments setup. The 21ex-JCC was showing an increase of transmitted dose with increasing distance from central axis, while BEAMnrc (A15, R8) is in better agreements with measurements. This may indicate that 8 cm leaf tip radius is indeed a better choice for Pinnacle beam modeling. The 1 mm gap abutments measurements were showing higher profile peaks in comparison with 0.5 mm gap setup against the calculations. This is expected since more dose transmissions is transmitted when opposing leaves are separated by a larger gap. However, the peaks calculated values were still below those measured for the center and the right fields for both setups.

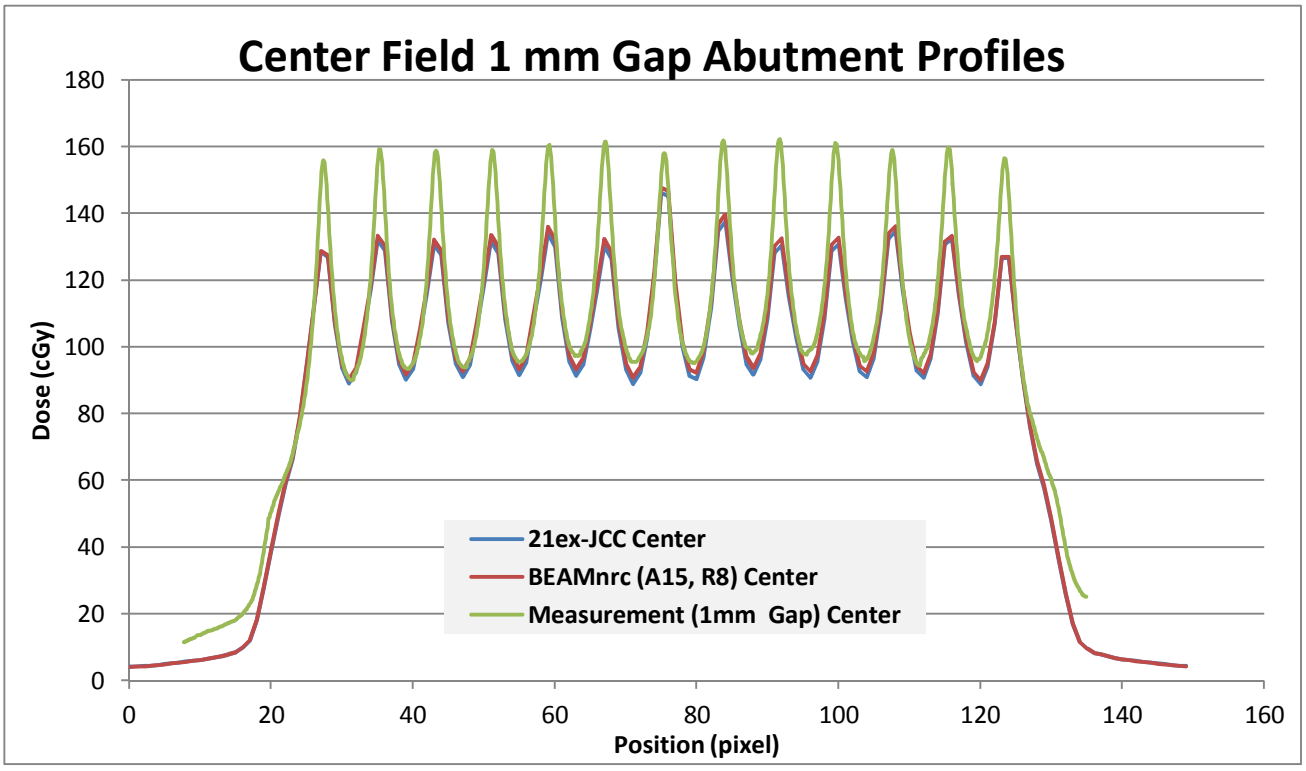

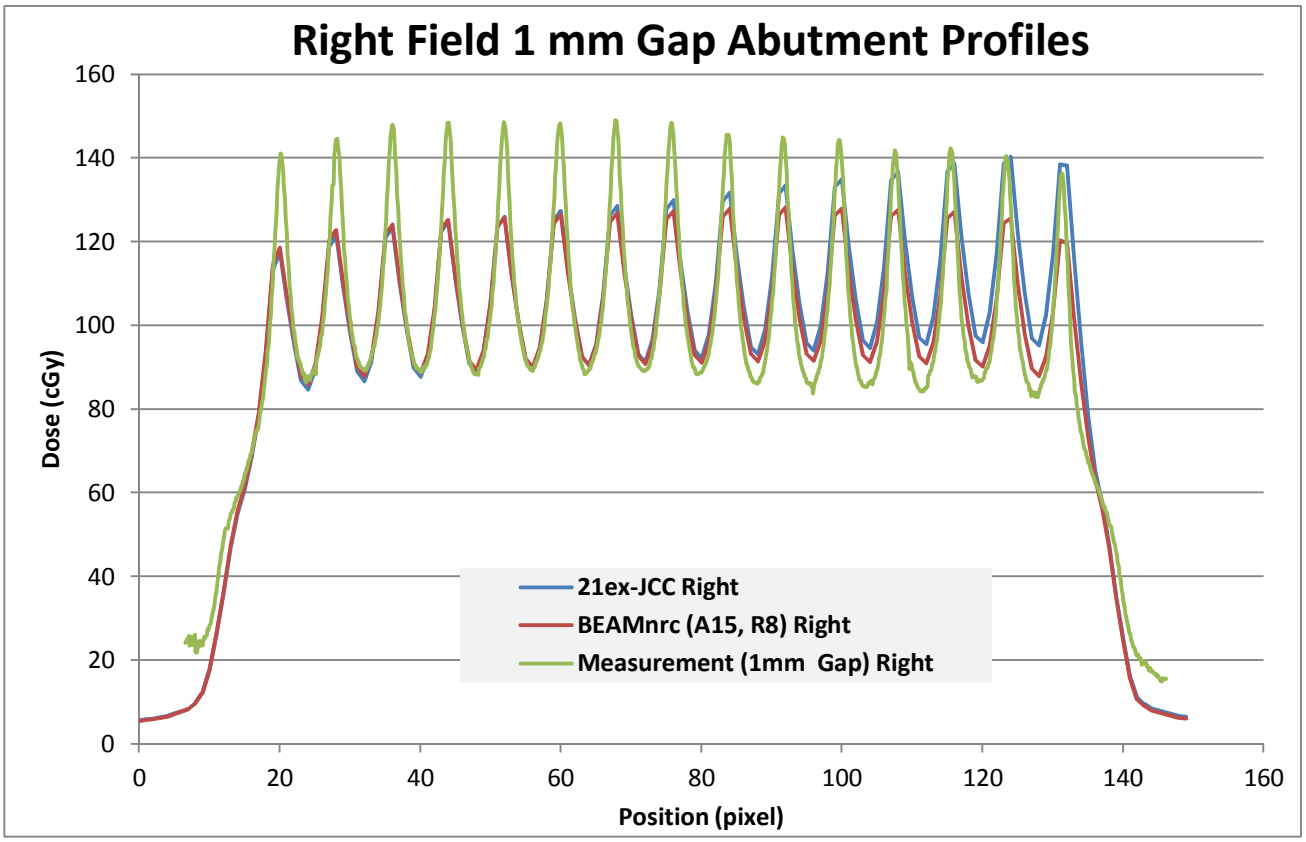

Graph 26. Demonstration of center and right fields 1 mm gap abutment profiles calculation using different machines against the measurements. Note that 1 cm equal to 8 pixel based on the resolution of the RAW images exported from Pinnacle

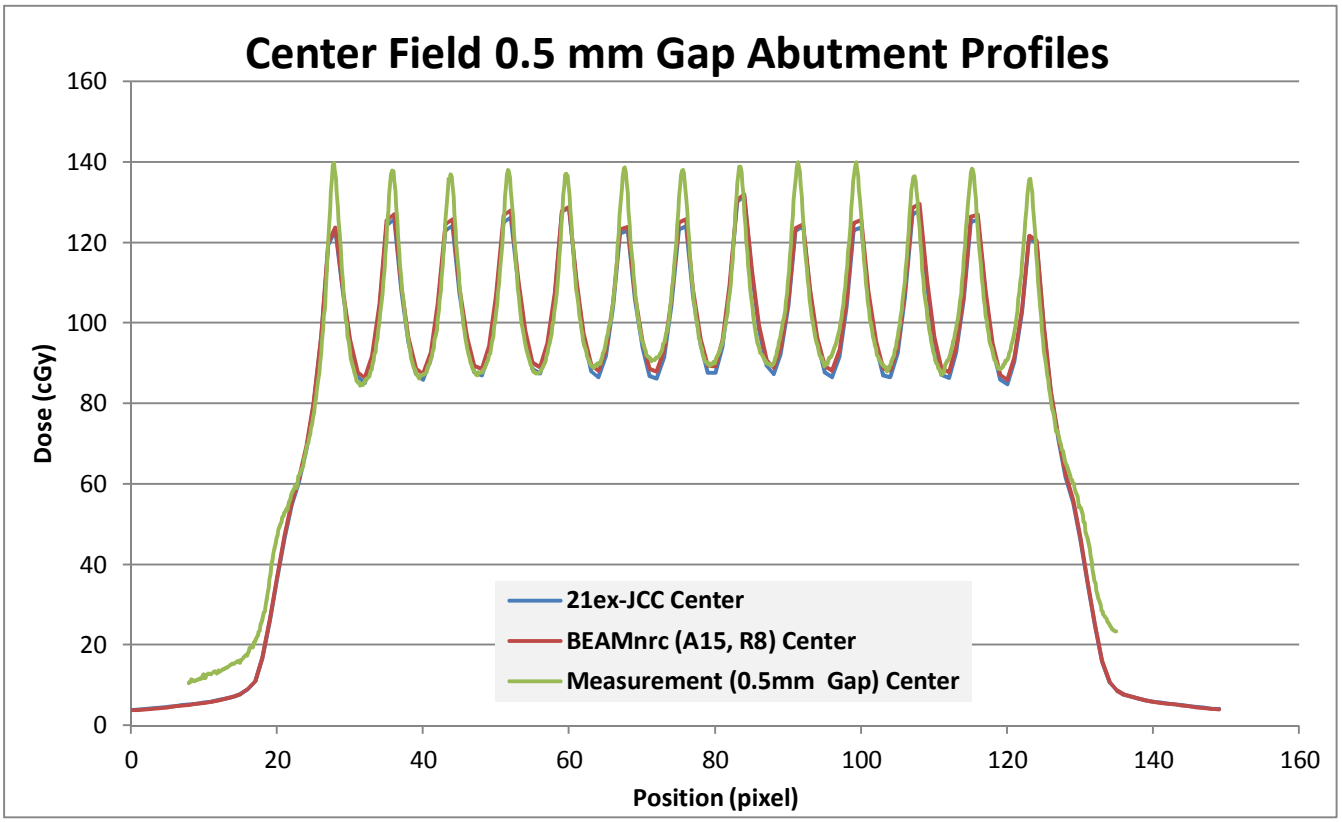

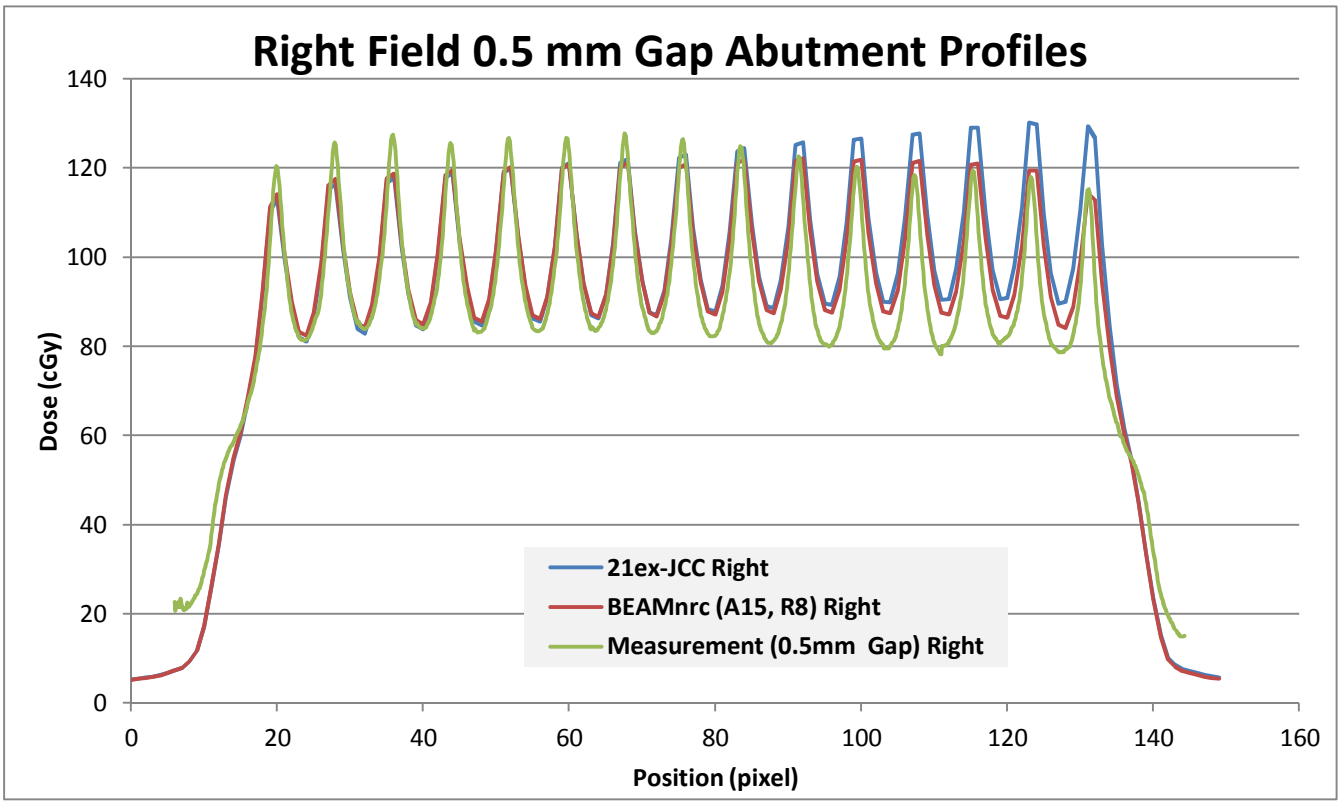

Graph 27. Demonstration of center and right fields 1 mm gap abutment profiles calculation using different machines against the measurements. Note that 1 cm equal to 8 pixel based on the resolution of the RAW images exported from Pinnacle

The larger measured dose peaks observed in graph 26 and 27 are an indication that Pinnacle beam modeling does not consider the transmission through the leaf ends properly. As was discussed in section 2.1.2, the Varian MLC rounded leaf ends are approximated as a circle segment that extends between the top and the bottom surface of the MLC as shown in figure 10. Small adjustments to the leaf separation similar to Eclipse DLS approach maybe the most appropriate choice to achieve the best model of a small gap between opposed leaves.

The adjustments that were made to the MLC calibration offset table to adjust the profile for MLC defined field in section 3.5 shows the best result in the calculation of these small gap abutments profile. This is shown in graph 28 for the profile calculated using BEAMnrc (A15, R8, O -0.045) (purple line) machine for the center and right field 1 mm gab abutments setup. The profile peaks are in better agreement with the film measurements, while the profile valleys shows some offset. This is since we have intentionally increased the separation between the opposed leaves by a fixed value of 0.9 mm. However, graph 28 also shows that adjusting the off-axis softening factor parameter to 6.5 and reducing the additional interleaf leakage transmission factor from 0.01 (1%) to 0.005 (0.5%) while retaining the remaining MLC modeling parameters of the 21ex-JCC has further improved the calculations. This is shown in the calculation of BEAMnrc (A15, R8, S6.5, O -0.045, A.I.L. 0.5%) (red line) machine.

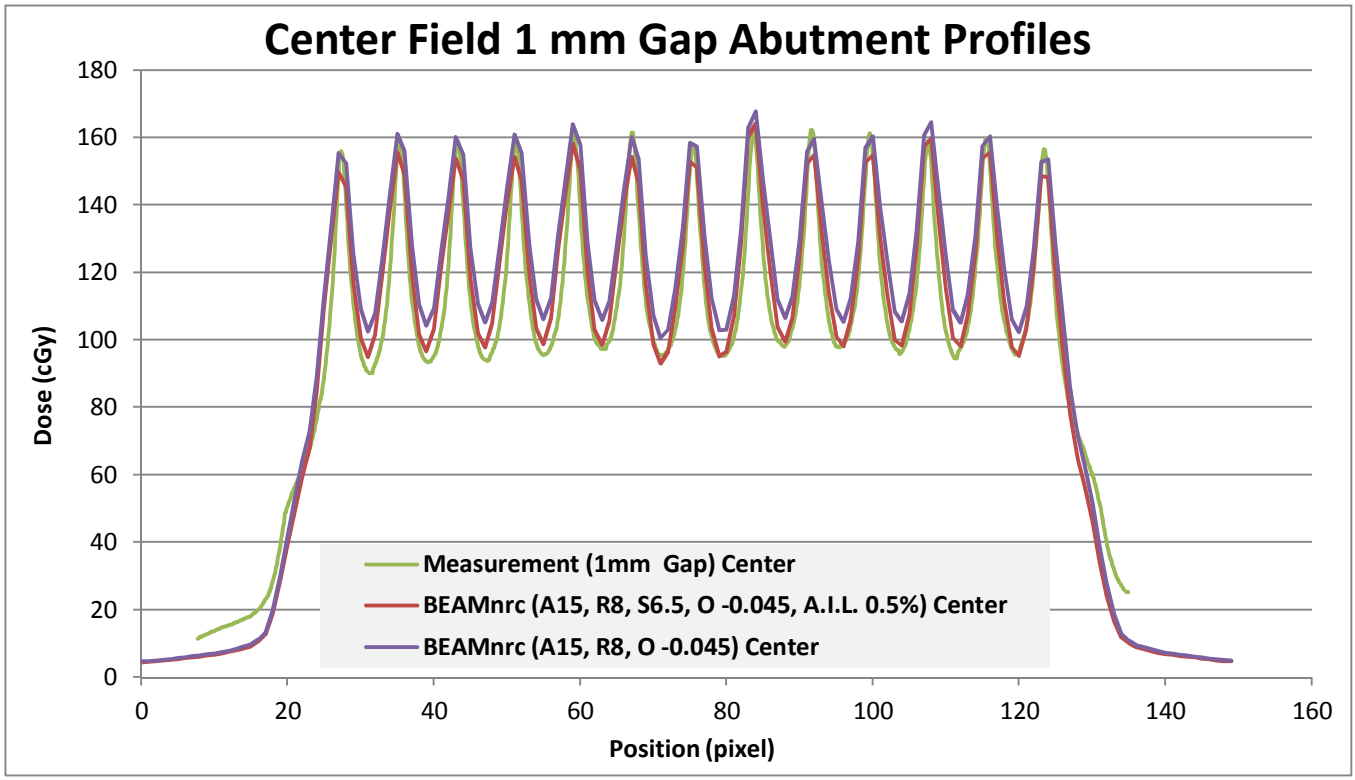

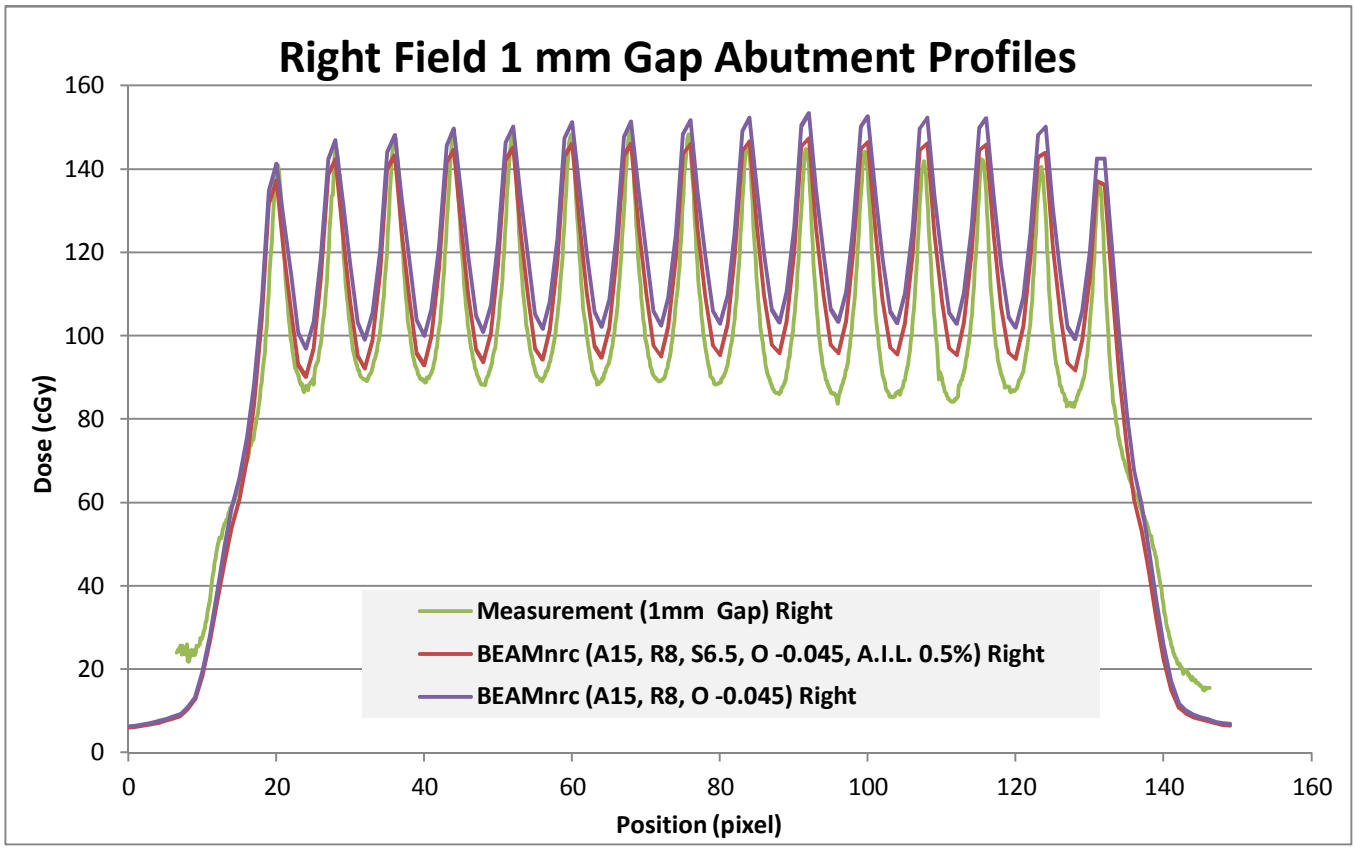

Graph 28. Demonstration of center and right fields 1 mm gap abutment profiles calculation using further adjustments to the Pinnacle beam modeling. Note that 1 cm equal to 8 pixel based on the resolution of the RAW images exported from Pinnacle

3.7 - Effect of Machine Parameters on Output Factor Calculation:

3.7.1 - Small Square Fields Setup:

In section 2.6.1, the setups performed by Klein *et al*, 2010[30] to measure the output factor for small fields defined by either jaws or MLC were described. The MLC setup involves two configurations; a centered abutted MLC and an offset 4 cm abutted MLC. Their measurements were performed using a plastic scintillation detector (PSD) of 0.5 mm diameter and 2 mm length. The measured data were extracted from their paper and renormalized to a 10 x 10 cm^2 field. Their setups were reproduced in Pinnacle and the collected data were normalized to a 10 x 10 cm^2 field. Furthermore, the exact setups were delivered at the machine and the measured data were collected using a Sun-point diode detector for comparison. The output factor data were plotted for comparison and conclusion.

Graph 29 (A) and (B) represents the centered and the 4 cm offset abutted MLC setups respectively. The graph shows the PSD data (blue line) plotted against the Sun-point diode measurements (red line), the 21ex-JCC (green line dots) and Eclipse AAA (purple line dots) calculations. The diode output factor measurements were slightly below the PSD for fields larger than 2 cm up to 8 cm. This was more pronounced for the 4 cm offset abutted MLC, while the diode data over estimated the dose for fields less that 2 cm in both configurations. This observation is in agreement with the literature, since diodes generally over-respond at small fields due to their densities (Scott *et al*, 2012)[38]. Scott *et al*, 2012[38], have shown that at small field sizes, high-density detectors over-read, while low-density detectors under-read. This correlates with the mass density

of the detector material active volume relative to water density rather than the differences in atomic number, while the average atomic number of the detector material would influence the measurements at all field sizes. Thus, in a relative dosimeter, the atomic number is not important for measurements of small fields relative to centered larger reference field (Scott *et al*, 2012)[38].

Scott *et al*, 2012[38] developed Monte Carlo calculated density correction factors, $F_{detector}$, to convert the detector- measured small-field doses into true values in water. They have found that this correction might improve the accuracy of small-field doses measured on-axis. However, they also showed experimentally that this correction may make the integral dose less accurate. This is because implementing a correction by rescaling the measured small-field doses using on-axis correction values would lead to improper estimation of the delivered integral doses, especially by techniques such as IMRT since it is encountering a large number of overlapping off-axis small fields. The authors suggested a better approach would be to use small-field relative detectors that have an active volume density similar to water.

Another factor that would influence the measurements is the encapsulation and the shielding of the diode. In general, for photon field dosimetry, the diode is shielded by a high atomic number material (usually tungsten), which is integrated into the encapsulation to selectively absorb-low energy photons that would cause the diode to over respond (Eklund and Ahnesjö, 2010)[39]. Diode detectors use silicon, which is a semiconductor material that has a high electron density and gives a strong signal per detector volume. Thus, a silicon diode can be made thousands of times smaller than an ion chamber, while its sensitivity can be 10 times higher, which makes it a preferable

choice for small field dosimetry. However, in situations where a large part of the deposited dose originated from scattered low-energy photons, such as at deeper depths in a large field, silicon diodes overestimate the absorbed dose. In order to compensate for that, silicon diodes used in photon dosimetry are equipped with shielding material to partially absorb the low-energy photons. This shielding is made based on empirical testing and manufacturing compromises, rather than theoretical detailed investigations (Eklund and Ahnesjö, 2010)[39]. Moreover, a common practice in manufacturing is to encapsulate the silicon diodes with plastic for the matter of protection and to simplify mounting on scanning devises. A Monte Carlo simulation made by Eklund and Ahnesjö, 2010[39] was aimed to investigate the effect of the encapsulation for both shielded and unshielded diodes by studying the spectra changes at the detector cavity. They found that shielding the silicon diode caused not only the desired decreases in low-energy photons, but also caused an increase of the primary electron fluence at the detector cavity. Furthermore, they have found that these perturbations are independent on the depth of measurement. However, the response from a shielded diode is not completely independent of field size-dependent scattering as it should be. This was also validated with measurements. Nevertheless, this encapsulation around the silicon may also influence the dose response for both shielded and unshielded diodes. However, the degree of disturbance on spectra was very slight for the unshielded diodes in comparison with the shielded diodes. The authors demonstrated that unshielded diodes used together with an appropriate correction are much better for photon relative dosimetry.

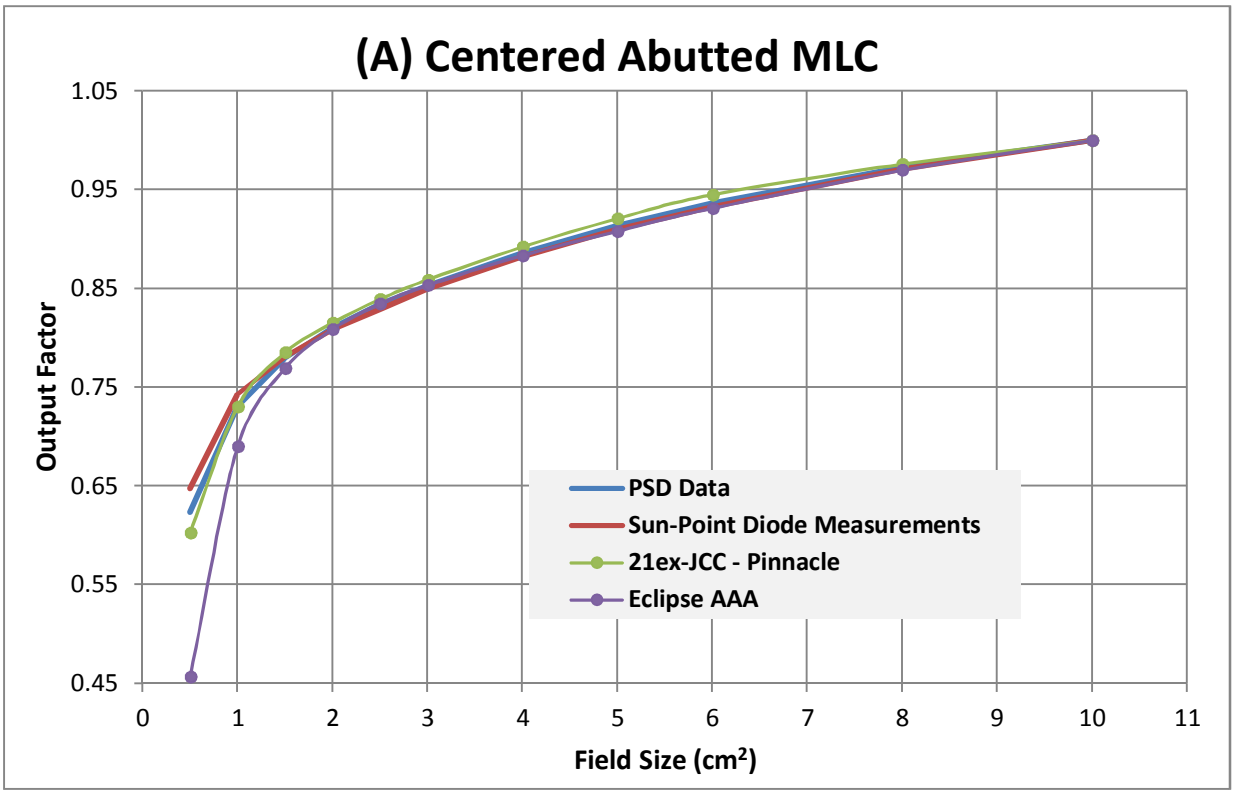

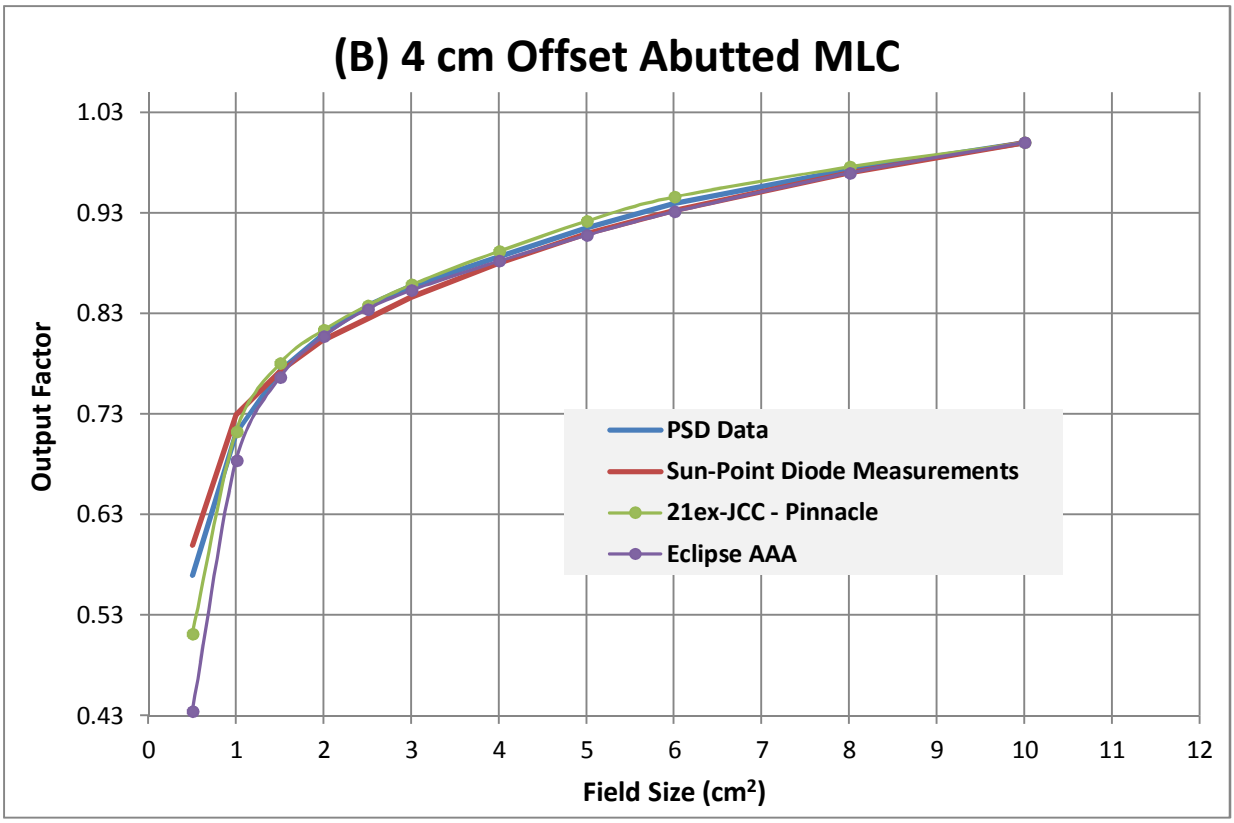

Graph 29 (A) Centered Abutted MLC and (B) 4 cm Offset Abutted MLC. The graph demonstrates the output factor plot of the PSD[30] against the 21ex-JCC and Eclipse AAA calculation. The Sun-point diode measurements are also plotted. The data are normalized to 10 x 10 cm² MLC defined field. The jaws was set at 20 x 20 cm²

In graph 29, it has to be noted that the PSD error in the output factor measurements ranged between 0.19% to 0.48% for the centered abutted MLC setup. The error bars for the 4 cm offset abutted MLC were very similar, ranging from 0.21% to 0.43%. These were the error bars in y-direction (not shown in graph). Furthermore, there is a fixed uncertainty in the x-direction of 1 mm (not shown in graph) to account for the PSD positioning variation and MLC/jaws traveling error (Klein *et al*, 2010)[30]. This 1 mm x-direction fixed error has also been validated using the JCC quality assurance record, which can be applied for the diode measurements. Furthermore, the Sun-point diode has ±0.2% stability[32] while the electrometer (FLUKE 35040) used for the measurements has an accuracy of ±0.2%[40]. The approximate expected error bars in the y-direction would be about 0.28% for the Sun-point diode measurements.

Graph 29 also shows the calculation of the 21ex-JCC and Eclipse AAA output factors against the PSD. At smaller field sizes (less than 1.5 cm^2), Pinnacle and Eclipse underestimated the dose. However, the Eclipse dose was far below that calculated by Pinnacle, e.g., at 0.5 x 0.5 cm^2 field, the 21ex-JCC and Eclipse under-read by -3.44% and -26.85% respectively for the centered abutted MLC, While they both under-read by -10.19% and -23.78% respectively for the 4 cm offset abutted MLC. The 21ex-JCC performed better at smaller field size calculation. However, the calculation appeared to be much better for the centered abutted MLC. Conversely, for larger field sizes ranged from 2 x 2 up to 8 x 8 cm^2, the 21ex-JCC overestimated the dose slightly by an average of 0.63% for the center abutted MLC and by 0.43% for the offset abutted MLC, while Eclipse on average slightly underestimated the dose by -0.30% and -0.53% respectively. The difference was more pronounced at the 4 cm offset abutted MLC for the Eclipse

calculation. However, it can be seen from graph 29 that the Eclipse AAA calculation performed slight better at larger field sizes compared with Pinnacle 21ex-JCC for fields defined by MLC.

Graph 30 presents the PSD and Sun-point diode measurements output factor against the 21ex-JCC and Eclipse AAA calculation for field defined by jaws only. The total uncertainty for the PSD ranged from 0.52% to 0.81% (Klein *et al*, 2010)[30].

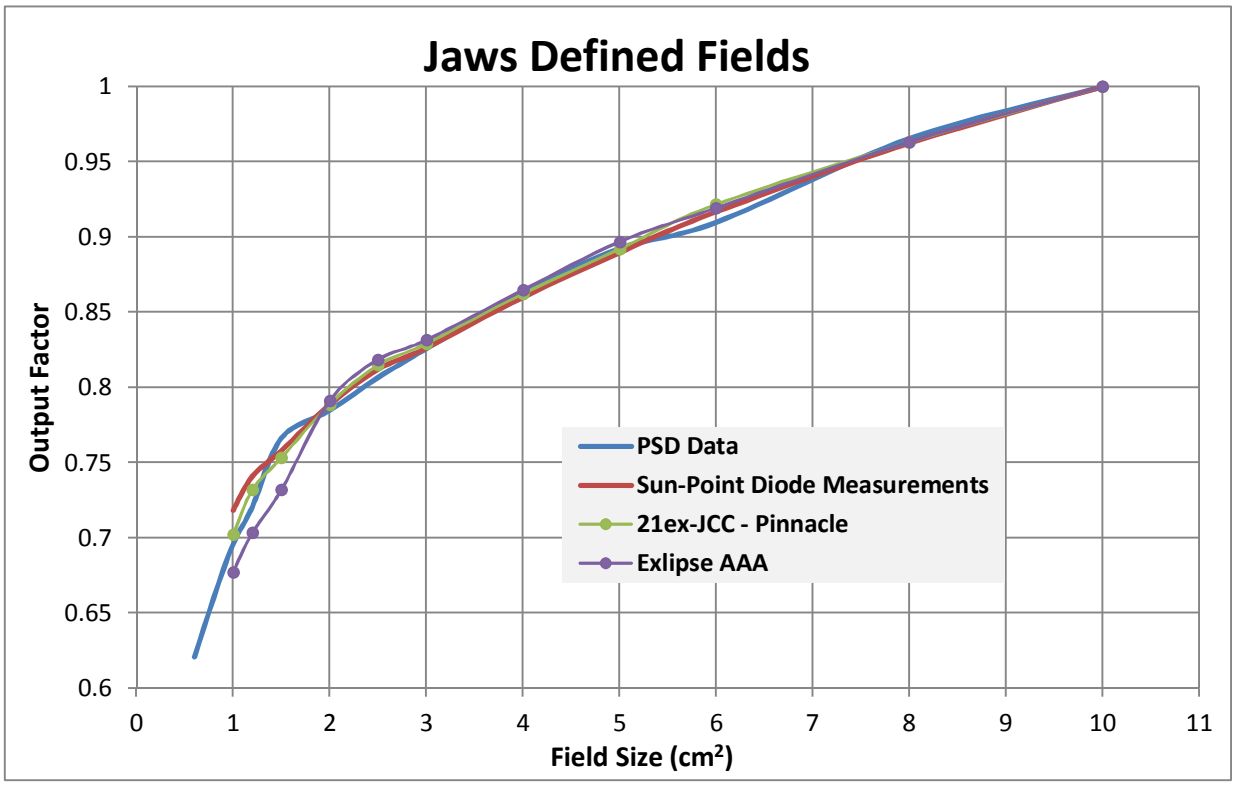

Graph 30. Output factor for field defined by jaws showing plot of the PSD[30] against the 21ex-JCC and Eclipse AAA calculation. The Sun-point diode measurements are also plotted. The whole data are normalized to 10 x 10 cm^2 jaws open field.

Similar to the MLC defined fields, the diode measurements overestimated the dose compared with the PSD data at smaller fields. However, at 6 x 6 cm^2 field, the diode measurements exceeded the PSD, unlike the MLC defined fields. This might be due to an error in the PSD or the diode measurements. Moreover, it can be seen from

the graph that Pinnacle 21ex-JCC performed better in comparison with Eclipse AAA calculation at all field size defined by jaws.

In order to test the new models, the percentage difference between the PSD and the 21ex-JCC output factor was calculated and the process repeated for the other models. Graphs 31 A and B shows the percentage error calculations of the 21ex-JCC (blue dots) with the BEAMnrc (A15) (green dots) for the centered abutted MLC and the 4 cm offset abutted MLC respectively. The graph shows that using the 15 cm water attenuated BEAMnrc spectrum leads to a better slight estimation of the dose. However, for the center abutted MLC at 4 x 4 cm^2 field, the 21ex-JCC has better result only.

Graph 32-A compares the 21ex-JCC (blue dots) percentage error against various machines for the centered abutted MLC setup. The graph shows that using the BEAMnrc (A15, R8) (red square) that has the nominal 8 cm leaf tip radius of curvature has further improved the calculation of the BEAMnrc (A15) for field size smaller than 6 x 6 cm^2. Adjusting the off-axis softening factor to 6.5 has only improved the calculation at 0.5 x 0.5 cm^2 for the output factor (green dots). Using a 12 cm leaf tip radius led to good results except at fields less that 1 x 1 cm^2 (orange dots). The adjustments that we made to the MLC offset table were most effective at smaller field sizes. This is shown for the BEAMnrc (A15, R8, O -0.045, S6.5) (purple x), where the error was reduced to less than 1.17% for a 0.5 x 0.5 cm^2 field compare to -3.44% for the 21ex-JCC calculation error against the PSD data. It also shows a slight improvement for the 8 x 8 cm^2 field output factor calculation. The extra adjustments that were made to the additional interleaf transmission did not lead to a significant difference in the computed output factor (cyan x).

Graph 32-B compares the 21ex-JCC (blue dots) percentage error against various machines for the 4 cm offset abutted MLC setup. Similarities can be seen as to the centered abutted MLC output factor percentage error calculations shows in graph 32-A. However, as seen in graph 32-B, there were a slight improvements to the calculation of the output factor at larger field sizes for the new models. Moreover, the BEAMnrc (A15, R8, O -0.045, S6.5) underestimates the dose by -5.25% for a 0.5 x 0.5 cm^2 field compare to -10.19% for the 21ex-JCC. Tables 4 and 5, tabulate the percentage error calculated using the various Pinnacle models against the PSD data for centered and the 4 cm offset abutted MLC.

For field defined by jaws only as shown in graph 30, the output factor will be the same as the 21ex-JCC clinical machine for all machines. This is because Pinnacle applies a field-size dependent correction factor (OFc) to correct the Pinnacle modeled output factor (OFp) to match the measured output factor (OF) as was discussed in section 2.3.1. Discussion and conclusions will be presented in detail in chapter 4.

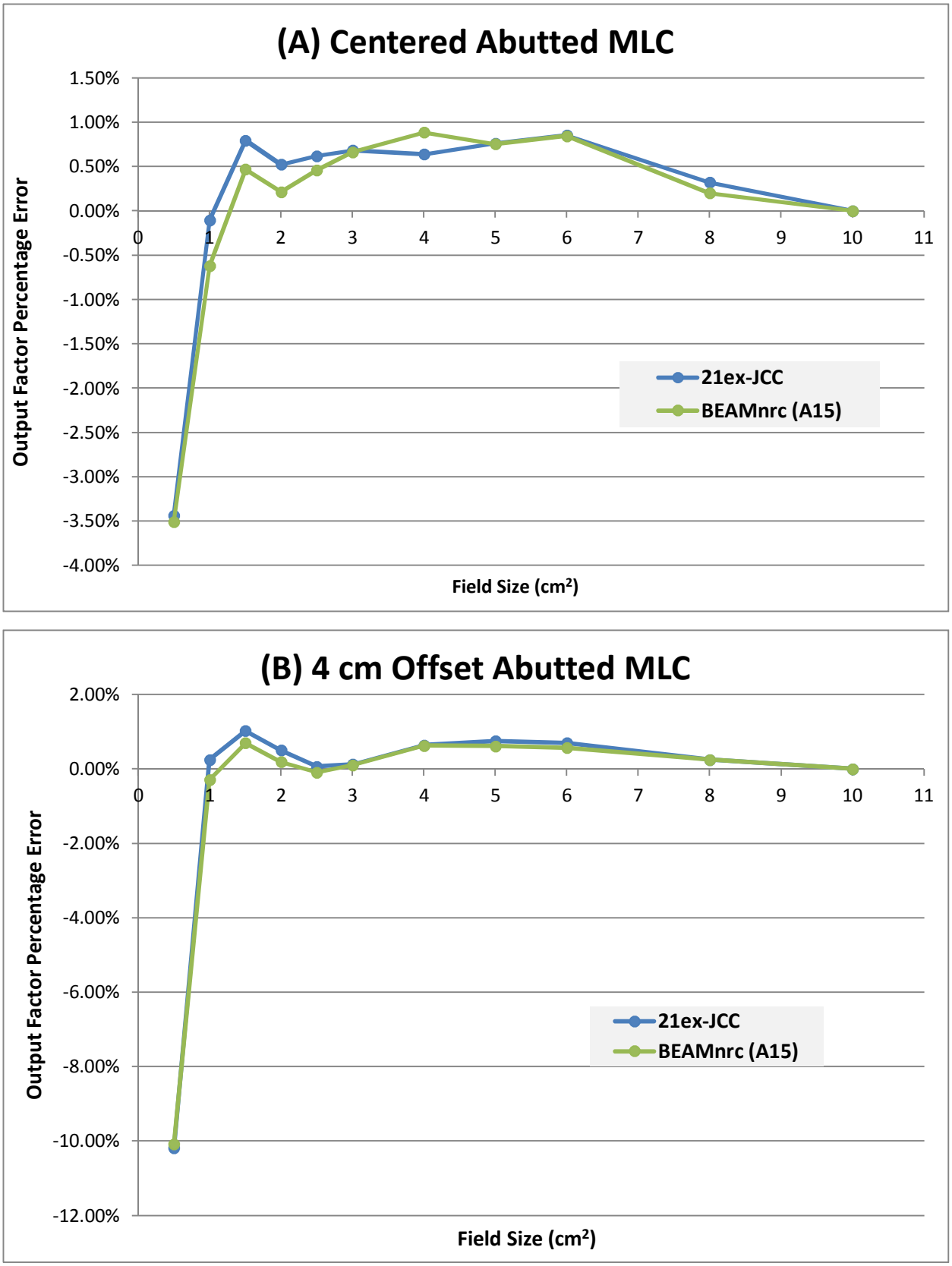

Graph 31 (A) Centered Abutted MLC and (B) 4 cm Offset Abutted MLC. The graph demonstrates the output factor % error plot between the 21ex-JCC and the BEAMnrc (A15). The % error is based on the PSD data

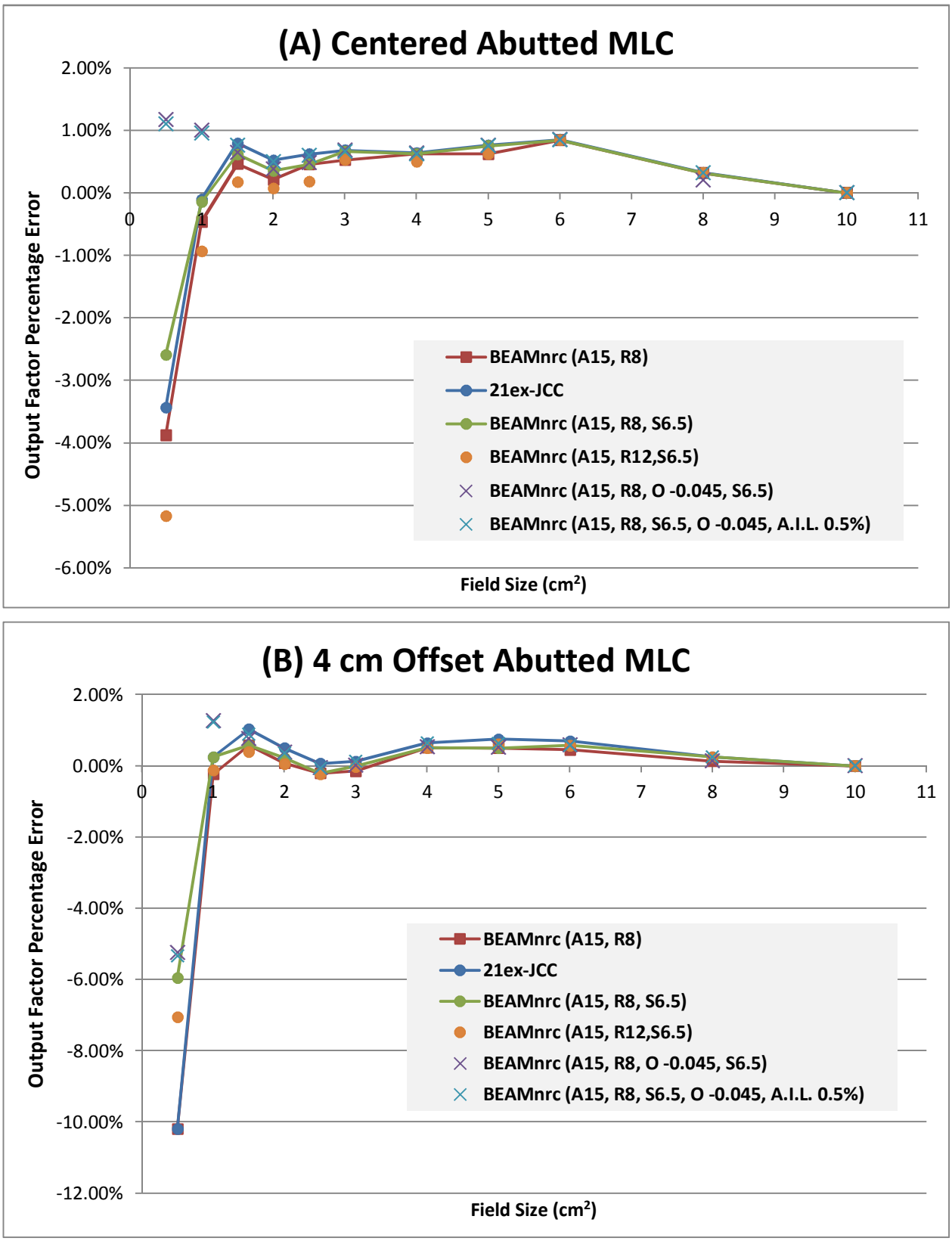

Graph 32 (A) Centered Abutted MLC and (B) 4 cm Offset Abutted MLC. The graph demonstrates the output factor % error plot between the 21ex-JCC and different examined machines. The % error is based on the PSD data

F.S (cm^2)	% error between Sun-Diode and PSD	Eclipse % Error compared to PSD	21ex-JCC % Error compared to PSD	BEAMnrc (A15)% Error compared to PSD	BEAMnrc (A15, R8)% Error compared to PSD	BEAMnrc (A15, R8, S6.5) % Error compared to PSD	BEAMnrc (A15, R12, S6.5) % Error compared to PSD	BEAMnrc (A15, R8, O -0.045, S6.5) % Error compared to PSD	BEAMnrc (A15, R8, S6.5, O -0.045, A.I.L. 0.5%) % Error compared to PSD
0.5	3.81%	-26.85%	-3.44%	-3.51%	-3.88%	1.17%	-5.17%	1.17%	1.10%
1	1.68%	-5.61%	-0.10%	-0.62%	-0.46%	1.00%	-0.93%	1.00%	0.96%
1.5	0.20%	-1.27%	0.80%	0.47%	0.47%	0.65%	0.17%	0.65%	0.76%
2	-0.28%	-0.25%	0.52%	0.21%	0.21%	0.38%	0.07%	0.38%	0.50%
2.5	-0.57%	0.05%	0.62%	0.46%	0.46%	0.48%	0.18%	0.48%	0.60%
3	-0.40%	0.02%	0.68%	0.66%	0.53%	0.68%	0.53%	0.68%	0.66%
4	-0.47%	-0.33%	0.64%	0.89%	0.63%	0.64%	0.50%	0.64%	0.63%
5	-0.43%	-0.65%	0.76%	0.75%	0.63%	0.76%	0.63%	0.76%	0.75%
6	-0.45%	-0.61%	0.85%	0.85%	0.85%	0.85%	0.85%	0.85%	0.85%
8	-0.18%	-0.32%	0.32%	0.20%	0.32%	0.20%	0.32%	0.20%	0.32%
10	0.00%	0.00%	0.00%	0.00%	0.00%	0.00%	0.00%	0.00%	0.00%

Table 4. Calculated percentage error against the PSD for the centered abutted MLC

F.S (cm^2)	% error between Sun-Diode and PSD	Eclipse % Error compared to PSD	21ex-JCC % Error compared to PSD	BEAMnrc (A15)% Error compared to PSD	BEAMnrc (A15, R8)% Error compared to PSD	BEAMnrc (A15, R8, S6.5) % Error compared to PSD	BEAMnrc (A15, R12, S6.5) % Error compared to PSD	BEAMnrc (A15, R8, O -0.045, S6.5) % Error compared to PSD	BEAMnrc (A15, R8, S6.5, O -0.045, A.I.L. 0.5%) % Error compared to PSD
0.5	5.27%	-23.78%	-10.19%	-10.08%	-10.19%	-5.95%	-7.05%	-5.25%	-5.34%
1	2.64%	-3.81%	0.25%	-0.28%	-0.24%	0.25%	-0.12%	1.26%	1.22%
1.5	-0.10%	-0.76%	1.03%	0.70%	0.58%	0.58%	0.40%	0.76%	0.88%
2	-0.77%	-0.28%	0.50%	0.19%	0.08%	0.22%	0.05%	0.39%	0.36%
2.5	-1.49%	-0.37%	0.07%	-0.09%	-0.21%	-0.21%	-0.23%	-0.05%	-0.07%
3	-1.29%	-0.53%	0.12%	0.10%	-0.14%	-0.01%	-0.03%	0.01%	0.12%
4	-0.66%	-0.46%	0.64%	0.63%	0.51%	0.51%	0.50%	0.53%	0.64%
5	-0.63%	-0.78%	0.75%	0.62%	0.50%	0.50%	0.62%	0.51%	0.63%
6	-0.73%	-0.88%	0.70%	0.57%	0.45%	0.58%	0.57%	0.58%	0.58%
8	-0.33%	-0.39%	0.25%	0.25%	0.13%	0.25%	0.25%	0.14%	0.25%
10	0.00%	0.00%	0.00%	0.00%	0.00%	0.00%	0.00%	0.00%	0.00%

Table 5. Calculated percentage error against the PSD for the 4 cm offset abutted MLC

3.7.2 - Long and Narrow Irregular Fields Setup:

In order to further examine the machine parameter adjustments on output factor calculation, a series of long and narrow MLC defined fields were created. However, different collimator rotations would force the MLC leaves to be staggered as shown in figure 16. Therefore, the setup was also repeated throughout a series of collimator angles in order to check the accuracy of Pinnacle calculation. The experimental setup was discussed in detail in section 2.6.2. Measurements were performed using a Sun-point diode detector, however, the diode detector may overestimate the dose at smaller fields due to its high density (full details were explained at section 3.7.1). The output factors were calculated relative to 10 x 10 cm^2 open field for the calculated and measured data. Graph 33 shows the percentage error for the diode measurements and the various machine models for the series of collimator angles plotted against slit width.

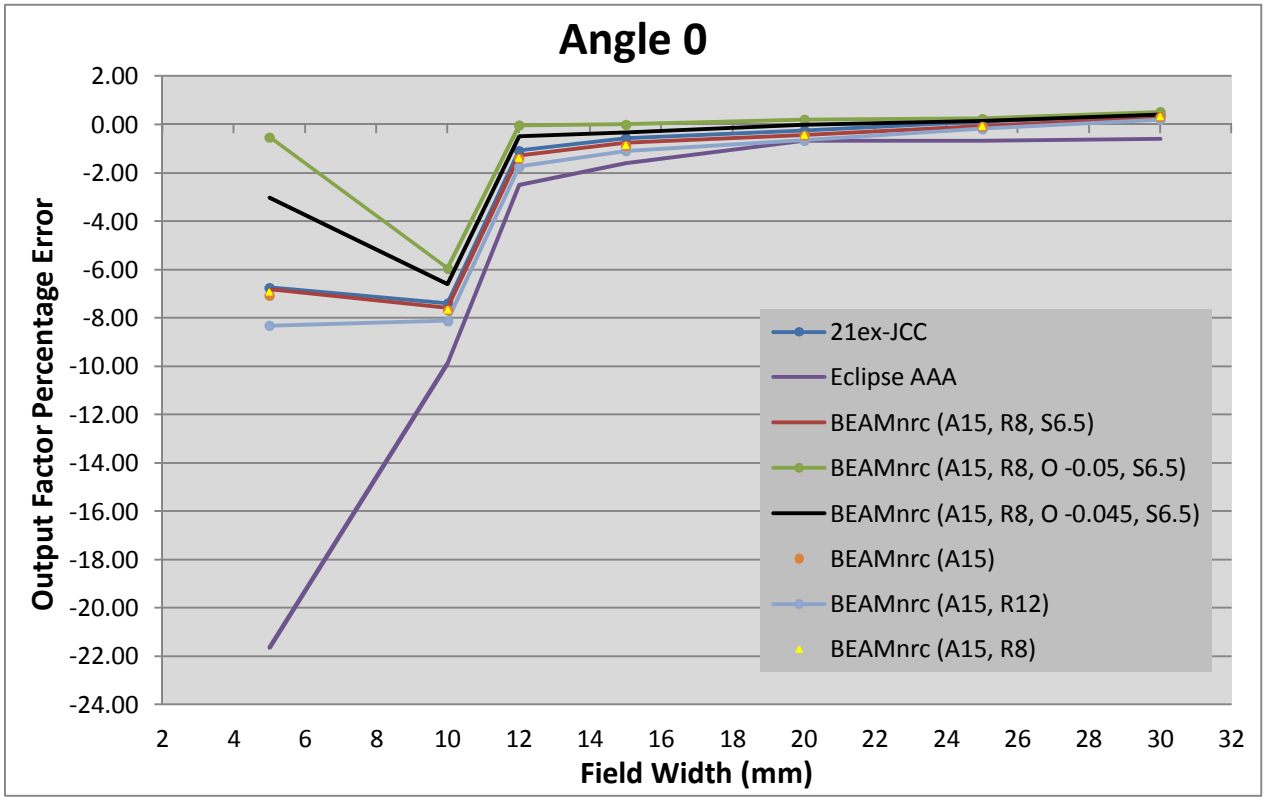

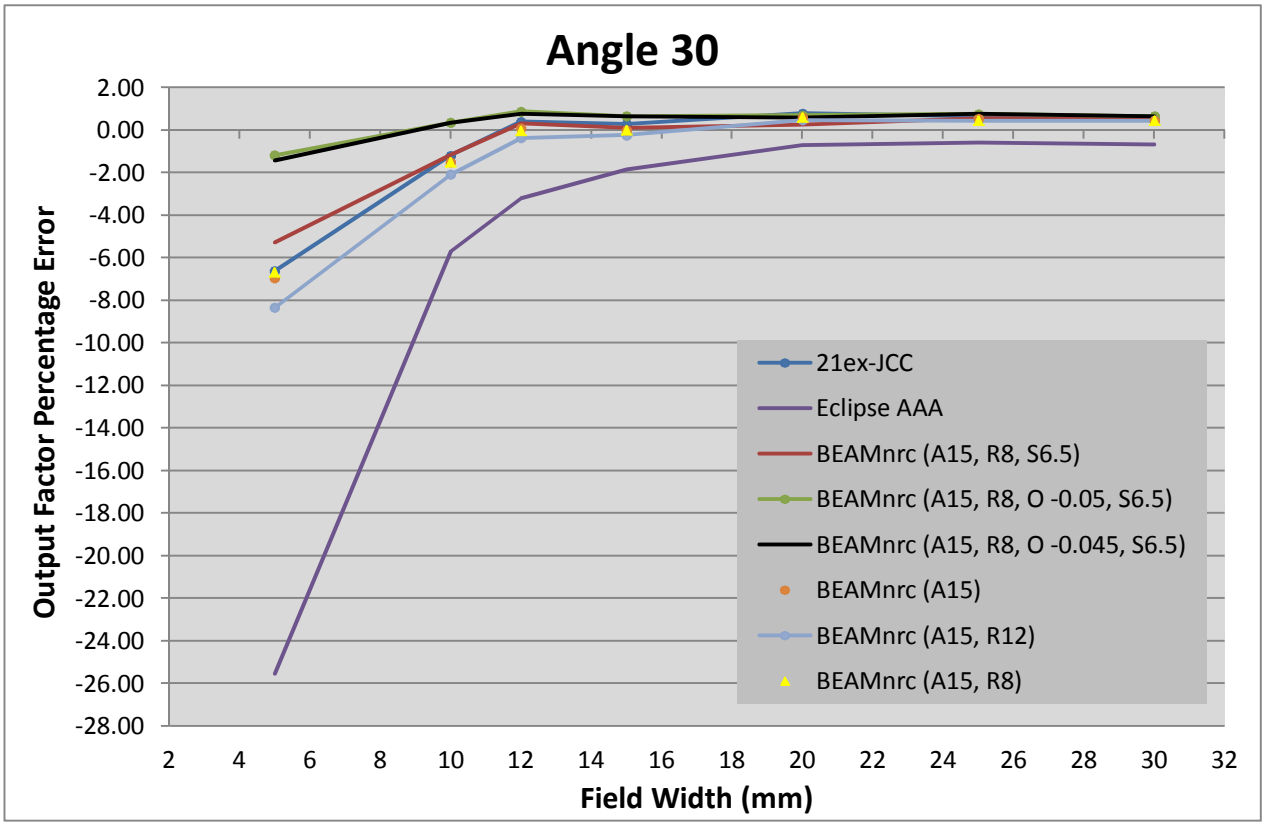
Angle 30
Output Factor Percentage Error
2.00
0.00
-2.00
-4.00
-6.00
-8.00
-10.00
-12.00
-14.00
-16.00
-18.00
-20.00
-22.00
-24.00
-26.00
-28.00
2
4
6
8
10
12
14
16
18
20
22
24
26
28
30
32
Field Width (mm)
21ex-JCC
Eclipse AAA
BEAMnrc (A15, R8, S6.5)
BEAMnrc (A15, R8, O -0.05, S6.5)
BEAMnrc (A15, R8, O -0.045, S6.5)
BEAMnrc (A15)
BEAMnrc (A15, R12)
BEAMnrc (A15, R8)

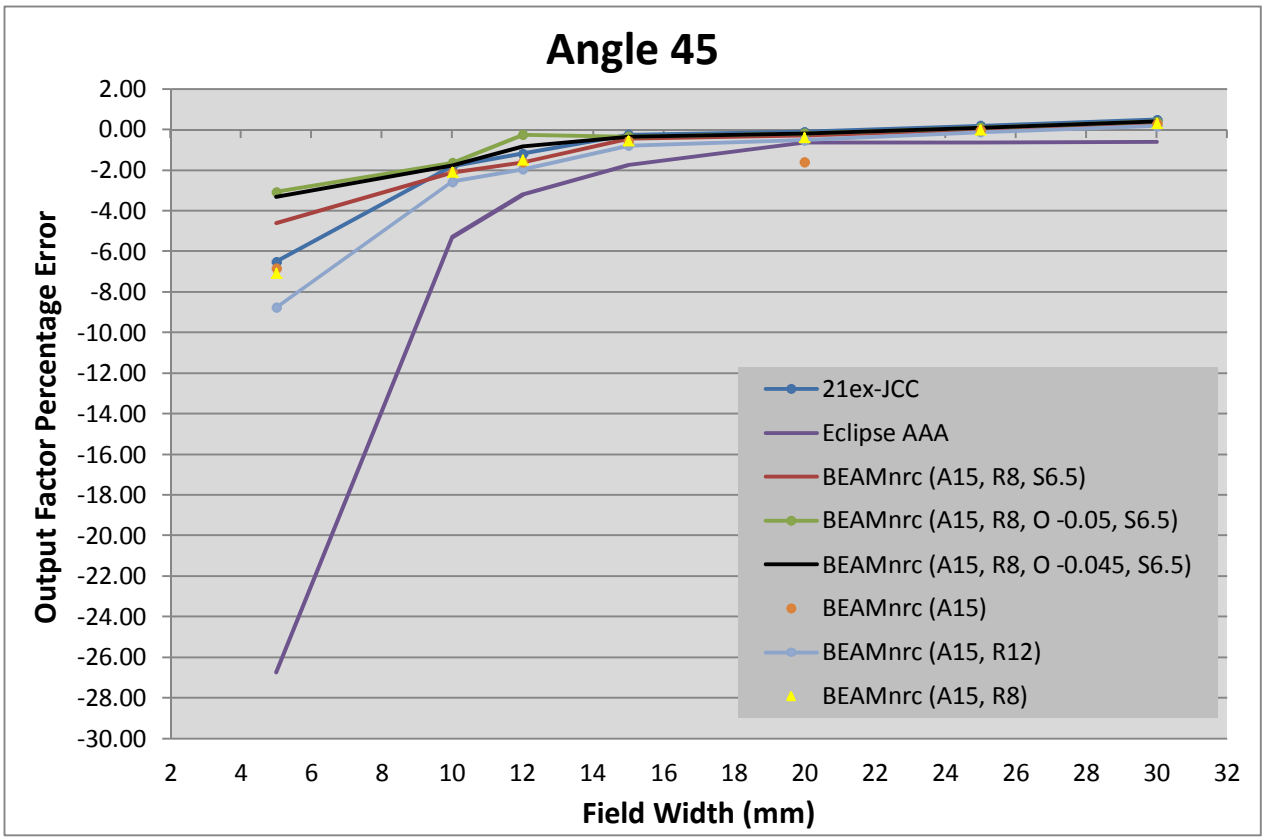
Angle 45
Output Factor Percentage Error
2.00
0.00
-2.00
-4.00
-6.00
-8.00
-10.00
-12.00
-14.00
-16.00
-18.00
-20.00
-22.00
-24.00
-26.00
-28.00
-30.00
2
4
6
8
10
12
14
16
18
20
22
24
26
28
30
32
Field Width (mm)
21ex-JCC
Eclipse AAA
BEAMnrc (A15, R8, S6.5)
BEAMnrc (A15, R8, O -0.05, S6.5)
BEAMnrc (A15, R8, O -0.045, S6.5)
BEAMnrc (A15)
BEAMnrc (A15, R12)
BEAMnrc (A15, R8)

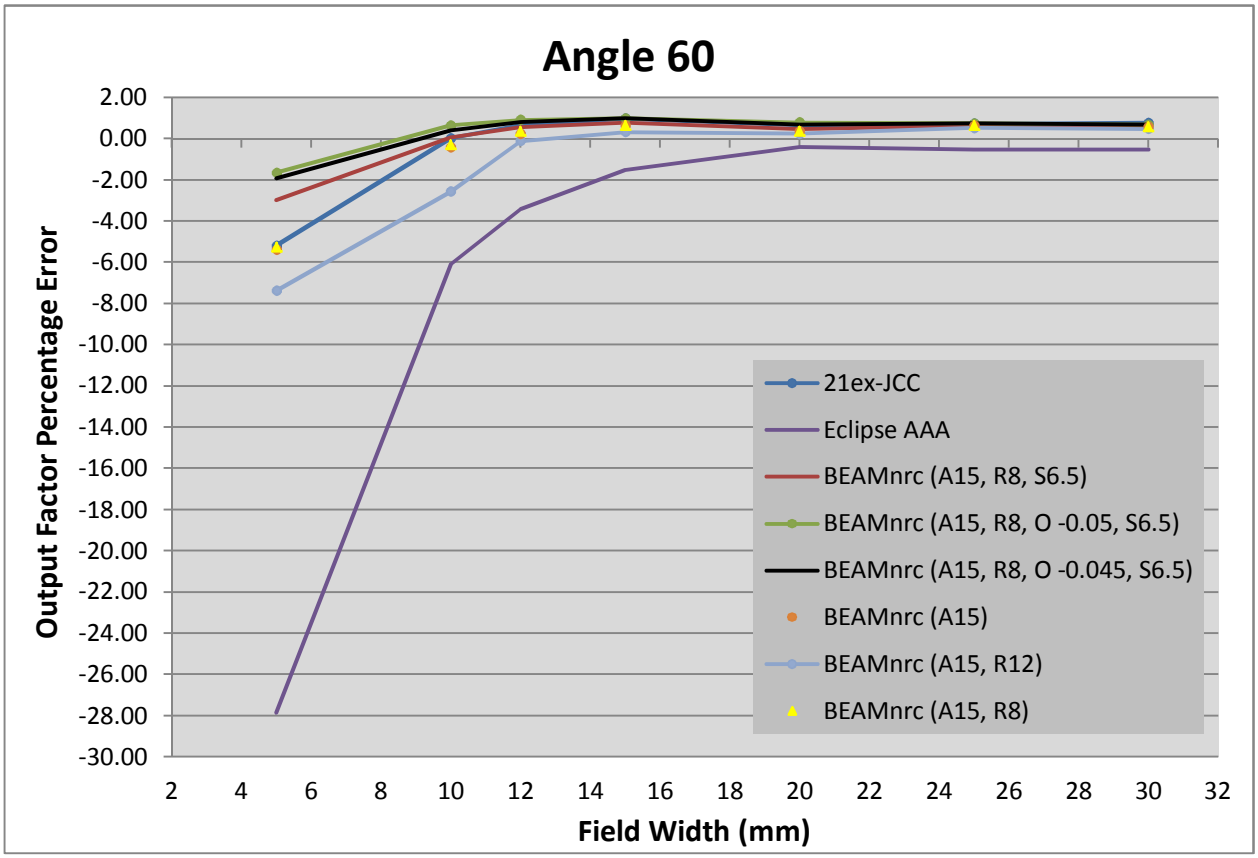
Angle 60
Output Factor Percentage Error
2.00
0.00
-2.00
-4.00
-6.00
-8.00
-10.00
-12.00
-14.00
-16.00
-18.00
-20.00
-22.00
-24.00
-26.00
-28.00
-30.00
2
4
6
8
10
12
14
16
18
20
22
24
26
28
30
32
Field Width (mm)
21ex-JCC
Eclipse AAA
BEAMnrc (A15, R8, S6.5)
BEAMnrc (A15, R8, O -0.05, S6.5)
BEAMnrc (A15, R8, O -0.045, S6.5)
BEAMnrc (A15)
BEAMnrc (A15, R12)
BEAMnrc (A15, R8)

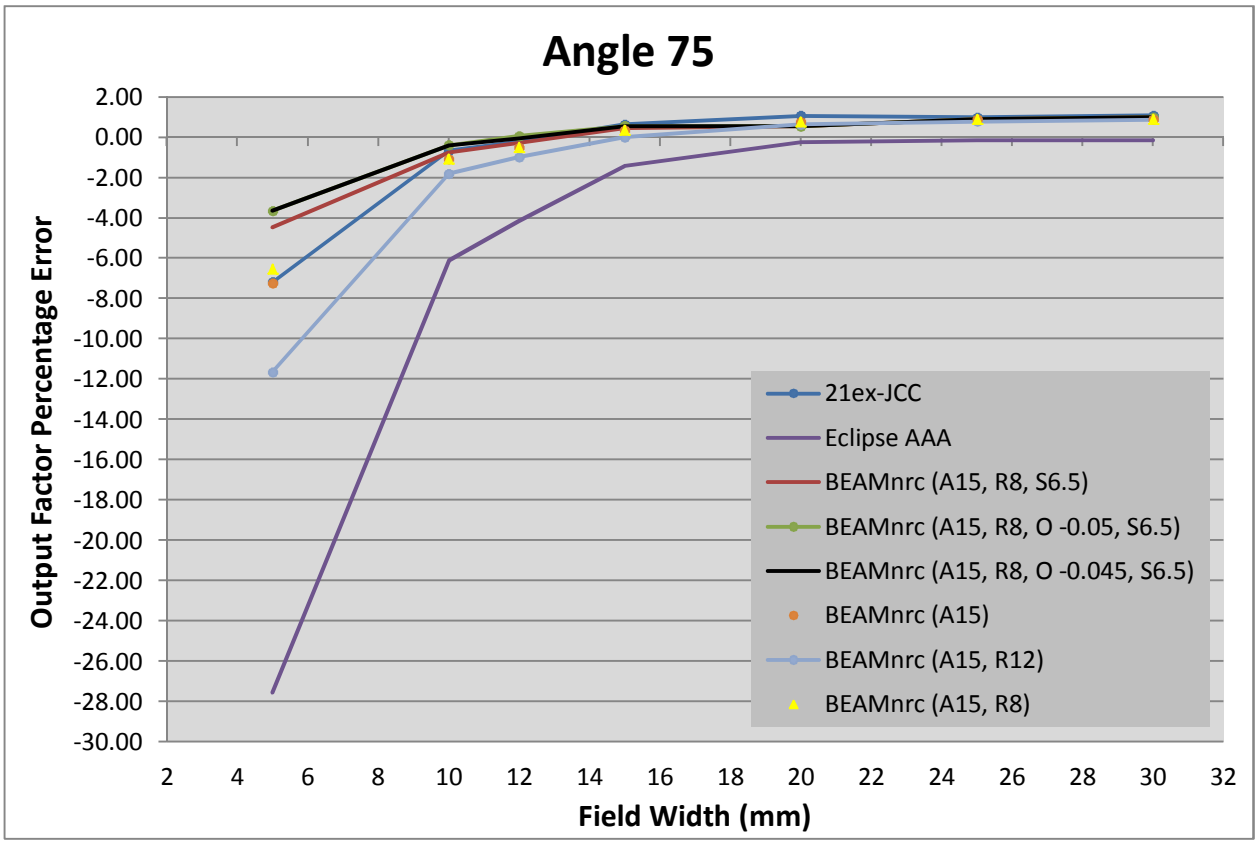
Angle 75
Output Factor Percentage Error
2.00
0.00
-2.00
-4.00
-6.00
-8.00
-10.00
-12.00
-14.00
-16.00
-18.00
-20.00
-22.00
-24.00
-26.00
-28.00
-30.00
2
4
6
8
10
12
14
16
18
20
22
24
26
28
30
32
Field Width (mm)
21ex-JCC
Eclipse AAA
BEAMnrc (A15, R8, S6.5)
BEAMnrc (A15, R8, O -0.05, S6.5)
BEAMnrc (A15, R8, O -0.045, S6.5)
BEAMnrc (A15)
BEAMnrc (A15, R12)
BEAMnrc (A15, R8)

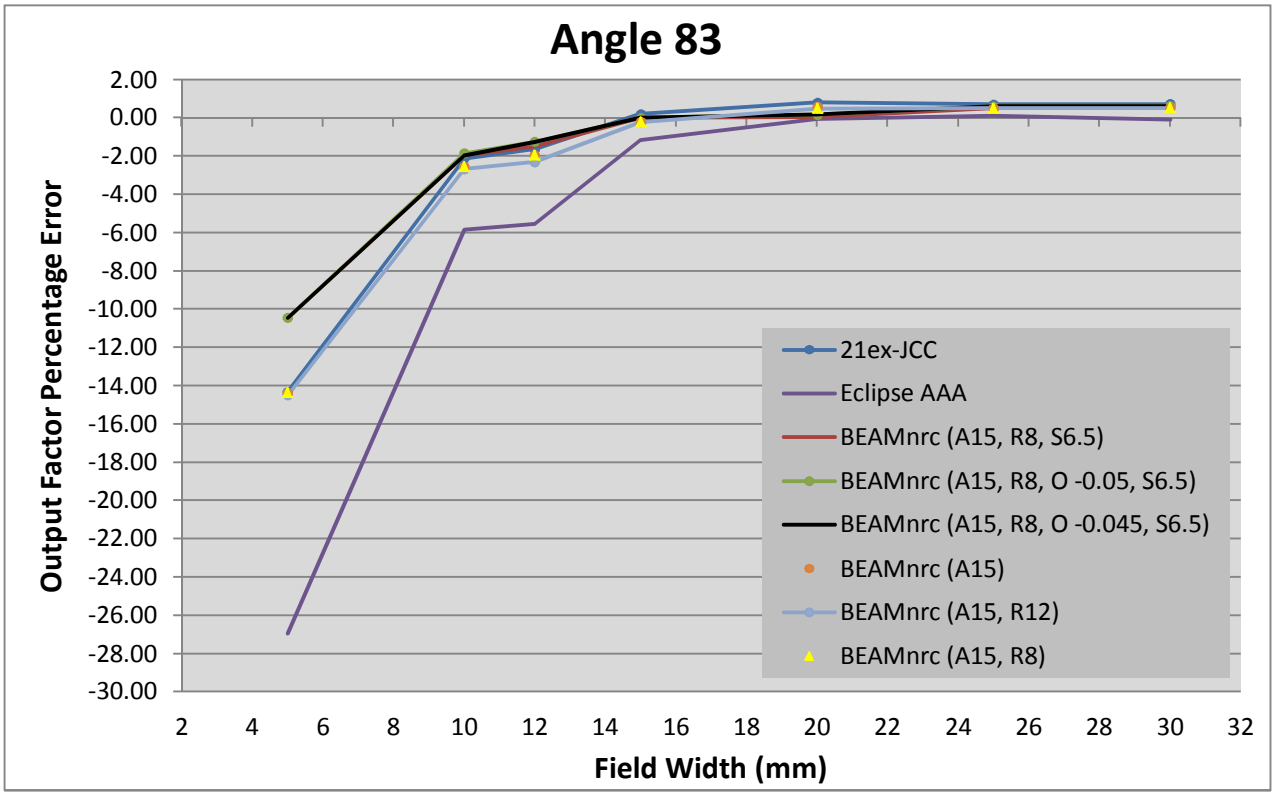

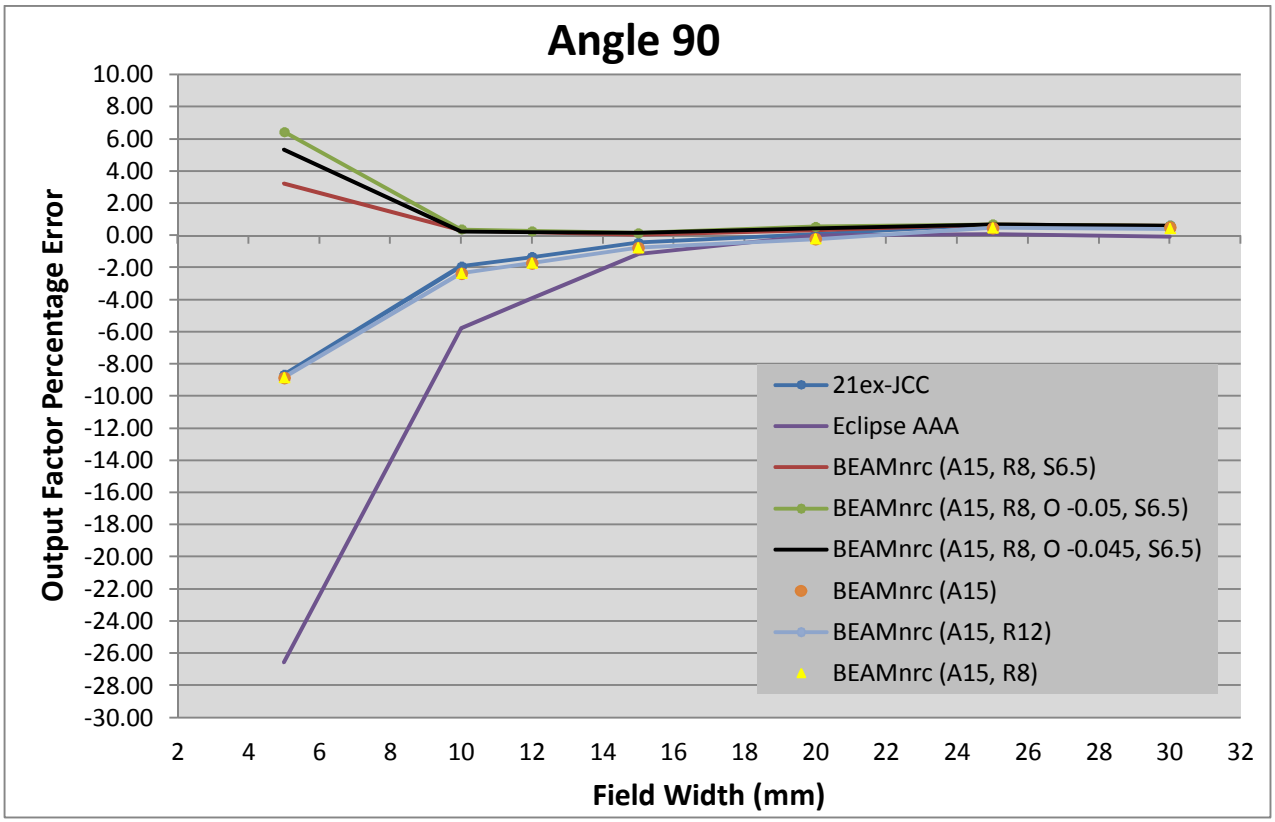

Graph 33. Percentage error calculation of output factor based on the Sun-point diode detector and different computed machines throughout a series of collimator angles. Note that field length is fixed at 15 cm and the output factors were calculated relative to 10 x 10 cm^2 open jaws field

Based on graph 33, it can be seen that BEAMnrc (A15) (orange dots) yields approximately the same results as the 21ex-JCC clinical machine (blue line) throughout the series of collimator angles, except for one particular case at width of 20 mm and collimator angled at 45º, where output factor agreement was worst. This indicates that applying a slightly softer spectrum has no effect on these long and narrow fields. The use of a 12 cm leaf tip radius of curvature along with the 15 cm water attenuated spectrum worsened the results significantly for smaller width fields for the whole set of collimator angulations (BEAMnrc (A15, R12) (grey line)). Using a nominal leaf tip radius of 8 cm which, corresponds to the MLC calibration offset table (BEAMnrc (A15, R8) (yellow triangle)) did not lead to any observed difference in comparison to the 21ex-JCC beam model for the entire series of collimator angles. Conversely, these settings have led to an observed improvement in the calculated output factor for the square MLC defined fields presented in the previous section.

Adjusting the Off-Axis Softening Factor parameter to 6.5 in correlation with 15 cm attenuated water spectrum and 8 cm nominal leaf tip radius (BEAMnrc (A15, R8, S6.5) (red line)) led to improvements in the computed output factors for fields less than 10 mm wide throughout the series of collimator angles in comparison to the 21ex-JCC clinical machine, except at zero collimator angle where it shows approximately the same results. Moreover, while the underestimation of the dose was improved, the output factor was overestimated by about 3% for a field width of 0.5 mm at 90º collimator angle in comparison with an under estimation of about -9% with the 21ex-JCC clinical machine.

Enlarging the fields slightly by subtracting a fixed value from the MLC calibration offset table significantly improved the output factor calculation for these long and narrow

fields. This is shown for the calculation using either BEAMnrc (A15, R8, O -0.05, S6.5) (green line) or BEAMnrc (A15, R8, O -0.045, S6.5) (black line) machines respectively. The first machine (green line) shows a dramatic improvement in accuracy at all filed widths and angles, except at angle 90º where the result was worsened at width of 0.5 mm. The second machine (black line) was almost identical to the first one except at zero collimator angle, where it differs significantly. Conversely, the second machine has performed much better in modulating the MLC dose profile and the equivalent square output factor from previous section. From graph 33, it can be seen that Pinnacle slightly overestimates the dose at larger widths (i.e. 30 mm). However, as the field width decreases, it starts to underestimate the dose throughout the series set of collimator angles. Conversely, Eclipse AAA consistently underestimates the dose. In addition, for field widths less than 20 mm, Eclipse dose is too low compared to Pinnacle calculations and measurements. However, at angles of 75º, 83º and 90º for a width range from 20 to 30 mm, Eclipse AAA performs much better than Pinnacle machines, while Pinnacle generally shows better results for widths less than 20 mm.

Graph 34 shows the output factor calculation relative to 10 x 10 cm^2 open field against collimator angles for various field widths. The graph includes data from the Sun-point diode measurements (green line), Pinnacle 21ex-JCC (red line), BEAMnrc (A15, R8, O -0.045, S6.5) (purple line), and Eclipse AAA (blue line) calculation. Similar to the analyses for graph 33, Eclipse calculation in general underestimated the doses, while Pinnacle performed better at field widths from 5 mm up to 20 mm. At 20 mm field width and beyond, Pinnacle overestimates the dose in general. The graph also demonstrates that, as the collimator angle changes from 0º to 90º, the measured dose

tends to falls slightly due to the effect of the scalloped edges of the MLC. This indicates that there is a dependence of output factor collimator angle.

Both Eclipse AAA and Pinnacle calculations show a similar trend. However, Pinnacle data shows large fluctuations as the collimator rotates in contrast to Eclipse AAA calculations for field widths of 25 and 30 mm, which are independent of collimator angle. The results demonstrate that Pinnacle determinations of the scattered dose were much better, especially at smaller fields compared to Eclipse AAA calculation. Discussion and explanation to this observation will carry on at chapter 4.

Graph 35 illustrates a simplified summary of the experimental data by showing the dependence of calculated percentage error for the 21ex-JCC, BEAMnrc (A15, R8, O -0.45, S6.5) and Eclipse AAA calculations relative to the diode measurements for various collimator angles and field widths. Further discussion will be presented in chapter 4.

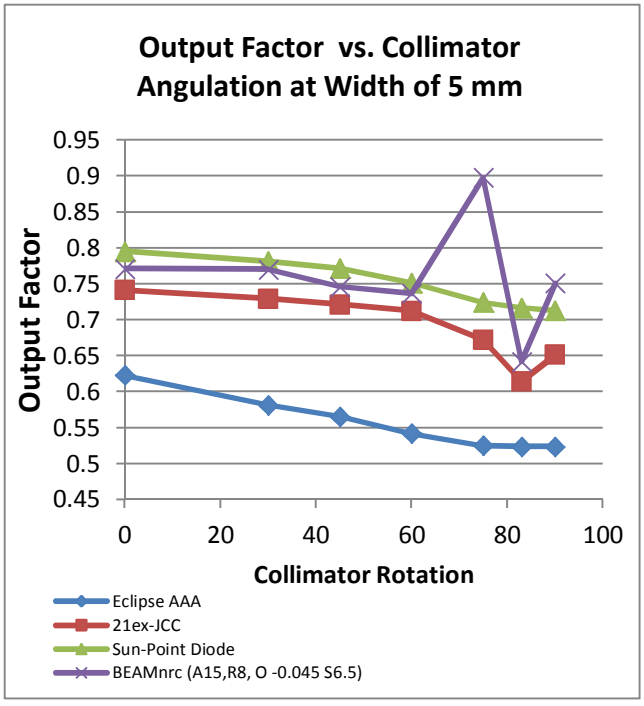

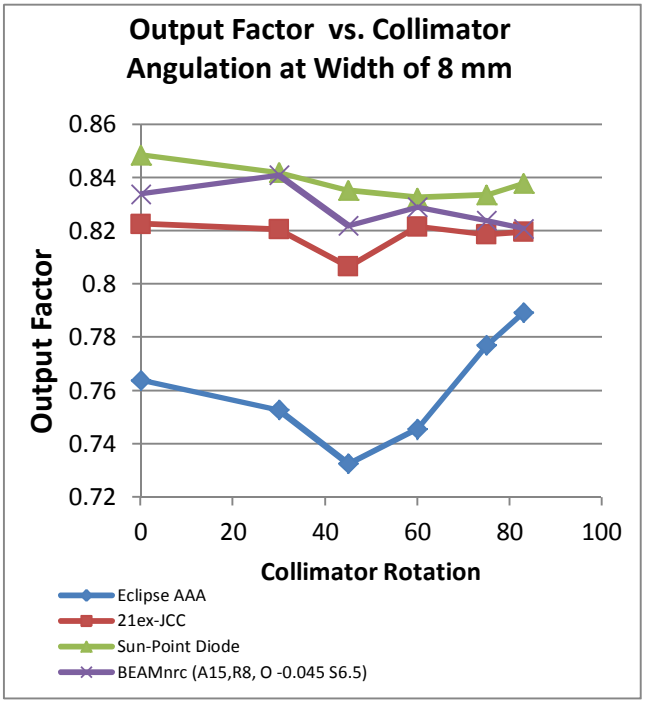

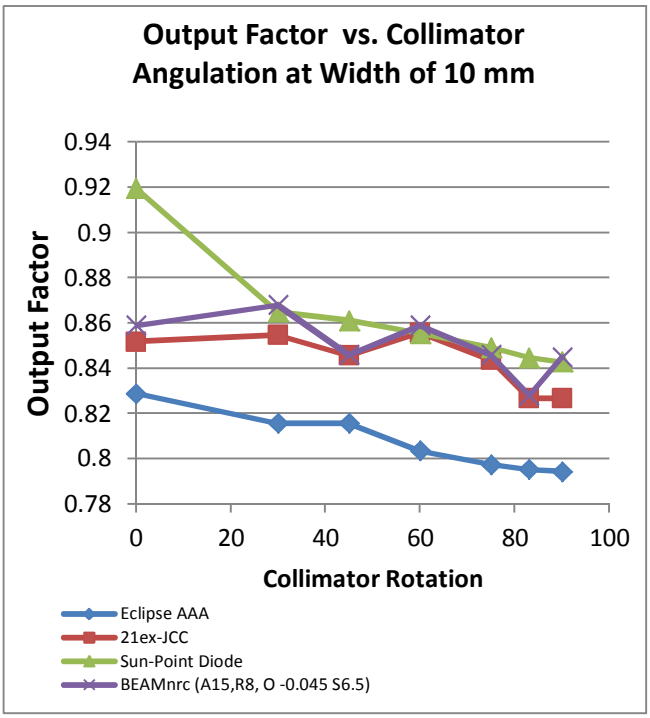
Output Factor vs. Collimator Angulation at Width of 10 mm
Output Factor
0.94
0.92
0.9
0.88
0.86
0.84
0.82
0.8
0.78
0
20
40
60
80
100
Collimator Rotation
Eclipse AAA
21ex-JCC
Sun-Point Diode
BEAMnrc (A15,R8, O -0.045 S6.5)

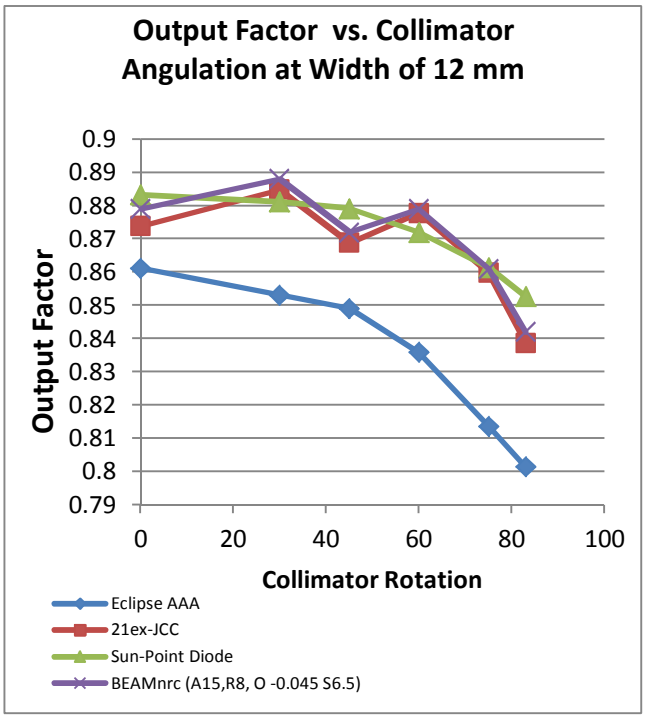
Output Factor vs. Collimator Angulation at Width of 12 mm
Output Factor
0.9
0.89
0.88
0.87
0.86
0.85
0.84
0.83
0.82
0.81
0.8
0.79
0
20
40
60
80
100
Collimator Rotation
Eclipse AAA
21ex-JCC
Sun-Point Diode
BEAMnrc (A15,R8, O -0.045 S6.5)

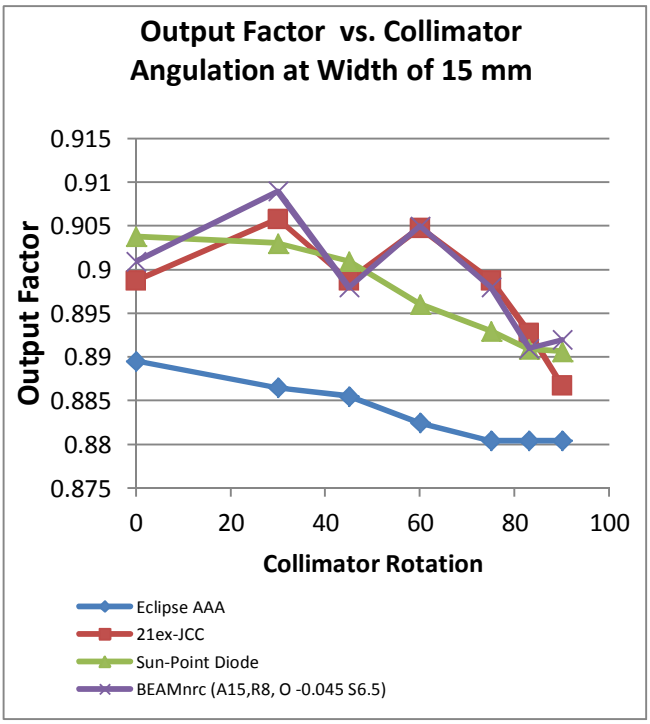
Output Factor vs. Collimator Angulation at Width of 15 mm
Output Factor
0.915
0.91
0.905
0.9
0.895
0.89
0.885
0.88
0.875
0
20
40
60
80
100
Collimator Rotation
Eclipse AAA
21ex-JCC
Sun-Point Diode
BEAMnrc (A15,R8, O -0.045 S6.5)

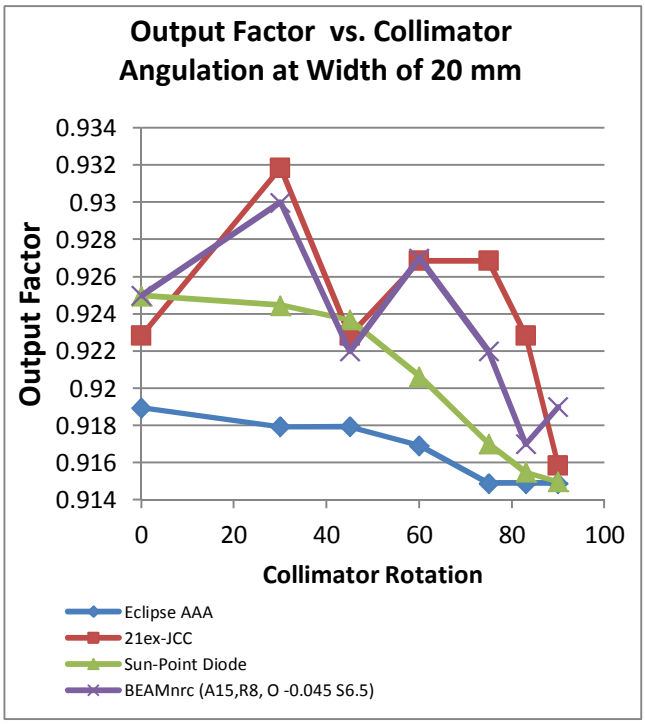
Output Factor vs. Collimator Angulation at Width of 20 mm
Output Factor
0.934
0.932
0.93
0.928
0.926
0.924
0.922
0.92
0.918
0.916
0.914
0
20
40
60
80
100
Collimator Rotation
Eclipse AAA
21ex-JCC
Sun-Point Diode
BEAMnrc (A15,R8, O -0.045 S6.5)

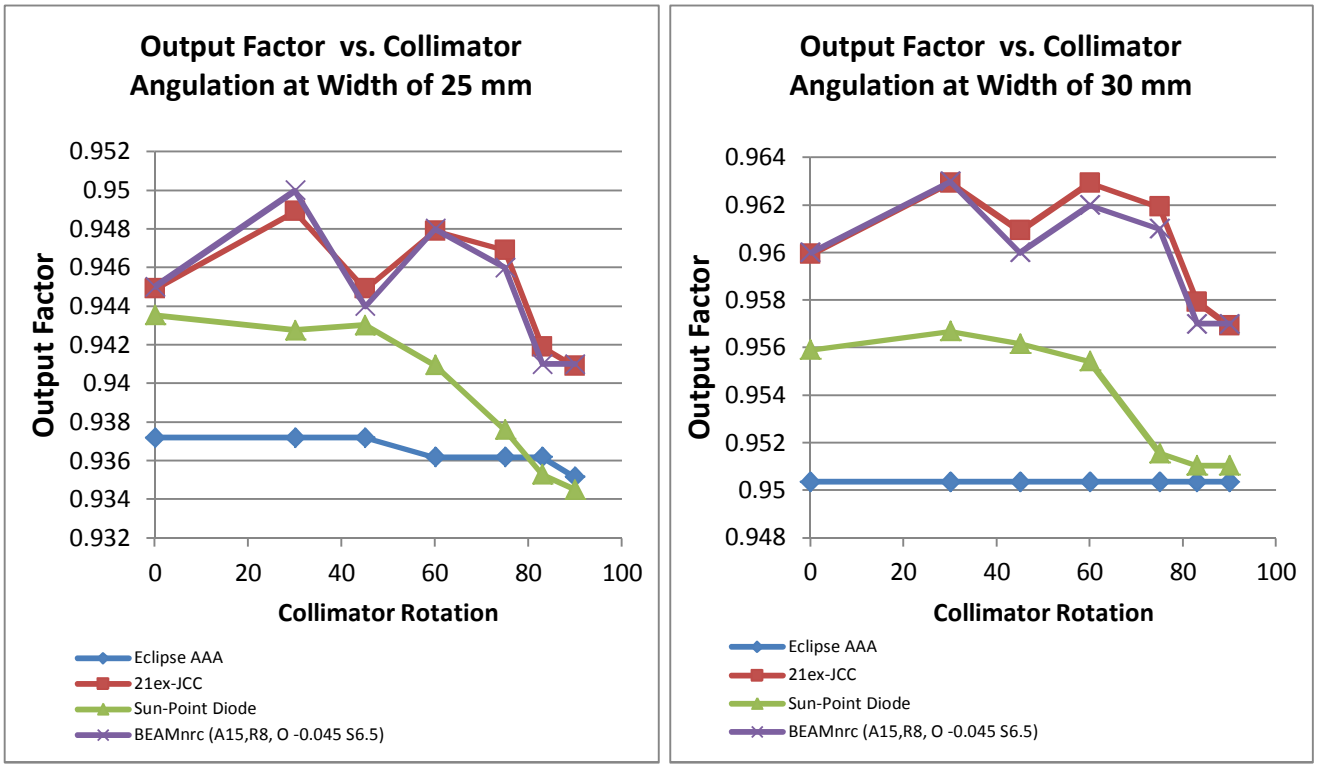

Graph 34. Output factor against collimator angle rotation for series of field widths. The green line represents the Sun-point diode measurements, while the blue line represents Eclipse AAA calculations, the red and purple line represents calculations of Pinnacle 21ex-JCC and BEAMnrc (A15, R8, O -0.045, S6.5) models. Note that fields length are fixed at 15 cm and the output factors were calculated relative to 10 x 10 cm^2 open jaws field

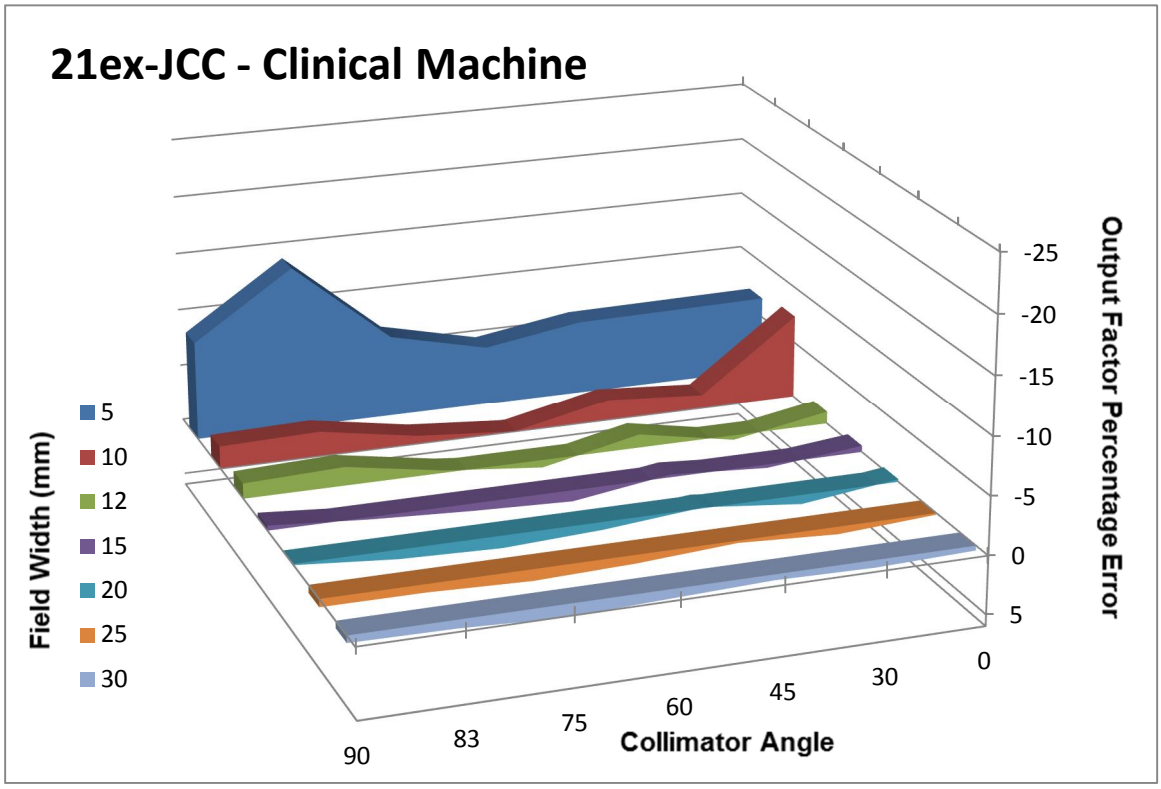
21ex-JCC - Clinical Machine
Field Width (mm)
5
10
12
15
20
25
30
90
83
75
60
45
30
0
Collimator Angle
-25
-20
-15
-10
-5
0
5
Output Factor Percentage Error

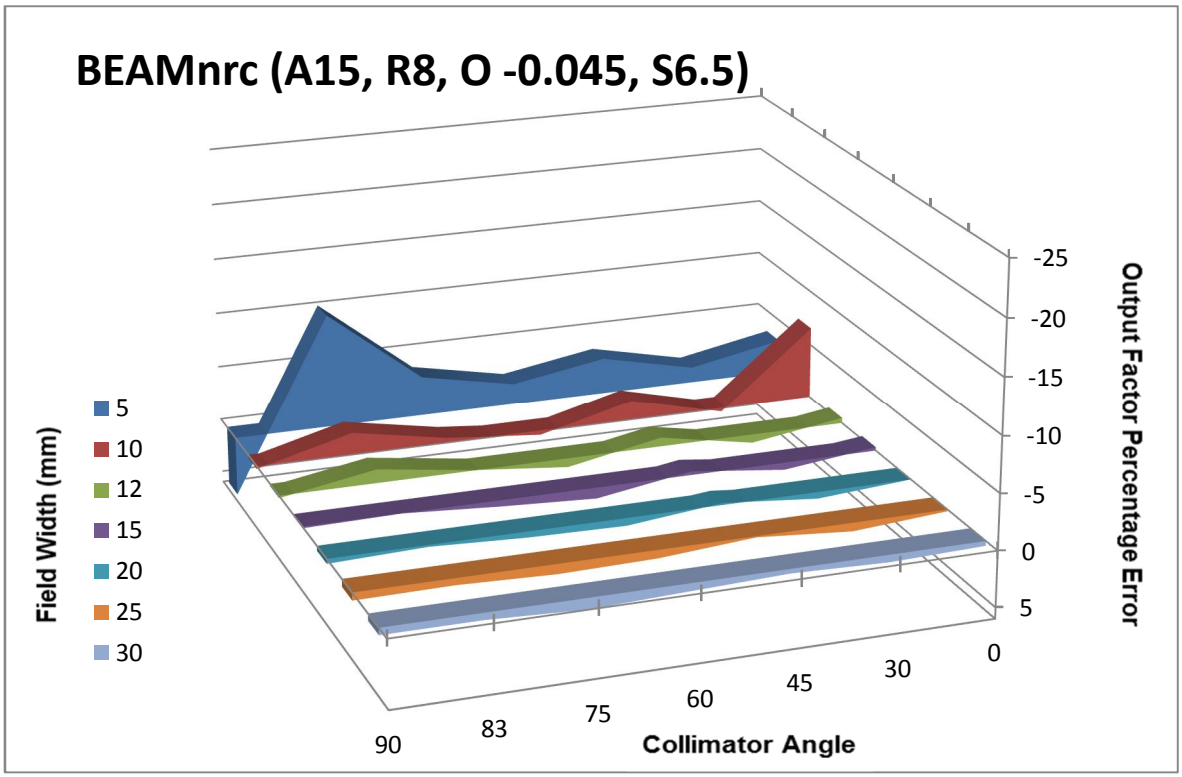
BEAMnrc (A15, R8, O -0.045, S6.5)
Field Width (mm)
5
10
12
15
20
25
30
90
83
75
60
45
30
0
Collimator Angle
-25
-20
-15
-10
-5
0
5
Output Factor Percentage Error

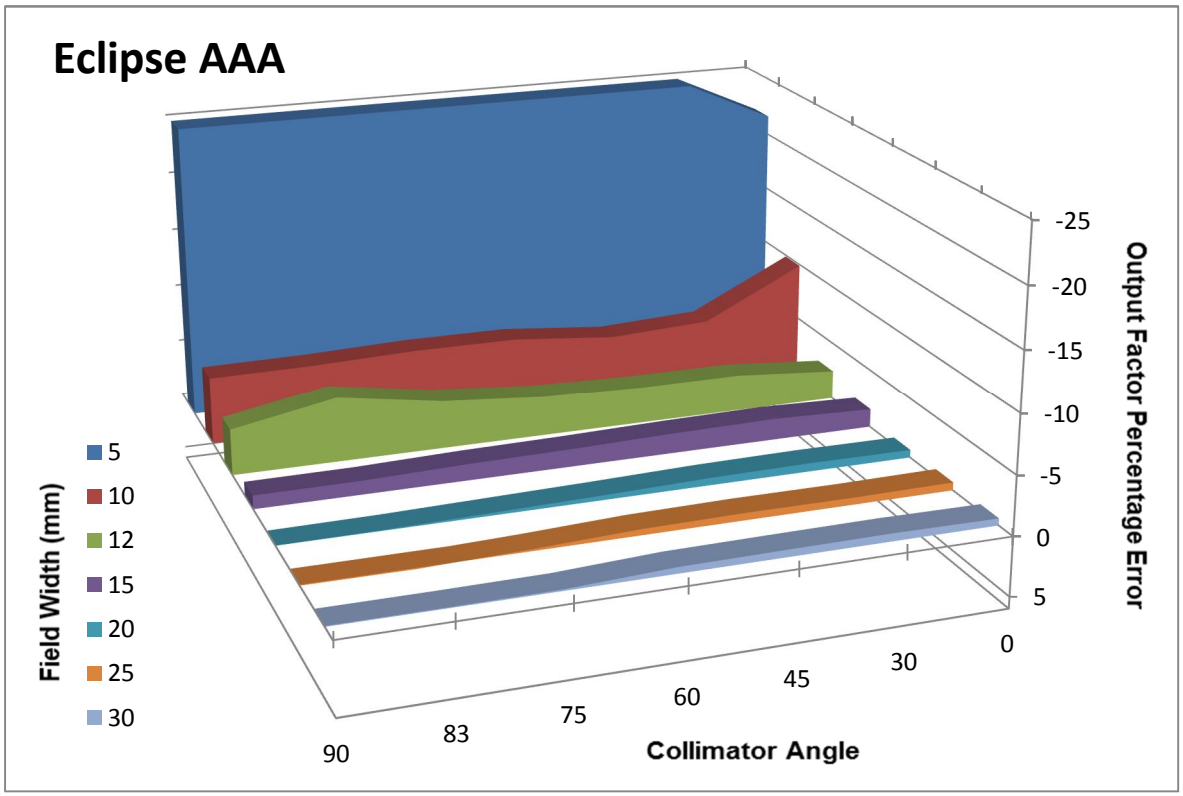

Graph 35. Demonstrate of percentage error calculation of output factor based on Sun-point diode measurements illustrating the dependence on both collimator angles and field widths for the 21ex-JCC, BEAMnrc (A15, R8, O -0.45, S6.5) and Eclipse AAA calculations respectively. Note that field length is fixed at 15 cm and the output factors were calculated relative to 10 x 10 cm^2 open jaws field

CHAPTER 4: DISCUSSION AND CONCLUSION

4.1 - Discussion:

4.1.1 - Photon Energy Spectrum:

In clinical radiotherapy, computation of absorbed dose distribution convolution methods have become more reliable due to its simplicity and accuracy (Papanikolaou *et al*, 1993)[17]. The convolution algorithm implemented in the Pinnacle planning system is based upon the work of Mackie (1985, 1988, 1990) and Papanikolaou (1993) (Pinnacle[3] Physics Reference Guide)[6]. The essential components of a convolution model are arrays tracing TERMA, representing the energy imparted throughout the medium by the primary photons, and the EDK (energy deposition kernel), representing the deposition of energy about each primary interaction site (refer to chapter 1 for more details). The use of convolution to calculate the dose distributions in a homogeneous medium could be either by the **components** method or by the **single polyenergetic convolution** method.

In the components method implementation, spectral information of the polyenergetic photon beam is determined as a fluence-weighted sum of appropriate monoenergetic dose distributions that are calculated separately (Papanikolaou *et al*, 1993)[17]. These monoenergetic kernels are correctly weighted for the spectrum that exists at the depth of the primary interaction (PW Hoban, 1995)[41]. The model requires a separate convolution for each spectral bin components. Therefore, it can handle spectral hardening effect correctly (Papanikolaou *et al*, 1993)[17]. This calculation approach is inefficient and time consuming in terms of CPU power.

An alternative quicker approach is the use of a single polyenergetic convolution model, where the spectral information of the beam is used to calculate a number of weighted mean quantities that are involved in the convolution. Papanikolaou *et al*, 1993[17] reported the following final equation for calculation of dose from polyenergetic beam using single polyenergetic convolution:

$$D(r, MV) = \int \frac{\bar{\mu}}{\rho}(r', MV)\, \bar{h}\nu(r', MV)\, \bar{F}(r', MV)\, \phi_0(MV) \times \left(\frac{|r_0|}{|r|}\right)^2 \bar{A}(r', r - r', MV) d^3r' \quad (5)$$

Where $\phi_0(MV)$ represents the total incident fluence from the polyenergetic beam (defined at the phantom surface for the work reported by Papanikolaou *et al*, 1993[17]). The quantities $\bar{\mu}/\rho$ (average mass attenuation coefficient), $\bar{h}\nu$(average energy), and $\bar{F}$ (average attenuation in the phantom) are determined based on the incident photon fluence at a specific depth. Therefore, TERMA at a point as a function of depth is calculated.

The average polyenergetic kernel is uniquely defined from the spectrum of the beam using a set of monoenergetic kernels that can be weighted as a TERMA-weighted spectrum-averaged kernel $\bar{A}(r', r - r', MV)$. This kernel contains all the dosimetry information regarding the primary electron transport and scattered photons dose. This mean polyenergetic kernel is based on the incident fluence at a certain depth, which is determined from the spectral components of the beam (defined at the phantom surface based on Papanikolaou *et al*, 1993[17]) and would be applied throughout the phantom.

The inverse square correction $(|r_0|/|r|)^2$ is performed at the dose deposition site in order to correct for the kernel tilting effect with beam divergence (Papanikolaou *et al*, 1993)[17].

However, it has to be noticed that this mean polyenergetic kernel is computed using kernel weights of monoenergetic components that were generated using a particular spectrum at a specific depth. Therefore, as the depth increases, beam hardening become more pronounced due to the preferential removal of low-energy photons with increasing depth, resulting in a greater fraction of higher-energy photons. In this situation, a polyenergetic kernel generated from a photon energy spectrum corresponding to a certain depth compute dose per fluence correctly for that depth only (Papanikolaou *et al*, 1993)[17].

For the dose calculation to be accurate at every depth, beam hardening must be accounted for in the TERMA calculation and in the use of the EDKs. TERMA has the greatest effect on the shape of the depth dose curve. Yet, hardening is easily accounted in TERMA calculation if linear attenuation coefficients corresponded to each energy components of a known incident spectrum are used (PW Hoban *et al*, 1994)[13]. However, it is not simple to account for the hardening effects in the generation of the kernels. The monoenergetic kernel weights need to be attenuated at every depth in order to find a corresponding mean polyenergetic kernel that matches for that depth before performing the convolution process. However, this approach is impractical due to the inefficient CPU time, which would results in a loss of speed advantage over the components method. Instead, Papanikolaou *et al*, 1993[(17)] introduced a correction factor to handle the hardening effect. This factor is energy and depth dependent and was obtained by a

simple linear fit to the ratio of the depth dose curves from the components and the single polyenergetic convolution methods. A kernel hardening correction factor CF(MV,d) was obtained based on this linear relationship with depth. The single polyenergetic convolution calculation would approximate the dose distribution, which can be multiplied by the corresponding correction factor to yield the real dose. Based on preliminary results, this correction was found to be independent of field size and SSD, which makes it a practical way to account for kernel spatial variance (Papanikolaou *et al*, 1993)[17]. However, field size dependence may have been noticed if smaller fields had been investigated due to the dominance of the primary dose components, since only 10 x 10 and 20 x 20 cm^2 fields were compared by Papanikolaou *et al*, 1993[(17)] (PW Hoban, 1995)[41]. More details will be discussed in section 4.2.

The Pinnacle planning system has adopted this single polyenergetic convolution approach. The photon spectrum is represented by a set of relative photon fluence that values at 15 discrete energies, which already has available corresponding monoenergetic dose-spread kernels within the software. As discussed in section 2.1.1, these relative spectral weights are variable and can be modified to fit calculated to measured dose distributions. The Monte Carlo BEAMnrc spectrum was normalized first to the relative photon fluence spectrum that is implemented in the clinical machine. The new machine model retained the same modeling parameters as the clinical machine, except for the fluence spectrum. This spectrum resulted in an underestimation of the PDD curve. In section 2.3.2, BEAMnrc spectrum was attenuated by various depths of water as shown in graph 9. Accordingly, as found in section 3.2, the depth of 15 cm of water gives the closest agreement between the computed and measured depth doses

similar to the clinical machine spectrum, which was determined by conventional means. The hardened spectrum (BEAMnrc (A15)) is expected to match the depth dose at 15 cm. According to Pinnacle physics notes, an energy and depth dependent correction factor is applied so that the depth dose matches at all depths. It appears that this correction factor is unity at a depth of 15 cm, since attenuating the BEAMnrc spectrum to this depth gives the best results at all depths. This implies that the correction factor is derived from the ratio of the components method to the polyenergetic kernel method of convolution where the polyenergetic kernel corresponds to the spectrum at 15 cm depth.

The BEAMnrc (A15) spectrum shape behaved differently from the 21ex-JCC spectrum as shown in graph 13. However, the Pinnacle calculation of the mean energy at the central axis shows a 2.105 MeV for the BEAMnrc (A15) in comparison to 2.115 MeV for the 21ex-JCC spectrum. This indicates that BEAMnrc (A15) spectrum is slightly softer than the 21ex-JCC spectrum. Yet, both spectra resulted in very similar PDD curves as shown in graph 14.

On the other hand, the mean energy as a function of distance from the central axis falls more quickly with off-axis distance in the case of the BEAMnrc (A15) spectrum (graph 16). This causes a degree of discrepancy in dose profile computation against measurements for fields larger than 10 x 10 cm^2 at shallow depths. The reduction in the mean energy causes the horns to become more pronounced for wider fields at the shoulder of the dose profile (graph 17), while it has no effect for fields smaller than 10 x 10 cm^2. This might be due to the increase in mean energy difference between the BEAMnrc (A15) and the 21ex-JCC as we go far from the central axis (graph16). Nevertheless, these differences in mean energy were found to have no effect on the

dose profiles of larger fields at deeper depths (graph 18). The error in the computed dose profiles using the BEAMnrc (A15) spectrum for larger field sizes at shallow depths was accounted for by adjusting the Off-Axis Softening Factor parameter from 8.45312 to 6.5, while retaining the same radial fluence as the 21ex-JCC clinical machine (graph 18). As a result, the BEAMnrc (A15, S6.5) mean energy does not fall at the same rate as before the adjustment, remaining slightly higher than the 21ex-JCC mean energy off-axis (graph 16). Moreover, BEAMnrc (A15) spectrum yielded slightly better calculation of OFc and OFp compared to the 21ex-JCC spectrum (graph 20).

As shown in section 3.2 and 3.3, the BEAMnrc (A15, S6.5) spectrum was validated using the conventional methods of PDD curves and dose profiles agreements with measurements for fields defined by jaws only. It has to be emphasized that our new machine contains the same modeling parameters as the clinical machine model, except for the photon fluence and the Off-Axis Softening Factor parameter.

4.1.2 - MLC Leaf Tip Radius and Offset Table:

The BEAMnrc (A15) spectrum model was also validated using fields defined by MLC only. As found in section 3.5, the slightly softer spectrum of BEAMnrc (A15) models led to a little wider penumbra at low gradient regions near the tails of the dose profiles. While at high gradient regions near the shoulders, no differences have been found between the BEAMnrc (A15) and the 21ex-JCC model. However, increasing the leaf tip radius from 6.5 cm to 8 cm led to better agreement, since it has sharpened the penumbra at the tails of the dose profile (graph 21). This radius agrees with the Varian Millennium MLC leaf tip radius of curvature, while corresponds to the Varian MLC

calibration offset table. The 21ex-JCC and BEAMnrc (A15, R8) models were found to be underestimating the penumbra and the shoulders of the dose profile in the X and Y axis for the fields defined by MLC. However, the x-axis disagreements were much more apparent than the Y-axis. The Y-axis field size is determined by the geometrical thickness of the leaf. This defect is a function of the tongue-and-groove effect. It might be accounted for by adjusting either the width of the tongue-and-groove or the amount of the additional interleaf leakage transmission or both. This was not addressed in our investigation.

The x-axis field size is determined as a function of Pinnacle leaf position (leaf tip projection to the isocenter) plus the position-dependent leaf offset (refer to section 2.1.2). Adjustments to the MLC offset table can be made to account for this effect. As described in section 3.5, subtracting a fixed value of 0.045 cm from the whole leaf tip calibration offset table led to the best agreement with the measured dose profiles. An example can be seen in graph 22 for the BEAMnrc (A15, R8, O -0.045) model. Moreover, this correction was found to have a smaller effect as the field size increased.

4.1.3 - Overview Discussion:

Rather than relying only on conventional methods to validate the new model, which includes the photon energy spectrum, Off-Axis Softening Factor, MLC rounded leaf tip radius and MLC calibration offsets. Setups have been proposed to assess the effect of these parameters on MLC abutment leakage and output factors calculated for long and narrow MLC defined fields and square MLC and jaws defined fields.

Section 3.6 shows the MLC abutment leakage calculation. The use of a softer spectrum resulted in a slightly higher leakage as shown in graph 23 when same transmission parameters were used. This is expected since the MLC model would use the user specified leaf thickness and the MLC transmission to calculate an effective attenuation coefficient for the MLC leaf material. This would be then applied to each path length in order to determine an MLC transmission array. The final effective MLC transmission arrays are multiplied by the incident energy fluence arrays to incorporate the presence of the MLC leaf, the rounded leaf ends and the tongue-and-groove effects. In regions below the leaf tip, the rounded leaf tip radius and the leaf position offset are used to generate the increase in leaf tip transmission in transition from the full thickness of the MLC leaf (Cadman *et al*, 2005)[42].

The use of 6.5 cm leaf tip radius for either the 21ex-JCC or any of the BEAMnrc spectrum led to an unrealistic gradual increase in abutment profile as the distance increases from the central axis. However, using the 8 cm leaf tip radius value that corresponds to the Varian Millennium MLC in addition to the Varian MLC offset table led to results that are more realistic. No differences in abutment leakage were found when the Off-Axis Softening parameter for BEAMnrc (A15, R8, S6.5) was adjusted. Moreover, the 12 cm leaf tip radius suggested by Williams and Metcalfe, 2005[(34)] to improve dosimetric accuracy was found to worsen the result of the abutment leakage by introducing an irregular profile shape (graph 23).

The most important finding was made when these abutment plans were delivered at the machine for film measurements. The machine did not apply the MLC offset table since there were zero gaps between planned opposing leaves. Therefore, due to the

beam divergence far from central axis, a ray would pass through a greater thickness of the leaf body that would lower the transmission leakage (graph 25). Both Pinnacle and Eclipse did not show such a trend, since they both applied the MLC offset table, which opens a gap between the leaves corresponding to the offsets. As a result, the calculated abutment field profiles became widely discrepant in comparison with the measurement, especially at the field edge farthest from central axis. Moreover, it can be seen that Eclipse AAA calculations were more discrepant with measurements in comparison to Pinnacle. The measurement also shows higher peaks closer to central axis. Applying a model with a zero MLC offset table did not fully address these discrepancies (graph 25). This is because the calculated profile variations do not decrease with off axis distance in a way consistent with the measurements.

Replanning the abutment setup with 0.5 and 1 mm gap insured that the linac would apply the MLC offset table to correspond with Pinnacle calculation. The abutment field profile calculations were in better agreement with the measurements. The use of the 8 cm leaf tip radius was also a better choice for Pinnacle beam modeling, since the calculated field profile variations far from central axis were in good agreement with measurements. The profile valleys were also in good agreement, except at points far from central axis were the measured profile shows a quicker drop. However, higher profile peaks were still observed on the measurements (graph 26 - 27). This is an indication that Pinnacle beam modeling does not consider the transmission through the leaf tip properly. Calculating the gap abutment field profiles using the BEAMnrc (A15, R8, O -0.045) model that encounter a small adjustments to the leaf offset table results in

a slight increase in the opposed leaf separation, which led to better agreement at the profile peaks, while profile valleys become somewhat offset.

Moving onto output factor calculation for small square fields defined by MLC (graph 29 A-B), it was shown in section 3.7.1 based on the PSD percentage error calculation that both Pinnacle 21ex-JCC and Eclipse AAA underestimate the dose for fields smaller than 1.5 x 1.5 cm^2. However, the dose calculated using Eclipse was far lower than that calculated using Pinnacle for both center and offset abutted MLC setup. The 21ex-JCC and Eclipse AAA calculations of 0.5 x 0.5 cm^2 field were found to be low by -3.44% and -26.85% respectively for the center abutted setup, while they were both low by -10.19% and -23.78% respectively for the 4 cm offset abutted setup. Furthermore, we found that for center and offset abutted MLC setup fields ranging from 2 x 2 up to 8 x 8 cm^2, the 21ex-JCC calculation on average overestimates the dose by 0.63% and 0.43% respectively, while Eclipse AAA on average underestimates the dose by -0.30% and -0.53% respectively (table 4 and 5). Moving into the long and narrow setups (section 3.7.2), the fields length were fixed at 15 cm, while field width was changed from 5 up to 30 mm. Compared to Sun-point diode measurements, the error of Pinnacle 21ex-JCC calculation shows an average overestimation of 0.68% throughout the series of collimator angles at a width of 30 mm, while Eclipse AAA shows an average underestimation of -0.38% (graphs 33). As the field width decreases, both the Pinnacle 21ex-JCC and Eclipse AAA calculations gradually underestimated the doses. However, Eclipse becomes far more discrepant compared with Pinnacle calculation. For instance, at a field width of 5 mm, Pinnacle 21ex-JCC calculates a dose that is on

average low by -7.88%, while Eclipse AAA calculates a dose that is on average low by -26.11% throughout the series of collimator angles.

Based on PSD data percentage error calculation, it has been shown that a slightly softer spectrum based on 15 cm of BEAMnrc water attenuation led to a slightly better estimation of the dose in both center and offset abutted MLC square field setups (graph 31 A and B). In contrast, for the long and narrow MLC setup, this spectrum led to no obvious changes in comparison to the 21ex-JCC percentage error calculation based on Sun-point diode output factor measurements (graphs 33). This observation was consistent for the series of collimator angles plotted against slit width. Using an 8 cm leaf tip radius has improved the calculation accuracy for square fields smaller than 6 x 6 cm^2 in both center and offset abutted MLC setups. The model was further improved by adjusting the off-axis softening factor to 6.5 most effectively at 0.5 x 0.5 cm^2. However, the 8 cm leaf tip did not lead to any noticeable differences when calculating long and narrow fields throughout the series of examined collimator angles in comparison to the 21ex-JCC calculation. The calculation was improved when 6.5 off-axes softening was used. Furthermore, the use of a 12 cm leaf tip radius improved the accuracy for both center and offset abutted MLC square fields, except at field sizes less than 1 x 1 cm^2. Similar trends have been shown for the long and narrow setup where the results worsened significantly for smaller width fields. It can be concluded that this setting might improve accuracy for larger fields, while corrupting the accuracy for very small fields.

The most effective modification that was made was based on adjusting the Varian MLC calibration offset table. Among the various models examined, subtracting a fixed

value of 0.045 cm would enlarge the separation between opposing leaves by 0.9 mm in the x-axis direction, while the separation in the y-axis direction remains the same, since the field size is determined by the geometrical thickness of the leaves. This adjustment works well for smaller fields defined by MLC without losing accuracy for larger field. The BEAMnrc (A15, R8, O -0.045, S6.5) model incorporated all the discussed beneficial adjustments. The output factor percentage error calculation based on PSD showed significant improvements for the center and offset abutted MLC setups, particularly for smaller fields. For instance at 0.5 x 0.5 cm^2 field center abutted MLC setup, the dose was overestimated by 1.17% in comparison to an underestimation of -3.44% for the 21ex-JCC calculation (graph 32A); while for the offset abutted setup, the model underestimated the dose by -5.25% in comparison to -10.19% for the 21ex-JCC calculation (graph 32B). For more details, refer to table 4 and 5. The output factor percentage error calculation based on Sun-point diode measurements for long and narrow MLC defined fields computed using the new model shows a similar trend as the square MLC defined fields. The BEAMnrc (A15, R8, O -0.045, S6.5) model at a field width of 5 mm calculates a dose that is, on average, low by -2.63% throughout the series of examined collimator angles in comparison to -7.88% for the 21ex-JCC calculation; while at width of a 30 mm, they are both high by an average of 0.63% and 0.68% respectively throughout the series of examined collimator angles. It can be seen that this new gain in accuracy did not corrupt the calculation at larger widths where slight improvements can also be seen (graph 35).

As shown and discussed, the adjustment that was made to the MLC calibration offset table led to significant improvement in computation of the dose profiles and the

output factors for geometries defined by the MLC. However, a tradeoff has been observed between the dose profiles and the output factors computation when improvements were made using the modified offset table. The modified offset table was made to give the best compromise for our new model.

In general, it was observed that Pinnacle performs better at smaller field geometries in comparison with the Eclipse AAA calculation. Two reasons could explain this observation. First, Pinnacle uses the collapsed cone convolution algorithm to determine the scatter distribution around the primary site of photon interaction. The dose kernels are discretized along a set of collapsed cone axis where all the released energy would b rectilinearly transported, attenuated and deposited on the cone axis of equal solid angle (Ahnesjo, 1989)[16], (e.g. OMP uses 106 collapsed-cone axis for representation of energy transport). On the other hand, Eclipse AAA uses a pencil beam superposition algorithm where pencil beam monoenergetic kernels are pre-computed for narrow beams and the clinical beam are divided into small beamlets. The AAA model calculation separates the energy deposition into depth dependent directed component calculated along the central fanline and lateral component perpendicular to the fanline. However, the lateral energy transport is modeled by photon and electron scatter kernels discretized in 16 lateral directions (Van Esch *et al*, 2006)[20] (refer to section 1.4 for more details). As a result, Eclipse AAA might determine the lateral scattered doses with lower resolution in comparison to Pinnacle CC calculation. This might affect the prediction of dose in the situation of electronic disequilibrium, especially at small and narrow fields were electronic equilibrium is unlikely to occur as fields become less and less.

The second possible reason is the different implementation approach in the modeling of the MLC between the two treatment planning systems. As explained before, Pinnacle allows for the modeling of the rounded MLC leaf tip and the tongue and groove effect, while giving separate parameters for the inter-leaf and intra-leaf transmission. The system uses the MLC calibration offset table in order for the projected light field to agree with the nominal programmed leaf position (refer to section 2.1.2 for more details). On the other hand, Eclipse only uses a single averaged transmission factor to account for the MLC inter-leaf and intra-leaf transmission. While the rounded leaf tip is not modeled explicitly, its effect is approximated using an offset value that is introduced to the leaf position, which is controlled by the Dosimetric Leaf Separation (DLS). These parameters are depth and field size dependent. Accordingly, the MLC transmission and DLS are optimized to best-fit calculation to measurement. As a result, the use of a model that explicitly accounts for the effect of the MLC on small fields where electronic equilibrium does not exist would be more efficient. This is important not only to the calculation of the dose, but also to the determination of the leakage dose when MLC are abutted and to the transmission of the dose throughout the leaf. Pinnacle has shown better results than Eclipse AAA for the abutment setup, and the output factor calculation for the small square fields and the long and narrow field setups examined in our investigation.

4.2 - Overview of Pinnacle CC Convolution Algorithm Limitation:

The Pinnacle treatment planning system is based on the collapsed cone convolution that was developed by Madison group in Wisconsin. Therefore, many similarities exist with other CC algorithms that include the use of point dose kernels.

However, different implementation approaches to the solution have been used where the kernel does not separate into primary and scattered parts during the convolution (Knöös et al, 2006)[21]. Instead, all the photon scatter and electron transport dosimetry information are represented with one kernel. The hardening effect was accounted for by using a simple linear fit to the ratio of depth dose curve from the components and the single polyenergetic convolution methods, which was found to be linear with depth. This correction was found to be independent of field size and SSD as discussed in section 4.1.1. However, PW Hoban, 1995[41], stated that a field size dependence correction factor may have been noticed if smaller fields had been investigated, since Papanikolaou *et al*, 1993[17] only compared the correction factor at 10 x 10 and 20 x 20 cm^2 field. He has indicated that without the hardening correction factor, the primary dose is underestimated and the scatter dose is overestimated. However, as the field size becomes larger, the errors in the two components would increasingly cancel each other reducing the differences between the single polyenergetic and the components methods. Conversely, the differences between the two calculation methods would become larger as field size decreases, which would result in less scatter dose (PW Hoban *et al*, 1994[13] and PW Hoban, 1995[41]). This might explain why both the 21ex-JCC and BEAMnrc (A15) spectrum failed to calculate the PDD curve for 1 x 1 cm^2 field (graph 15). The hardening correction factor might cause the depth dose to be overestimated for this narrow field. However, when we used a 6 cm water attenuated BEAMnrc spectrum, it corresponded better to the kernel and the depth correction factor for that geometry only.

An alternative approach has been investigated by PW Hoban, 1995[41] where the single polyenergetic convolution is performed using TERMA, which is the sum of differential TERMA at each energy component and separate primary and scattered kernels formed by a TERMA weighted sum of monoenergetic kernels for each component. However, the kernels are generated using the energy spectrum that exists at certain medium depth. Therefore, as beam hardens due to depth increase, an increasing proportion of primary photon energy imparted is given to electron resulting in an increase in collision KERMA to TERMA ratio, which is not addressed by this method. Note that the ratio of linear energy absorption coefficient to the linear attenuation coefficient, $\boldsymbol{\mu_{en}/\mu}$, increases with energy. As a result, this proportion also increases with depth. A correction factor based on collision KERMA to TERMA ratio can be applied as following:

$$Primary\ kernel\ correction\ (z) = \frac{K_c(z)/\,T(z)}{K_c(z_0)/\,T(z_0)} \qquad (6)$$

$$Scatter\ kernel\ correction\ (z) = \frac{1 - K_c(z)/\,T(z)}{1 - K_c(z_0)/\,T(z_0)} \qquad (7)$$

Where K_c represents the collision KERMA, T represents TERMA, Z represents the depth and Z_0 represent the depth of the incident energy fluence.

These correction factors adjust the primary and scatter kernels by making them approximate the kernels that would exist at each primary interaction depth. Applying equation 6 and 7 to the single polyenergetic convolution would ensure that the sum of values in the primary kernel to approximate the ratio of $\boldsymbol{(\mu_{en}/\mu)}$ and that for the scatter

kernel to approximate the ratio of $(1- \mu_{en}/\mu)$. However, equation 7 might not be expected to give the true sum due to the long range of scattered photons. The scatter kernel should be extended large enough to account for all scattered photon absorbed energy. If that is true, then the total combined fractional energy in both kernels would be equal to unity (PW Hoban, 1995)[42]. However, the fractional energy contained in the scatter kernel is much less than that in the primary kernel. Thus, this would not contribute to a large error. Therefore, in a situation where the doses due to secondary electrons that originate from primary photon interactions becomes much larger than the dose due to scattered photons as in narrow beams, it is important to calculate the separate primary and scattered convolution doses accurately using the appropriate correction factor. Separating the kernel into primary and scatter parts is also important in situations of inhomogeneity correction, since both kernels are scaled separately to account for density variation (PW Hoban *et al*, 1994)[13].

Without the correction factor in the previous calculation methods, the proportion of energy due to primary or scatter kernels is not known at any depth other than the depth where the kernels are normalized, since both kernels are convolved with TERMA. Another method investigated by PW Hoban, 1995[41] is based on the use of collision KERMA convolution with primary kernel for primary dose calculation, and the use of the difference between TERMA and collision KERMA for the convolution with scatter kernel for scattered dose calculation. The polyenergetic primary kernel is formed by a collision KERMA weighted sum of monoenergetic kernels, which is normalized to the collision KERMA. Similarly, the scattered kernel is formed and normalized to $(T - K_c)$. In this case, the energy imparted to secondary electrons and retained by scattered photons,

along with the subsequent distribution of this energy using correctly normalized kernels is explicitly calculated at each depth. In other words, both primary and scattered energy imparted at the primary interaction site are conserved in terms of energy deposition. Therefore, this method avoids the use of correction factors since it is more direct. The use of this method is equivalent to the application of the correction factors (equation 6-7) to the polyenergetic TERMA convolution (PW Hoban, 1995)[41]. This method is currently implemented in the current generation of Nucletron: Oncentra MasterPlan (OMP) planning system (Knöös *et al*, 2006)[21]. It has to be noticed that in both methods, the kernel shape variation is not adjusted as the beam hardens. PW Hoban, 1995[41] stated that this is not an important factor based in their observations. This is because the ratio of collision KERMA to TERMA would vary with depth in the same manner as for the use of invariant polyenergetic kernels.

Another factor that could influence the Pinnacle calculation is the kernel-tilting effect. As discussed before, Pinnacle applies an inverse square correction to handle the kernel tilting associated with beam divergence. This approximation for kernel tilting might be the reason why the calculated off-axis dose profiles from the center at deeper depths were always in disagreement with measurements (graph 6). It also might be the reason for the variations in output factor for the long and narrow fields throughout the series of collimator angles when the calculation performed using Pinnacle over Eclipse AAA model (graph 34-35). The scalloped field edges near the dose calculation point could influence the determination of the scattered dose when MLC shielded area edge intersects with a collapsed cone axis at far points from central axis. Accordingly, part of the shielded area under the leaf would overestimate the dose, while the other part would

underestimate the dose, since the kernel does not follow the divergence of the beam. This situation may occur more frequently far from the central axis. This may possibly explain the variations that we observed in Pinnacle calculation. As the collimator rotates, the pattern of the scalloped MLC edges changes affecting the determination of the scattered contribution (graph 16). Eclipse AAA calculation shows minor changes in output factor calculation with collimator angle changes. This might be since AAA pencil beam beamlets are taking into account the beam divergence, even though the lateral scattered doses are determined with much lower resolution in comparison to the Pinnacle collapsed cones algorithm. The potential for geometric interplay between the scalloped field edges and the CC axes or non-tilted kernel directions bears further investigation.

Furthermore, a potentially stronger influence on output factor calculation may be from the extra photon fluence associated with the leaf tip radius. The proximity of the leaf tip to the measurement point and therefore the extra fluence due to the rounded leaf tip may affect the calculate dose at the central axis. Other influences may be due to the proximity of the leaf edge, which is associated with a reduced fluence due to the tongue and groove effect. Alterations of these parameters in the machine model are needed to elucidate the cause of the output factor variations further.

The rectilinear energy transport of TERMA method has been found to overestimate the dose. This is because charged particles tend to be more laterally deflected than this method can predict (Keall and Hoban, 1995)[43]. The collapsed cone convolution approximation could potentially corrupt the accuracy of the calculation, especially in lateral electronic disequilibrium conditions, when the collapsed cone

rectilinear kernel approximation method represents the dose contribution from electrons (Francescon *et al*, 2000)[44]. This might explain why Pinnacle consistently shows a slight overestimation for larger fields when calculating the square fields and the long and narrow setups. This overestimation becomes significant when the dose is calculated in low-density regions. Woo and Cunningham, 1990[45] have shown that in a region beyond a high density to low density, the rectilinear scaling would lead to an overestimation of the dose, while the dose would be underestimated in a region beyond low to high density. This is because the greatest contribution to the lateral electron spread at a plane is from scattering events furthest from the plane. This is not being accounted for by the rectilinear scaling method (PW Hoban *et al*, 1990)[46].

Keall and Hoban, 1995[43] pointed out that the primary dose due to electrons that have been set in motion at the interaction site makes up most of the total dose, especially for small fields. Therefore, any error in the primary dose determination would result in similar sized errors in the total dose. The rectilinear approximation method is valid only for the scattered dose calculation, which results from electrons set in motion by scattered photons. The main reason is because photons would travel in a straight lines from the interaction site, while the subsequently ejected electrons have much less range than the mean free path of the scattered photons. In addition, these scattered photons can produce further scattered photons, which are not being accounted for by the collapsed cone rectilinear approximation. Yet, the multiply scattered photons may contribute non-negligible dose (Keall and Hoban, 1995)[43]. Because the rectilinear scaling assumes that the energy spread to be the same between different densities, the authors have suggested a new method for calculating the primary dose component that

can account for the effects of the density distribution between the interaction and the deposition site on the kernel array. This new method shows significant improvement in the total dose calculation. However, it has increases the computation time by a factor of 3 for their examined geometry.

It can be seen why separating the total dose in a primary and a scattered components is very important, even without the use of a sophisticated scaling method for representation of the kernels energy transport. The rectilinear approximation may remain most accurate when the primary and scattered components are handled separately. Separating the kernel is important, especially when dose is dominated by primary component such as in a small field, or when primary and scattered kernels are scaled separately in accounting for density changes (PW Hoban *et al*, 1994)[13]. The use of one primary and scatter kernel for electron and photon energy transport might overestimate the range of the electrons from the primary dose component. This could be worsened in heterogeneous media, or as the fields become much smaller.

4.3 - Conclusion:

A method has been investigated whereby a realistic photon fluence spectrum is used for modeling of a clinical machine in Pinnacle. The novel spectrum is based on 15 cm depth water attenuation of the BEAMnrc spectrum. This spectrum had a slight difference in mean energy at the central axis in comparison to the 21ex-JCC spectrum model, which was obtained based on conventional methods (i.e., least squares fit to present depth dose curves for various field sizes). However, with a small adjustment to the off-axis softening factor, the new spectrum was shown to be equivalent to the

21ex-JCC spectrum using a machine that has the same modeling parameters as the clinical model in calculating the PDD curves and dose profiles defined by the jaws. For fields defined by the MLC, the use of an 8 cm leaf tip radius showed a result similar to the clinical machine. The adjustment to the MLC offset table led to a significant improvement for dose profiles defined by MLC mostly at small fields.

Rather than relying on conventional methods only for assessing the beam model, different supplementary setups have been proposed to further validate our model. Studying the impact of adjusting the photon energy spectrum, Off-Axis Softening Factor, MLC rounded leaf tip radius and MLC calibration offsets, individually on a machine, while the rest of the modeling parameters were maintained the same as those of the clinical 21ex-JCC model, determined the best model fit. Combining all adjustment in one machine, the BEAMnrc (A15, R8, O -0.045, S6.5) model surpasses the 21ex-JCC model significantly, especially for small fields, when examined using small square and long and narrow setups against the measurements. Consequently, validating a model based on agreement with PDD and dose profile curves might not necessarily lead to the best machine parameters for Pinnacle beam modeling, since some effects might not be observed easily.

4.4 - Future Work:

The use of the collapsed cone convolution implemented in Pinnacle needs to be investigated in more detail. The impact of kernels not being separated into two components (primary and scattered) should be inspected explicitly. Many researchers claims that the rectilinear approximation for energy transport and deposition leads to an

overestimation of the dose, especially in low-density regions. The impact of using one kernel must be explored alone with that approximation. The kernel tilting limitation in Pinnacle must also be examined, since applying an inverse square correction does not seem to address the problem. These limitations and their impact could be investigated explicitly using Monte Carlo simulation methods.

The modification that was made to the calibration offset table shows significant improvement in computation of dose profiles and the output factor for fields defied by MLC, especially at small geometries. It may be worthwhile to investigate a leaf position dependent adjustment when modifying the MLC offset table, while considering the best compromise between the computation of dose profile and the output factors for geometries defined by the MLC.

In addition, part of the variations observed in the output factor calculation based on the long and narrow MLC defined field setup as collimator changes is due to the inappropriate handling of the kernel tilting far from central axis. A field based on 5 cm long and 20 mm width might be centered at the central axis, while the output factor would be calculated at different collimator angles. This can be repeated at 20 cm off axis, while comparing both sets of calculations with measurements. If both centered and offset long and narrow fields shows similar trends, then kernel tilting is not the problem. If they behave differently, this might explain the tilting affect, since the offset setup would suffer from more output factor variations compared to the center fields calculated in Pinnacle. It would be also important to cover other aspects of the Pinnacle beam modeling parameters that were not investigated in the current work in order to refine the model further. This should include the influence of the extra photon fluence associated

with the leaf tip radius, since this might affect the calculated dose at small geometry. Other potential factor could be due to the reduced fluence due to the tongue and groove effect associated with the proximity of the leaf edge.

Ultimately, the optimal machine model must be validated using clinical cases of both IMRT and VMAT plans, along with QA comparisons to obtain results in real situations.

REFFRENCES:

1- Khan, Faiz M. *The physics of radiation therapy*. Vol. 3. Philadelphia: Lippincott Williams & Wilkins, 2003.

2- Karzmark, C. J., and Robert J. Morton. *A primer on theory and operation of linear accelerators in radiation therapy*. Medical Physics Publishing Corporation, 1989.

3- Karzmark, C. J. "Advances in linear accelerator design for radiotherapy."*Medical physics* 11 (1984): 105.

4- AAPM Radiation Therapy Committee. Task Group 50, and Arthur Boyer. *Basic applications of multileaf collimators*. American Association of Physicists in Medicine, 2001.

5- Boyer, Arthur L., and Shidong Li. "Geometric analysis of light-field position of a multileaf collimator with curved ends." *Medical physics* 24 (1997): 757.

6- Pinnacle^3 Physics Reference Guide, Release 8.0, Printed in the United States of America. Document number 9201-5135A-ENG A.

7- Deng, Jun, Todd Pawlicki, Yan Chen, Jinsheng Li, Steve B. Jiang, and C. M. Ma. "The MLC tongue-and-groove effect on IMRT dose distributions." *Physics in Medicine and Biology* 46, no. 4 (2001): 1039.

8- Medina, Antonio Lopez, Antonio Teijeiro, Juan Garcia, Jorge Esperon, J. Antonio Terron, Diego P. Ruiz, and Maria C. Carrion. "Characterization of electron contamination in megavoltage photon beams." *Medical physics* 32 (2005): 1281.

9- Mohan, Radhe, Chen Chui, and Leon Lidofsky. "Energy and angular distributions of photons from medical linear accelerators." *Medical physics* 12 (1985): 592.

10- Sheikh-Bagheri, Daryoush, and D. W. O. Rogers. "Monte Carlo calculation of nine megavoltage photon beam spectra using the BEAM code." *Medical physics* 29 (2002): 391.

11- Ding, George X. "Energy spectra, angular spread, fluence profiles and dose distributions of 6 and 18 MV photon beams: results of Monte Carlo simulations for a Varian 2100EX accelerator." *Physics in medicine and biology* 47, no. 7 (2002): 1025.

12- Gunilla, C., and M. D. Bentel. "Radiation therapy planning." *2da. edición, McGrawHill, USA, ISBN 0-07-005115-1* (1996).

13-Hoban, P. W., D. C. Murray, and W. H. Round. "Photon beam convolution using polyenergetic energy deposition kernels." *Physics in medicine and biology* 39, no. 4 (1994): 669.

14-Presentation made by Tom Knöös, Lund, Sweden, "Model Based Dose Calculation Algorithms for Photons in External Radiation Therapy" AAPM 2009.

15-Liu, H. Helen, T. Rock Mackie, and Edwin C. McCullough. "A dual source photon beam model used in convolution/superposition dose calculations for clinical megavoltage x-ray beams." *Medical physics* 24 (1997): 1960.

16-Ahnesjö, Anders. "Collapsed cone convolution of radiant energy for photon dose calculation in heterogeneous media." *Medical Physics* 16 (1989): 577.

17-Papanikolaou, Nikos, T. Rockwell Mackie, Carol Meger-Wells, Mark Gehring, and Paul Reckwerdt. "Investigation of the convolution method for polyenergetic spectra." *Medical physics* 20 (1993): 1327.

18-Liu, H. Helen, T. Rock Mackie, and Edwin C. McCullough. "Correcting kernel tilting and hardening in convolution/superposition dose calculations for clinical divergent and polychromatic photon beams." *Medical physics* 24 (1997): 1729.

19-Butson, Martin J., Rebecca Elferink, Tsang Cheung, K. N. Peter, Michael Stokes, Kim You Quach, and Peter Metcalfe. "Verification of lung dose in an anthropomorphic phantom calculated by the collapsed cone convolution method." *Physics in medicine and biology* 45, no. 11 (2000): N143.

20-Van Esch, Ann, Laura Tillikainen, Jukka Pyykkonen, Mikko Tenhunen, Hannu Helminen, Sami Siljamäki, Jyrki Alakuijala, Marta Paiusco, Mauro Iori, and Dominique P. Huyskens. "Testing of the analytical anisotropic algorithm for photon dose calculation." *Medical physics* 33 (2006): 4130.

21-Knöös, Tommy, Elinore Wieslander, Luca Cozzi, Carsten Brink, Antonella Fogliata, Dirk Albers, Håkan Nyström, and Søren Lassen. "Comparison of dose calculation algorithms for treatment planning in external photon beam therapy for clinical situations." *Physics in medicine and biology* 51, no. 22 (2006): 5785.

22-Jin, Hosang, Jatinder Palta, Tae-Suk Suh, and Siyong Kim. "A generalized a priori dose uncertainty model of IMRT delivery." *Medical physics* 35 (2008): 982.

23-McNiven, Andrea L., Michael B. Sharpe, and Thomas G. Purdie. "A new metric for assessing IMRT modulation complexity and plan deliverability." *Medical physics* 37 (2010): 505.

24-Craft, David, Philipp Süss, and Thomas Bortfeld. "The tradeoff between treatment plan quality and required number of monitor units in intensity-modulated radiotherapy." *International Journal of Radiation Oncology* Biology* Physics* 67, no. 5 (2007): 1596-1605.

25-Boyer, Arthur L., and Timothy Schultheiss. "Effects of dosimetric and clinical uncertainty on complication-free local tumor control." *Radiotherapy and Oncology* 11, no. 1 (1988): 65-71.

26-LoSasso, Thomas, Chen-Shou Chui, and C. Clifton Ling. "Physical and dosimetric aspects of a multileaf collimation system used in the dynamic mode for implementing intensity modulated radiotherapy." *Medical physics* 25 (1998): 1919.

27-Pinnacle planning System, beam modeling configuration, JCC, Hamilton, Canada.

28-Varian Beam Configuration 8.6.17 documents. 21-ex-jcc, AAA, Unattenuated Spectrum.

29-National Institute of Standards and Technology, http://physics.nist.gov/PhysRefData/XrayMassCoef/ComTab/water.html

30-http://www.gafchromic.com

31-Klein, David M., Ramesh C. Tailor, Louis Archambault, Lilie Wang, Francois Therriault-Proulx, and A. Sam Beddar. "Measuring output factors of small fields formed by collimator jaws and multileaf collimator using plastic scintillation detectors." *Medical physics* 37 (2010): 5541.

32-Sun-Point Diode detector Benefits Analysis, http://www.sunnuclear.com/medPhys/sunpoint/sunpoint.asp.

33-Podgorsak, Ervin B. *Radiation oncology physics*. International Atomic Energy Agency, 2005.

34-Sievinen, Janne, Waldemar Ulmer, and Wolfgang Kaissl. "AAA photon dose calculation model in Eclipse." *Palo Alto (CA): Varian Medical Systems* 118 (2005).

35-Williams, M. J., and P. Metcalfe. "Verification of a rounded leaf-end MLC model used in a radiotherapy treatment planning system." *Physics in medicine and biology* 51, no. 4 (2006): N65.

36-Wasbø, E., and H. Valen. "Dosimetric discrepancies caused by differing MLC parameters for dynamic IMRT." *Physics in medicine and biology* 53, no. 2 (2008): 405.

37-Aland, T. M. L. M. L., T. Kairn, and J. Kenny. "Evaluation of a Gafchromic EBT2 film dosimetry system for radiotherapy quality assurance." *Australasian Physical & Engineering Sciences in Medicine* 34, no. 2 (2011): 251-260.

38-Scott, Alison JD, Sudhir Kumar, Alan E. Nahum, and John D. Fenwick. "Characterizing the influence of detector density on dosimeter response in non-equilibrium small photon fields." *Physics in Medicine and Biology* 57, no. 14 (2012): 4461.

39-Eklund, Karin, and Anders Ahnesjö. "Spectral perturbations from silicon diode detector encapsulation and shielding in photon fields." *Medical physics* 37 (2010): 6055.

40-Advanced Therapy Dosimeter (FLUKE 35040) specification, http://www.flukebiomedical.com/biomedical/usen/Radiation-Oncology-QA/Linear-Accelerator-QA/35040.htm?PID=54666.

41-Hoban, Peter W. "Accounting for the variation in collision kerma-to-terma ratio in polyenergetic photon beam convolution." *Medical Physics* 22 (1995): 2035.

42-Cadman, Patrick F., Todd McNutt, and Karl Bzdusek. "Validation of physics improvements for IMRT with a commercial treatment planning system." *Journal of Applied Clinical Medical Physics* 6, no. 2 (2005).

43-Keall, Paul, and Peter Hoban. "Accounting for primary electron scatter in x-ray beam convolution calculations." *Medical physics* 22 (1995): 1413.

44-Francescon, Paolo, Carlo Cavedon, Sonia Reccanello, and Stefania Cora. "Photon dose calculation of a three-dimensional treatment planning system compared to the Monte Carlo code BEAM." *Medical physics* 27 (2000): 1579.

45-Woo, M. K., and J. R. Cunningham. "The validity of the density scaling method in primary electron transport for photon and electron beams." *Medical physics*17 (1990): 187.

46-Hoban, P. W., D. C. Murray, P. E. Metcalfe, and W. H. Round. "Superposition dose calculation in lung for 10MV photons." *Australasian physical & engineering sciences in medicine/supported by the Australasian College of Physical Scientists in Medicine and the Australasian Association of Physical Sciences in Medicine* 13, no. 2 (1990): 81.

47-Krmar, M., J. Slivka, I. Bikit, M. Veskovic, Lj Conkic, M. Bistrovic, and A. Rudic. "A new method for the measurement of bremsstrahlung spectra." Physics in Medicine and Biology 38, no. 4 (1993): 533.

48-Baker, C. R., Behain Ama'ee, and Nicholas M. Spyrou. "Reconstruction of megavoltage photon spectra by attenuation analysis." Physics in medicine and biology 40, no. 4 (1995): 529.

49-Baker, Colin R., and Kyung K. Peck. "Reconstruction of 6 MV photon spectra from measured transmission including maximum energy estimation." Physics in medicine and biology 42, no. 11 (1997): 2041.

50-Nisbet, A., H. Weatherburn, J. D. Fenwick, and G. McVey. "Spectral reconstruction of clinical megavoltage photon beams and the implications of spectral determination on the dosimetry of such beams." Physics in medicine and biology 43, no. 6 (1998): 1507.

51-Nath, Ravinder, and R. J. Schulz. "Determination of high-energy x-ray spectra by photoactivation." Medical physics 3 (1976): 133.